DOI:10.18136/PE.2020.753

Novel Methods for Removing EEG Artifacts and Calculating Dynamic Brain Connectivity

A Thesis Submitted for the Degree of
Doctor of Philosophy in Computer Science

Mohamed Fawzy Ibrahim Issa

Supervisors:

Prof. Kozmann György
Dr. Juhász Zoltán

Department of Electrical Engineering and Information Systems

Doctoral School of Information Science and Technology

University of Pannonia

Veszprém, Hungary

2020

Novel Methods for Removing EEG Artifacts and Calculating Dynamic Brain Connectivity

Thesis for obtaining a PhD degree in

the Doctoral School of Information Science and Technology

of the University of Pannonia.

Written by:

Mohamed Fawzy Ibrahim Issa

Supervisors:

Prof. Kozmann György	**Dr. Juhász Zoltán**
propose acceptance (yes / no)	propose acceptance (yes / no)
.....	.....
(supervisor/s)	(supervisor/s)

The candidate has achieved **100** % in the comprehensive exam held on 31 May 2018

.....

(Head of the Doctoral School)

As reviewer, I propose acceptance of the thesis:

Name of reviewer: **Prof. Jobbágy Ákos** (yes / no)

.....

(reviewer)

As reviewer, I propose acceptance of the thesis:

Name of reviewer: **Prof. Benyó Balázs** (yes / no)

.....

(reviewer)

The PhD-candidate has achieved..... % at the public discussion,

Veszprem, Date:

.....

(Chairman of the Committee)

Th grade of the PhD diploma .....%

Veszprem, Date:

.....

(Chairman of UDHC)

Acknowledgment

First and foremost, I would like to express my thanks to ALLAH for guiding and aiding me to bring this work out to light. My deep thanks and highest gratitude go to my supervisors, Prof. Kozmann György and Dr. Juhász Zoltán for their patience, motivation, enthusiasm, and immense knowledge. I cannot possibly express anymore of my gratitude to them, not only on the guidance they gave during my study as a PhD student but valuable life experiences as well.

I would like to thank the Director of the Doctoral School Prof. Katalin Hangos for her help and support during the doctoral school report presentation. Thanks to the staff of University of Pannonia, especially Ujvári Orsolya, Lényi Szilvia, Dulai Tibor and Görbe Péter. They assisted me in every possible way and went through all the office works for me to have a good experience in Hungary. I would also like to take this opportunity to thank my great friend Dr Tuboly Gergely and his family for his kindness during my accommodation in Hungary.

I acknowledge and thank the Dean and Deputy Dean of the Faculty of Information Technology, Prof. Hartung Ferenc and Dr. Werner Ágnes, for the financial support under the project EFOP-3.6.1-16-2016-00015. Many thanks to Prof. Zoltan Nagy for giving me access to stroke patient measurements.

My deep thanks to the Egyptian Ministry of Higher Education and Scientific Research and to the Hungarian Ministry of Higher Education for their cooperation with Egypt to have my study in Hungary.

Last but not the least; I would like to thank my family, my parents, whose love and guidance are with me in whatever I pursue. They are the ultimate role models. Most importantly, I wish to thank my loving and supportive wife, Olfat, and my lovely daughter Rokaya who provide unending inspiration.

Mohamed F. Issa, 2020

Abstract

Electroencephalography (EEG) is one of the most frequent tools used for brain activity analysis. Its high temporal resolution allows us to study the brain at rest or during task execution with details not available in traditional imaging modalities. The low cost and simple mode of application enable EEG to be used for studying patient populations to help in the diagnosis and treatment of various brain injuries and disorders such as stroke, Alzheimer's or Parkinson's disease.

Unfortunately, EEG signals are frequently contaminated by undesirable noise and physiological artifacts, which may distort the underlying true neural information and lead to false diagnoses or unreliable experimental data that cannot be used for valid scientific studies. Consequently, artefact removal is a key step in EEG signal processing, and due to the complexity of the problem, it is still an active, open research area. This thesis presents novel methods developed to solve problems in EEG artifact removal. The fully automatic methods allow us to remove eye movement, blink (EOG) and heart-related (ECG) artifacts without using additional reference channels. Independent Component Analysis (ICA) was applied to the measured data, and the Independent Components (ICs) were examined for the presence of both ECG and EOG. An adaptive threshold based QRS detection algorithm was applied to the ICs to identify ECG activity using a rule-based classifier. EOG artifacts were removed from ocular artifact ICs in a selective way using wavelet decomposition minimising the loss of neural information content during the artifact removal process.

The second part of the thesis focuses on functional connectivity methods that allow the construction of resting state and task-related brain activity networks. First, resting state connectivity methods were used to analyse stroke patient brain activity in order to discover potential biomarkers for stroke recovery. Data set was recorded form healthy volunteers and stroke patients during resting state and functional connectivity graphs were created for the delta, theta, alpha and beta frequency bands. A comparison was performed between patients and control subjects as well as between start and end of the stroke rehabilitation period. The results showed differences in the graph degree, clustering coefficient, global and local efficiency that correlate with brain plasticity changes during stroke recovery, and that these can be used as biomarkers to identify stroke severity and outcome of recovery.

To uncover changes in the connectivity network during task execution, Dynamic Brain Connectivity (DBC) methods must be used. Traditional techniques to reveal temporal changes are based on the Short-Time Fourier Transform or wavelet transformation, which have limits on temporal resolution due to the time-frequency localization trade-off. In this work, a high time-frequency resolution method using Ensemble Empirical Mode Decomposition was proposed that generates phase-based dynamic connectivity networks based on the instantaneous frequency of the signals. A comparison with sliding-window techniques was conducted to validate the accuracy of the method. The results showed that the new method can track fast changes in brain connectivity at a rate equal to the sampling frequency.

Összefoglaló

Az EEG (elektroenkefalográfia) az egyik leggyakrabban használt eszköz az agy aktivitásának vizsgálatára. Nagy időbeli felbontásának köszönhetően lehetővé teszi az agy nyugalmi és feladat-végrehajtás közbeni működésének olyan részletességű vizsgálatát, ami más képalkotó módszerekkel nem lehetséges. Alacsony költsége és egyszerű alkalmazhatósága miatt nagy jelentősége van különböző idegrendszeri betegségek és agysérülések (sztrók, epilepszia, Alzheimer és Parkinson betegség) diagnosztikájában és kezelésében.

Sajnos az EEG mérési jelek gyakran tartalmaznak nemkívánatos zajokat és műtermékeket, amik eltorzíthatják az eredeti idegi működésre jellemző információt és így hamis diagnózist adhatnak, vagy az adat annyira megbízhatatlan lehet, hogy az alkalmatlan tudományos vizsgálatokra. Emiatt a zaj- és műtermék-mentesítés egy fontos lépés az EEG jelfeldolgozás során. A probléma komplexitása miatt ez jelenleg is aktív kutatási terület. Ez a disszertáció új műtermék eltávolítási módszereket ismertet, amik a jelenleg ismerteknél jobb eredményeket nyújtanak. A teljesen automatikus eljárások lehetővé teszik a szemmozgások, pislogás és a szívműködés okozta műtermékek eltávolítását a megszokott extra referencia elektródák (EOG, EKG) használata nélkül. Független komponens analízist alkalmazva, a mért adatok független komponensekre bontása után, a szemmozgás és EKG műtermékeket reprezentáló komponenseket azonosítom és eltávolítom. Az EOG műtermék komponens esetén nem a teljes komponenst távolítom el a jelből, hanem wavelet dekompozíciót alkalmazva, szelektíven tisztítom meg a szemmozgás műtermékektől, így minimalizálva a jelben található neurális információ minimális torzulását.

A disszertáció második része a funkcionális konnektivitási módszerekre fókuszál, melyek lehetővé teszik az agyi nyugalmi hálózatok, illetve a feladat végrehajtás közben kialakuló hálózatok feltérképezését. Elsőként a nyugalmi hálózatok létrehozására alkalmas módszereket vizsgáltam meg a sztrók rehabilitációt elősegítő biomarkerek azonosítása céljából. Egészséges és beteg EEG adatok felhasználásával konnektivitási hálózatokat készítettem a delta, théta, alfa és béta frekvencia sávokban. A sztrók beteg nyugalmi hálózatait összehasonlítottam a kontrol személyekével és megvizsgáltam a különbséget a sztrók bekövetkezése után egy héttel és három hónappal. Az eredmények azt mutatják, hogy a konnektivitási gráf fokszáma, a klaszterezési együttható, a globális és lokális hatékonyság korrelál a sztrók alatt lezajló agyi plaszticitás mértékével, és felhasználható biomarkerként a sztrók súlyosságának és a javulás mértékének előrejelzése céljából.

A feladat-végrehajtás agyi mechanizmusainak pontosabb megértését segítheti a dinamikus funkcionális konnektivitás (DBC) módszer alkalmazása. A hagyományos módszerek, melyek a konnektivitási gráf időbeli változásait határozzák meg, általában a rövid idejű Fourier transzformációra (STFT) alapulnak. Ezeknek a pontosságát behatárolja az idő-frekvencia felbontás határozatlansági tulajdonsága. A dolgozatban egy olyan új, nagy időbeli felbontást eredményező módszert fejlesztettem ki, ami az empirikus dekompozícióra alapulva, a jelek azonnali fázis információját képes meghatározni, amiből minden mintavételi időpillanatra meg lehet határozni a funkcionális konnektivitási gráfot. A csúszóablakos módszerrel történő összehasonlítás eredménye megmutatta a módszer pontosságát és alkalmazhatóságát gyors agyi folyamatok hálózatainak vizsgálatára.

List of abbreviations

BDN	Brain Dynamic Connectivity
BSS	Blind Source Separation
CSD	Current Source Density
DAR	Delta/Alpha power Ratio
DTF	Directed transfer function
dwPLI	debiased weighted Phase Lag Index
EAS	Ensemble Average Subtraction
EC	Effective Connectivity
ECG	Electrocardiography
EEG	Electroencephalography
EEMD	Ensemble Empirical Mode Decomposition
EMD	Empirical Mode Decomposition
EMG	Electromyography
EOG	Electrooculography
FC	Functional Connectivity
fMRI	Functional Magnetic Resonance Imaging
ICA	Independent Component Analysis
MIT/BIH	MIT-BIH Arrhythmia Database
PDC	Partial directed coherence
RMSE	Root Mean Square Error
SC	Structural Connectivity
Sen	Sensitivity
SNR	Signal-to-Noise Ratio
Spe	Specificity
WC	Wavelet Coherence
WNN	Wavelet Neural Network
WT	Wavelet Transform

Table of contents

1 Introduction

Electroencephalography (EEG) is a non-invasive method used to measure the bioelectric activity of the brain using electrodes placed on the scalp. The simplicity of the measurement and the high temporal resolution of the recorded signal make EEG essential e.g. in epilepsy diagnosis, cognitive or sensorimotor experiments, where rapid activity changes must be examined. The source of the activity is the change in the postsynaptic potentials of cortical neurons acting as tiny current generators placed in a direction perpendicular to the cortical surface. When a sufficiently large population of nearby neurons is activated simultaneously, the generated current fluctuations cause detectable changes in the electrical field of the brain [1].

The scalp potential distribution, generated by this electric field, can be measured by a suitable EEG measurement device and a set of scalp electrodes, and can be stored in a computer for later processing and analysis. The number and layout of the electrodes used in practice can vary greatly, but high-density 64 or 128-electrode systems arranged in the universal 10/10 or 10/5 layout [2] are the most common in research laboratories. The main advantage of EEG over other brain imaging methods (e.g. fMRI, PET) is its superior temporal resolution. Typical EEG sampling rates are in the range of 512 to 4096 Hz, which enable us to follow the time course of brain activity at millisecond or sub-millisecond resolution.

1.1 EEG Artifacts

The measured EEG signals are regularly contaminated by equipment and environmental noise as well as artifacts caused by extracerebral physiological sources. Among the latter types, ocular, muscle and cardiac artifacts are especially problematic due to their high amplitude and non-periodic (ocular, muscle) or quasi-periodic (cardiac) nature. Other kinds of artifacts generate physical noises that appear as power line noise or variations in electrode-skin conductivity. Artifacts can easily turn valuable EEG measurements unusable. The quality of measured data can further reduce due to the presence of low-quality sensors (electrodes) or bad trials. A trial here refers to a data segment whose location in time is typically locked or related to certain experimental protocol. In other cases, in a task-free protocol such as resting state, a trial represent a data segment of certain length of time.

Ignoring the presence of low-quality data (a bad trial or bad sensor, etc..) can have an adverse effect on downstream performance of the desired experiment. For example, when averaging multiple trials time-locked to the stimulation to estimate an evoked response, a single bad trial can corrupt the final averaged EEG signal. Bad channels are also potential problems, as artifacts present on a single bad sensor can spread to other sensors due to spatial projection. Normal filtering techniques [3] can often suppress many low frequency artifacts, but turn out to be insufficient for broadband artifacts since the artifacts usually have frequencies overlapping with the signal frequency, which makes artifact removal a key step in every EEG processing pipeline.

Early attempts to remove ECG artifacts from EEG included subtraction and ensemble average subtraction (EAS) [4] methods. Current mainstream methods are based on adaptive filtering [5,6] and blind source separation such as Independent Component Analysis (ICA) [7,8] which is

widely used in the field of EEG signal processing for artifacts suppression, since it can separate a signal mixture into its main sources, such as EOG, ECG, EEG, etc. components. Wavelet transform (WT) is increasingly used [9,10] in the EEG noise removal and it is more often used in combination with (ICA)-based methods [11,12].

The simplest method is to discard parts of the data that are contaminated by artifacts. This approach requires visual inspection and manual rejection of artifact contaminated data segments or epochs. This is a labour-intensive task that requires a trained expert to go through each individual dataset to mark artifacts, and it excludes the possibility of automatic and high-speed analysis of large-scale EEG experiments. Although the annotation of bad EEG data is likely to be accepted by trained experts, their decision is subject to variability and cannot be replicated. Their assessment may also be skewed due to prior experience with specific experimental setup or equipment, not to mention the difficulty these experts have in allocating enough time to review the raw data collected daily.

Since visual inspection is slow, tiring and requires an expert assistant, several authors proposed methods for semi or fully automatic component detection, which resulted in automated analysis pipelines [13]. The automation approach not only saves time, but also allows flexible analysis and reduces the barriers to reanalysis of data, thus facilitating reproducibility. One semi-automated method using ICA for identifying artifact components is presented by Delorme et al. in [14]. Various statistical measures (entropy, kurtosis, spatial kurtosis) are calculated for each independent component to label them automatically as artifact, but validation and rejection is performed manually. Since the method is based on statistical analysis of the components, which does not consider the physiological model of artifacts, the performance of the method is not perfect. A similar statistical approach is followed in the FASTER [15] and ADJUST [16] artifact removal toolboxes.

Brainstorm, EEGLAB, FieldTrip, MNE,[17–20] are popular tools used for rejection of EEG artifacts based on simple metrics such as differences in peak-to-peak signal amplitude that are compared to a manually set threshold value. When the peak-to-peak amplitude differences in the EEG exceeds a certain threshold, the given segment is considered bad that should be excluded from the experiment. Kurtosis, standard division, mean, skewness etc. are used to set the proper threshold and remove the peaks or trials greater than the threshold e.g. trial has kurtosis >5 is rejected. Although this seems to be very easy to understand and easy to use from the point of view of a practitioner, it is not always convenient. Moreover, a good peak-to-peak signal amplitude threshold is data-specific, meaning that setting it involves a certain amount of testing and error. Rejection of data epochs can result in significant loss of data which in turn can have adverse effects in Event Related Potential (ERP) studies. Using only a small number of remaining epochs can result in critically low signal-to-noise ratio.

More sophisticated artifact removal methods rely on cross-correlation based filtering which require the use of reference channels, in the form of e.g. horizontal-vertical eye movement (EOG) or ECG electrodes. These can be acceptable in strictly controlled laboratory situations, but extra electrodes can be problematic in clinical settings due to patient discomfort or interference with other equipment. Numerous researches have therefore been directed towards creating automatic artifact removal methods that work without external electrodes and can be performed without manual inspection. The most successful ones of such methods are based on the application of Independent Component Analysis (ICA) [8] that can separate a signal mixture into its original sources or components, based on the condition of statistical independence.

Bad channel artifacts generate high amplitude and non-periodic signal effects, which distort raw EEG data, making EEG calculations untrustworthy. Rejecting the trial which has drifts is not practical solution because if there is one bad channel displayed on the data, it means most of the trials would be rejected [21]. Consequently, only the bad channel has to be automatically marked and interpolated to avoid rejecting entire trials. The traditional artifact removal approach based on visual inspection has no standard measure from one to another about how we define and reject the artifacts. In the manual inspection protocol, the electrode offset has to be checked before starting the real experiment to mark the bad channels. The pre-defined information about the bad channel list needs to be updated if one of the channels contains bad records in the middle of the measurements, and this can be hard to detect during the recordings if no significant variance can be detected in the channels.

In this thesis, fully automatic methods for removing EOG and ECG artefacts from EEG signals are proposed. A new wavelet-based method is presented for EOG artifact removal that cleans EOG independent components selectively, leaving non-contaminated parts of the component untouched. The novel ECG artefact removal algorithm uses a sophisticated approach to identify automatically the ECG components without the need for a reference ECG channel, thus it can be used in situations where ECG data is not available. The method can also detect and remove ECG artefacts generated by pathological cardiac activities which makes the method more robust when analysing EEGs of elderly patient. The results show that the proposed methods outperform state-of-the-art methods for EOG-ECG removal in its accuracy both in the time and the spectral domain, which is considered an important step towards the development of accurate, reliable and automatic EEG artifact removal methods.

1.2 Brain Connectivity

The human brain comprises close to hundred billion neurons, each establishing several thousand synaptic connection matrices which can be mathematically modelled in several scales micro-meso-macro-scale levels, with nodes or regions and links. Connectivity refers to the anatomical connected patterns (networks pathways) of the nervous system ("anatomical connectivity"), which have statistical dependencies ("functional connectivity") or these patterns have causal interactions ("effective connectivity") between distinct regions within a nervous system. To go beyond these networks and decode the meaning of connectivity links between the nervous cells or regions is one of the goals of neuroimaging. Studying these links is crucial to elucidating the strength of connection and describing the direct and indirect information flow at different scales such as individual synaptic neurons at the microscale or pathways between regions at the macroscale. Properties of the connectivity network may help in deciding whether certain neural regions are normal or contain unexpected features caused by functional deficits or neuropsychiatric disorders.

Through identifying anatomical and functional associations of brain regions on the same map using an integrated approach, brain mapping techniques, network analysis becomes a powerful tool for investigating structural-functional mechanisms. It is able to present the brain connectivity and to reveal etiological relationships that link abnormalities of connectivity with neuropsychiatric disorders.

1.3 Brain Connectivity Biomarkers of Diseases

Ischemic stroke is one of the major causes of death or permanent disability with increasing frequency of occurrence as the population in developed countries is aging. Prompt and effective treatment can speed up recovery and improve rehabilitation outcome. Timely treatment of stroke starts with an MRI and/or CT scan to identify the location and extent of brain damage. After diagnosis, treatment starts and the condition of the patient is monitored by the medical staff based on external symptoms using standardized stroke scales (NIHSS, BI, etc.) [22,23]. A second MRI scan might be performed on patient dispatch to confirm recovery status. Unfortunately, complications can develop in the hospital, e.g. Delayed Cerebral Ischemia (DCI), which can only be discovered once symptoms worsen [24]. Also, efficiency of the treatment is difficult to assess without monitoring quantitative stroke metrics. These metrics could help in selecting the best treatment path, and be used as predictors for the level of recovery at the end of the rehabilitation period [25–28].

Continuous monitoring of patients and the use of mainly frequency-domain quantitative measures have already been suggested [28–31]. It is known that these metrics can detect stroke-related status changes well before symptoms develop [28]. The reported methods all rely on the calculation of a single metric from measurements using a standard 19-electrode clinical EEG system. This process could be more efficient with using high density electrode-cap of 128 or 256 channels with more metrics describing the properties in-between the different brain regions.

This thesis develops brain connectivity metrics based on high-density EEG measurements that can depict the location and extent of stroke lesions similar to MRI scans. Monitoring brain connectivity changes could help in verifying treatment effectiveness as well as measuring progress of recovery. A comparison of connectivity measures is performed between patients and control group as well as between start and end of the stroke rehabilitation interval. The results show differences in the small-world, graph degree, clustering coefficient, global and local efficiency metrics that correlate with brain plasticity changes during stroke recovery and can be used as biomarkers to quantify stroke severity and outcome of recovery.

1.4 High Resolution Brain Connectivity

Precise and accurate analysis of the non-stationary spectral variations in EEG is a long-standing problem. Dynamic Functional Connectivity (DFC) is an emerging subfield of functional brain connectivity analysis whose goal is to uncover and track the changes in functional connectivity over time. Traditional connectivity methods assumed that the connectivity network representing cortical activity is stationary. Dynamic connectivity can provide new insights about the large-scale neuronal communication in the brain and help to track the progress of recovery of many neurological disorders and brain diseases such as epilepsy, Alzheimer’s disease, stroke, and predict outcome to many other deficits related to the brain. The crucial part of calculating DFC is the time-frequency decomposition.

The Fast Fourier Transform (FFT) has been used to efficiently estimate the frequency content of a discrete and finite time series but it assumes the input signal is stationary. The most important issue in the time-frequency analysis of an EEG signal is the principle of uncertainty, which stipulates that one cannot locate a signal with an absolute precision both in time and frequency. Over the past 30 years, several methods have been developed to extend Fourier's research to non-stationary signals, resulting in a body of work called "time-frequency" (TF) representation

methods. They include linear TF methods as Short Time Fourier Transform (STFT), Wavelet Transform (WT) that involve phase and magnitudes contributions.

The Short-time Fourier and the wavelet transforms also show some resolution limitations (localization limit) due to the trade-off between time and frequency localizations and smearing due to the finite size of their templates. STFT is the extension of FT which was modified to show nonstationary components of the signal in time. It is indeed the FFT of the successive, overlapped windows of the signal, where each frequency distribution is being correlated with each window's central time. Usually there is a peak smeared around the peak of the main frequency with decaying side lobes on the selected window. However, side lobes attenuation is associated with increasing of the window [32]. The spectral smearing can be reduced by increasing the length of the time window, but this also reduces the time localization accuracy by imposing increased stationarity. Thus, high time localization comes at the expense of the spectral smearing.

Wavelet transformation was established for the time varying spectral estimate to overcome the spectral smearing. It uses variable time window lengths which are inversely proportional to the frequency of the central target. So, long windows used for low frequencies therefore have good frequency, but limited time, while short windows used for high frequencies have good time but limited range of frequency resolution [33]. WT showed accepted temporal resolution on the high frequencies, while poor temporal resolution was located in the low frequencies [34]. The chosen wavelet function should be carefully selected with specific characteristics to improve the signal representation.

Functional connectivity emerging from phase synchronization of neural oscillations of different brain regions provides a powerful tool for investigations. While the brain manifests highly dynamic activation patterns, most connectivity work is based on the assumption of signal stationarity. One of the underlying reasons is the problem of obtaining high temporal and spectral resolution at the same time. Dynamic brain connectivity seeks to uncover the dynamism of brain connectivity, but the common sliding window methods provide poor temporal resolution, not detailed enough for studying fast cognitive tasks. In this work, I propose the use of the Complete Ensemble Empirical Mode Decomposition (CEEMD) followed by Hilbert transformation to extract instantaneous frequency and phase information, based on which phase synchronization functional connectivity between EEG signals can be calculated and detected in every time step of the measurement. The work demonstrates the suboptimal performance of the sliding window connectivity method and shows that the instantaneous phase-based technique is superior to it, capable of tracking changes of connectivity graphs at millisecond steps and detecting the exact time of the activity changes within a few milliseconds margin. The results can open up new opportunities in investigating neurodegenerative diseases, brain plasticity after stroke and understanding the execution of cognitive tasks.

1.5 Thesis Organization

This section describes the structure of the thesis, starting from **Chapter 2** which presents an introduction to the characteristics of EEG, the measurement process and required equipment, and the steps to record an acceptable EEG measurement. Then, it gives an overview about the pre-processing approaches used in EEG signal processing.

Chapter 3 starts with defining the different types of EEG artifacts, which can be formed by biological or external sources, followed by an overview of the state-of-the-art techniques for EEG artifacts removal.

In **Chapter 4,** I provide an improved, fully automatic ICA and wavelet based EOG artifact removal method that cleans EOG independent components selectively, leaving other parts of the component almost untouched.

A novel automatic method for cardiac artifact removal from EEG is discussed in **Chapter 5**. Both proposed methods work without manual intervention (visual inspection), and thus accelerates pre-processing steps and lay the groundwork for potential online and real-time EEG analysis (e.g. BCI and task related application, finger tapping, visual - auditory evoked potentials).

A high-resolution EEG technology as an aid for monitoring and quantifying patient recovery progress, complementing the use of clinical stroke scales is introduced in the first part of **Chapter 6.** Connectivity network metrics are calculated as an aid for monitoring and quantifying patient recovery progress, complementing the use of clinical stroke scales. It shows changes of functional connectivity measures in stroke patients to identify reliable biomarkers that characterize progress of recovery and predict outcome. To overcome the trade-off between time and frequency resolution and localization smearing, in Chapter **7**, I propose the use of the Complete Ensemble Empirical Mode (EEMD) Decomposition followed by Hilbert transformation to extract instantaneous frequency and phase information. The results showed that the introduced method is able to track the fast-dynamic brain connectivity changes in time and frequency resolution at rate of sampling frequency.

Finally, in **Chapters 8** and **9**, I conclude the results of the thesis work and list my publications related to the presented work**.**

2 Introduction to EEG signal Processing

I start this chapter with discussing the characteristics of EEG data, the process of EEG measurements, the equipment needs for the measurement, and the steps to record an accepted EEG measurement. Then, I give an overview of the pre-processing approaches used with EEG measurements, the extracted features used to show the characteristics of the measured signal in the time and frequency domain and the concept of source localization and brain connectivity and their impact for neuroimaging sciences.

The history of EEG started around the end of the 19th century when an English researcher, Richard Caton (1842–1926) was able to detect electrical impulses of the brain using the exposed cortex of monkeys and rabbits [35]. He used a sensitive galvanometer to detect the fluctuations of the brain in different stages, sleep and absence of activity following death. Adolf Beck, (1863-1939), a Polish physiologist did similar measurements, followed by Russian physiologist Pravdich-Neminski (1879-1952) who presented a photographic record. The German psychiatrist Hans Berger [36], in 1924, was the first researcher who recorded EEG measurements from a human. This led to measurements on epileptic patients (Fisher and Lowenback, 1934). Gibbs, Davis, and Lennox [37] in 1935 described interictal epileptiform discharge wave patterns during clinical seizures. The English physician Walter Grey in the 1950's developed EEG tomography which provided a means for mapping electrical activity across the surface of the brain. It gained its prominence during the 80's primarily as an imaging technique in research settings.

2.1 Overview of the Measurement Process

The measured EEG signal is the sum of all the synchronous activity of all cortical sources including areas potentially far away from a given electrode. The scalp potential distribution, generated by this electric field, can be measured by a suitable EEG measurement device and a set of scalp electrodes, and can be stored in a computer for later processing and analysis. The recording system consists of electrodes, amplifiers with filters, A/D converter and recording device. Electrodes are used to record the signal from the head surface, then the recorded signals are fed into amplifiers. The signals are converted from analogue to digital form, and finally, a computer displays and stores the obtained data.

Electrodes


EEG Instrument (A/D box)

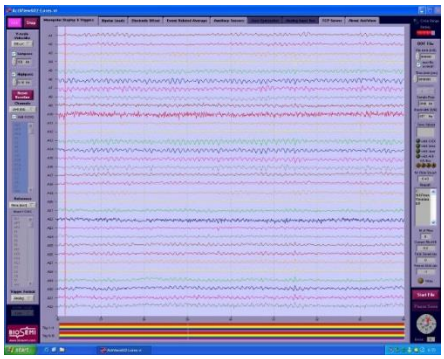
Graphical output

Figure 2-1: Main components of an EEG measurement system[1].

There are different types of electrodes, reusable disc electrodes, electrode caps, needle electrodes and saline-based electrodes. Each one of it has its own function; for example needle electrodes

[1] image source: https://www.biosemi.com/.

are used invasively where they are inserted under the scalp for long recordings while electrodes cap are preferred for multichannel montages, where they are installed non-invasively on the scalp surface. Commonly, scalp electrodes consist of Ag-AgCl disks, of diameter between 1 to 3 mm, and long flexible leads are plugged into an amplifier. The number of electrodes used in practice varies. In clinical practice, 19 electrodes are used. In research experiments, 32 to 256 electrodes may be used. There are several electrode layouts in use, such as the 10/20, 10/10 or 10/5 international systems, or the Biosemi ABC radial layout [2] as shown in Figure *2-2* and Figure *2-3* . The channel configurations can comprise up to 64 -128 or 256 active electrodes.

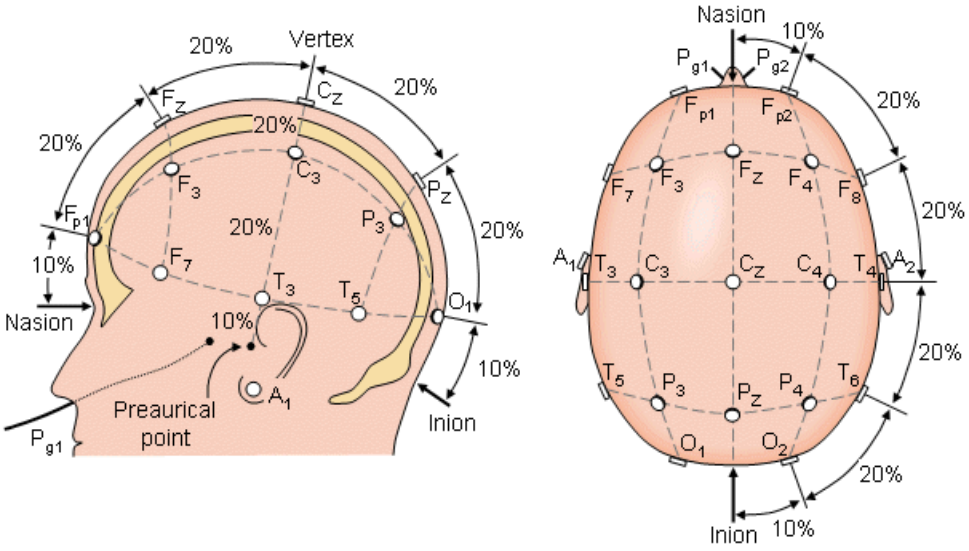

Figure 2-2: The international 10-20 electrode layout.

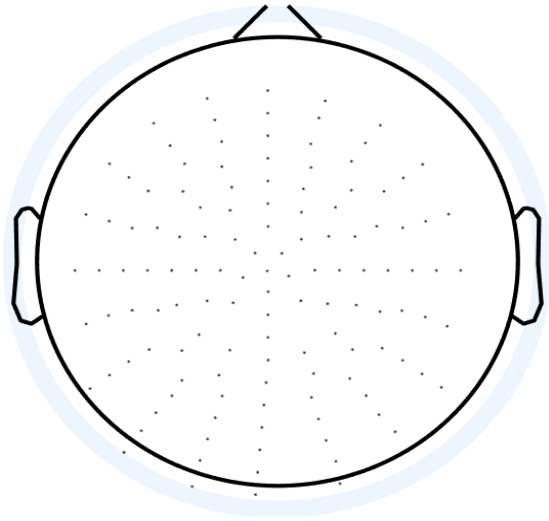

Figure 2-3: Biosemi cap, 128-channel ABC radial layout.

The main advantage of EEG over other brain imaging methods (e.g. fMRI, PET) is its superior temporal resolution. Typical EEG sampling rates are in the range of 512 to 4096 Hz, which enable us to follow the time course of brain activity at millisecond or sub-millisecond resolution. The head is made up of various tissues (white and grey matter, cerebrospinal fluid, skull, scalp) with varying conductivity properties. When the generated current flows from the cortex to the scalp, it must pass through the skull which has a relatively low conductivity (high resistivity). As a result, the current spreads out laterally within the skull instead of passing straight through to the scalp. The result of this so-called volume conduction effect is the reduced spatial resolution and

the ‘smeared’ or ‘blurred’ appearance of activation sources on the scalp potential distribution image.

EEG is widely used in many applications as part of diagnosis and monitoring of epilepsy [38], Parkinson's disease [39], Alzheimer’s disease [40], Huntington's disease [41], events detection in healthy human sleep EEG [42], brain-computer interface (BCI) [43] and can help in the localisation of the exact cortical source of the activity or disease [44].

2.2 EEG Processing Pipeline

EEG data is normally processed in a pipeline fashion, starting with data pre-processing including filtering, artifact removal, re-referencing, followed by feature extraction (Event-Related Potential, time-frequency, cortical source or connectivity features) followed by classification or pattern recognition.

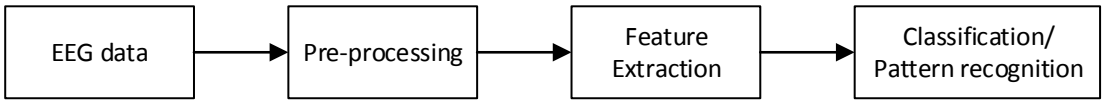

Figure 2-4: EEG processing pipeline

2.2.1 Pre-processing

One of the most critical steps to obtain a clean EEG data is the pre-processing phase. Noise, unwanted artifacts, and other disturbances must be removed from the signal in order to produce reliable results. The EEG signal can contain physiological and non-physiological noise and artifacts, e.g. effects of eye and body movements, muscle contraction induced noise, heart and pulse artifacts, superimposed mains power line noise of 50 or 60 Hz and its harmonics, and amplitude variations by changes at the tissue/electrodes interface (due to skin resistance variation or contact problems).

Bandpass/band stop filtering is one of the classical and simple attempts to remove artifacts from an observed EEG signal. This method works reliably only when the artifacts have a narrow frequency band, e.g. power line artifact (50/60 Hz, see Figure *3-1*), and the spectrum of the artifacts do not overlap with the signal frequency. Band pass filtering from 0.1 to 70 Hz is used to initially to keep only the meaningful frequency range of the EEG signal. However, in some cases, fixed-gain filtering is not working efficiently for biological artifacts because it will attenuate EEG interesting signal and change both amplitude and phase of signal [45]. Adaptive filtering [46] is an alternative approach to the normal filtering method, which assumes that the EEG and the artifacts are uncorrelated, and the filter parameters are adjusted in a feedback loop. Adaptive filtering, however, requires a reference signal for correct operation.

Wiener filtering is considered also an optimal filtering technique used as the adaptive filtering. It uses a linear statistical filtering technique to estimate the true EEG data with the purpose to create a linear time invariant filter to minimize the mean square error between the EEG data and the estimated signal [47]. Since there is no a priori knowledge on the statistics [48], the linear filter estimates the power spectral densities of the observed signal and the artifact signal, moreover it eliminates the limitation of using extra reference channels, but the requirement of calibration can add the complexity of its application.

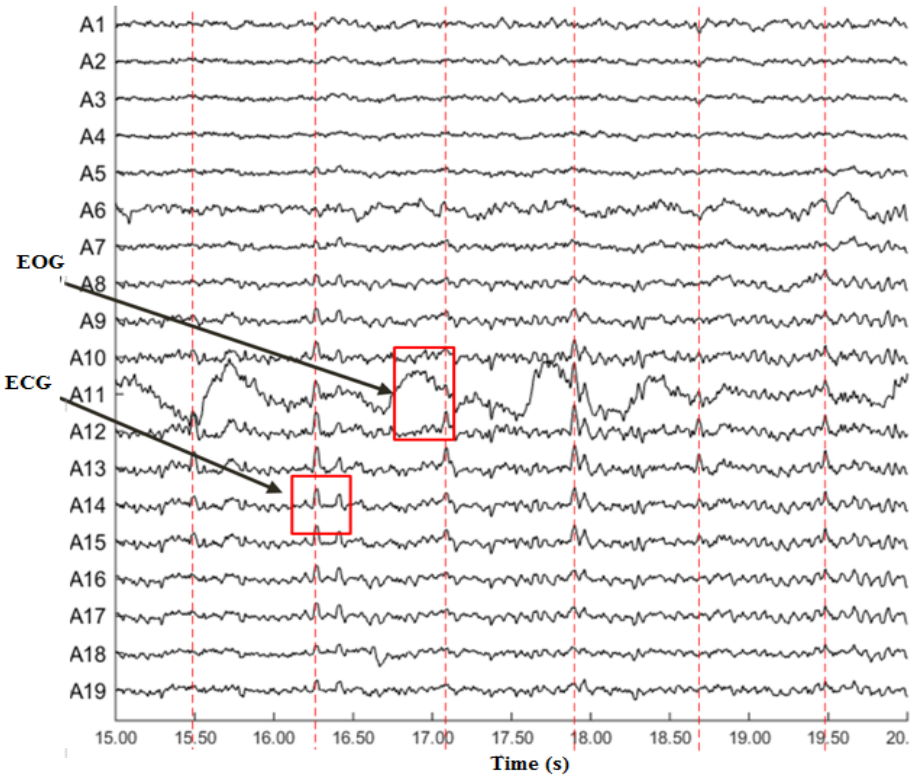

Figure 2-5: EEG raw data contaminated with EOG and ECG artifacts.

Since the electrical potential of the physiological artifacts have frequency characteristics overlapping with the EEG signal, the removal of such kind of artifacts needs more efficient methods since the traditional signal processing techniques such as normal filtering method fail to clean them. Researchers have developed different methods for artifact removal, including adaptive filtering and component-based method. In the adaptive filtering-based method, a recursive algorithm is used for updating filter coefficients. The coefficients are modified until the output has been minimized according to a given signal property (e.g. time and frequency domain features) to remove the noises out of the signal [45]. Thus, a reference signal, has to supplied besides the recorded signal (Figure *2-6*).

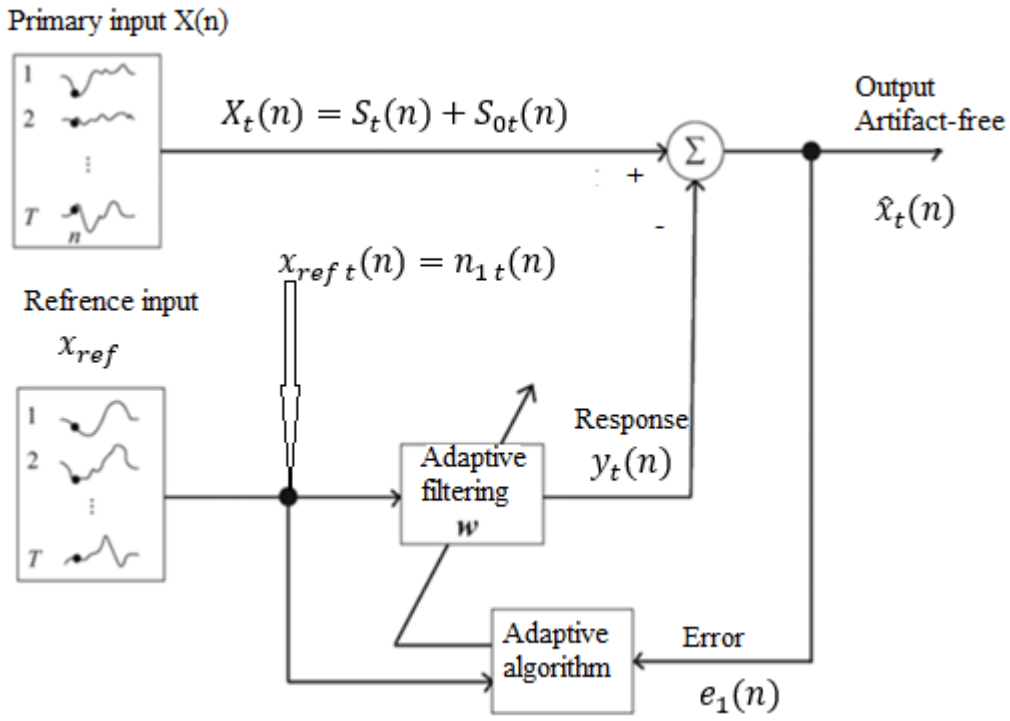

Figure 2-6: Overview of the adaptive signal filtering method [46].

Independent Component Analysis (ICA) is one of the component-based approaches that are commonly used in the pattern analysis and biosignal analysis [49]. ICA is able to separate the artifacts from the signals by decomposing the EEG signals into several independent components based on statistical independence of signals. One of the main advantages of this method that it does not need an external reference channel, as the algorithm itself does not need a priori information. Once the signal is decomposed into independent components, one or more components will represent the artifacts. If these components are removed before reconstructing the signal from the components, we will get an artifact-free signal. There are two methods for identifying and removing artifact components, i) manual visual inspection where an expert searches for the bad component to reject, and ii) automatic detection where the component is compared with a pre-defined threshold [15,50]. The manual component inspection is time consuming and cumbersome. Automatic component detection depends on passing the signal to a sophisticated algorithm using the pre-defined threshold or reference channels to help in identifying artifact components. The details of each method are described in the Chapter 3.

2.2.2 Feature Extraction

After artifact removal, the significant features of the cleaned EEG signals will be extracted by using feature selection methods. The feature extraction and selection methods are important to identify certain properties to be used effectively in classifying the EEG signals. In addition, it also reduces the amount of resources needed to describe a huge set of data accurately. Hence, feature extraction is considered the most critically significant step in EEG data classification. Several methods are used in feature extraction including time-domain, frequency domain and time-frequency domain. In the time-domain, the commonly used features are, mean, minimum, maximum, variance, entropy, etc. The drawback of the time-domain approach is its high sensitivity to variations of the signal amplitude.

In the frequency domain, the signal is transformed into frequency domain using Fast Fourier Transform (FFT). Frequency characteristics are dependent on neuronal activity and grouped into multiple bands (delta:1-4 Hz, theta:4-8 Hz, alpha:8-12 Hz, beta:12-30 Hz, and gamma :>30 Hz) corresponding to a cognitive process. In some cases, frequency characteristics are not enough to provide signal characteristic for classification using only frequency information, which makes the time-frequency domain the alternative to improve the classification performance [51]. These include wavelet transform (WT) which is highly effective for non-stationary EEG signals compared to the short-time Fourier transformation (STFT). Several feature extraction methods have been used based on the time-frequency domain approaches as Power Spectrum Density, Phase Values Signal Energy. Calculating the coherence between the different time-frequency signals refers to an important feature called connectivity. These connectivity features include Magnitude Squared Coherence, Phase Synchronization, Phase Locked Value, etc. The most important issue in the time-frequency analysis of the EEG signal is the principle of uncertainty, which stipulates that one cannot localize a signal with absolute precision both in time and frequency. This principle controls the time-frequency characteristics and is considered as a cornerstone in the interpretation of Dynamic Functional Connectivity (DFC).

2.2.2.1 Event Related Potential (ERP) computation

The amplitude of the EEG signal measured on the scalp is normally within the range of ± 50 μV. The biologically meaningful small-amplitude signal is usually embedded in relatively high level of noise generated by various biophysical sources (muscle activity, ECG, eye movement, blinks), skin resistance changes, electrode malfunction, and so on, making the detection of small amplitude changes difficult. A well-established method for this problem is signal averaging. Assuming that noise is a random process with zero mean, the sample-wise averaging of a sufficiently large number (>100) of EEG trials (time window of task of interest) in a stimulus-synchronised manner will cancel out noise and leave only the stimulus-locked components in the resulting signal [52]. Successful averaging requires very precise synchronisation of the datasets of the repeated experiments; therefore, stimulus presentation and response triggers are used to mark the start and end of the experiment trials. Depending on which trigger is used for averaging, we can distinguish between stimulus or response-locked averaging. The resulting trigger-based average potentials are called event related potentials (ERP). Depending on the applied stimulus type, we can examine visual, auditory, sensory and other cognitive tasks with this method.

The execution of cognitive tasks involves various sensory, cognitive and motor processes. The sum of these processes appears in the averaged ERP waveforms in the form of components. Components are distinct positive or negative potential peaks, as illustrated in Figure *2-7*, named by the polarity (negative/positive) and the order or time stamp of the peak, e.g. N1, N2, P1, etc. or N100, P300 or P500. The analysis of these waveforms allows us to compare ERPs obtained under different conditions and consequently test scientific hypotheses.

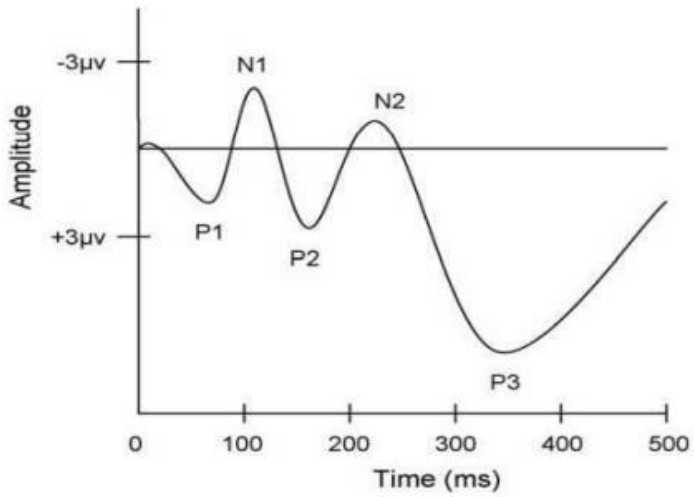

Figure 2-7: Typical ERP components: positive and negative peaks designated by their order P1, P2, P3 or the time they appear, e.g. P100, N400. ERP is often displayed with reversed polarity showing negative peaks pointing upwards. (Source: https://en.wikipedia.org/wiki/ Event-related potential).

2.2.2.2 EEG Source Localization and Connectivity

EEG source localization can be used to uncover the location of the dominant sources of the brain activity using scalp EEG recordings. It provides useful information for study of brain's physiological, mental and functional abnormalities by solving inverse problem. The process involves the prediction of scalp potentials from the current sources in the brain (forward solution) and the estimation of the location of the sources from scalp potential measurements (termed as inverse solution) [53]. The accurate source localization is highly dependent on the electric forward solution which includes, head model, the geometry and the conductivity distribution of the model tissue sections (scalp, skull, brain grey, cerebrospinal fluid, and white matter, etc.).

In EEG connectivity analysis, methods based spectral coherence such as Phase Lock Value, Phase Lock Index, etc. [54] replace amplitude correlation to mitigate the effect of noise and reduce spurious connections caused by volume conduction. Connectivity can be computed in the sensor (electrodes) space or in the source (cortex) space. Connectivity in source level requires accurate 3D head models and sophisticated inverse problem solvers needs it also requires a lot of complicated work includes first doing forward solution which needs information about the anatomical structural of the brain as:

- Head model which contains the voxels and the connectivity of the brain layers.
- Source model: which contains the information about the dipole's positions and orientations.

The above steps need information about the anatomical data and anatomical marks to align the sensors with the anatomical marks before starting source reconstruction. Preparing the head model dependent on the used method for preparing the volume conduction such as Boundary Element Method (BEM) and Finite Element Method (FEM). BEM calculates the model on the boundary of the head (scalp, skull, brain), while FEM calculates the model on all points of the head. The calculation of the connectivity is slow due to many arguments need to be defined. The increasing in the source depth deteriorates the accuracy of the connectivity estimations due to the decreased accuracy of source localization and size. A problem of source reconstruction in EEG is that the sources may not be fully spatially determined, but rather are smeared out across a

relatively large brain volume. This problem arises mainly from inaccurate forward solution and the ill-posed nature of the inverse EEG problem, which projects data from relatively few electrodes to many possible source locations. This might result in two uncorrelated sources having their reconstructed time courses erroneously correlated. Ignoring this can artificially inflate the level of connectivity between two sources. The way leakage propagates across the source space is non-trivial, and solutions are required to be implemented to decrease this effect on functional connectivity [55]. Since connectivity in the source space cannot be calculated without the anatomical information of the brain, calculating connectivity in sensor space is a much faster approach, however, with reduced spatial resolution.

2.3 Current State-of-the-Art Methods

Event-related and time-frequency analysis methods can be used to verify hypothesis based on various experimental conditions and to explore the temporal/spectral/spatial characteristics of the EEG data. Time-frequency analysis methods provide a more advanced set of tools that provide information of activity in different frequency bands and lend themselves naturally to the examination of oscillations and phase properties of the given cognitive process. It allows us to better separate the components of a task that contain perceptual, cognitive and decision subtasks. Time-frequency analysis results also more naturally connect with neural mechanisms at lower spatial scales. They do not, however, provide information about the nature and operation mechanisms of the distributed cortical networks underlying the given cognitive processes. On the other hand, finding the correlation between the calculated frequency characteristics give a clear insight where understanding brain function involves not only gathering information from active brain regions but also studying functional interactions among neural assemblies which are distributed across different brain regions. This frequency correlation is well known as brain connectivity and widely used to aid diagnosis of neural and brain diseases such as stroke, Alzheimer's disease, epilepsy, etc. It provides important biomarkers for understanding pathological underpinnings, in terms of the topological structure and connection strength and opens the way to the network analysis which has become an increasingly useful method for understanding the cerebral working mechanism and mining sensitive biomarkers for neural or mental problems as language processing [56,57].

Connectivity analysis, the collections of methods for investigating the interconnection of different areas of the brain – provides the theoretical basis as well as the practical tools describing the operation of these networks [58]. Different areas of the brain are connected by neural fibres or tracts of the white matter, transmitting information between distant brain regions. This type of connectivity, the Structural Connectivity, describes the anatomical connections in the brain. Diffusion Tensor Imaging [59] can be used to detect anatomical fibres and construct structural networks. Structural connectivity, however, presents a rather static and limited view of the brain; it cannot fully describe the short-range, dynamic and plastic interconnection and activation mechanisms found in brain processes. Functional and Effective Connectivity networks provide this crucial additional information for us [60]. Functional Connectivity describes the temporal correlations in activity between pairs of brain regions. The connectivity may reflect linear or nonlinear interactions, but it ignores the direction of the connection. Effective Connectivity, on the other hand, uses measures that enable it to describe causal influences of one region on another, hence explore dependencies in our network.

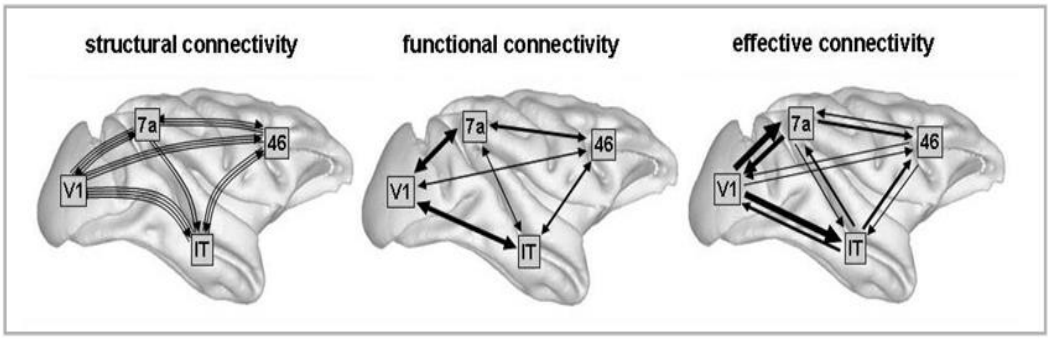

Figure 2-8: Varying information content extracted by different connectivity analysis methods[2].

Connectivity is described by networks, which are in fact graphs, consisting of nodes (brain regions) and edges (connections) [61]. Nodes ideally should represent coherent structural or functional brain regions without spatial overlap, while links represent anatomical, functional, or effective connections (link type) but can also have weight and direction associated with them. Binary links only represent the presence or absence of a connection. Weighted links, on the other hand, can represent various properties. In anatomical networks, weights may represent the size, density, or coherence of anatomical tracts, while weights in functional and effective networks may represent respective magnitudes of correlational or causal interactions. In functional and effective connectivity networks, links with low weights may represent spurious connections that obscure the topology of strong connections. These can be filtered out using suitable thresholding policies.

To use these constructed networks in a quantitative manner, network measures/metrics are needed [61]. Measures can characterise the properties of local or global connections in the network, detect various aspects of functional integration and segregation, or quantify importance of individual brain regions. Measures exist at the individual element level or globally as distributions of individual measures. The degree of a node is the number of its links, i.e. the number of its neighbours, representing the importance of a node. The degrees of all nodes create a degree distribution which is important to describe e.g. the resilience of the network. The mean of this distribution gives the density of the network. Other measures, e.g. the number of triangles in the network, or the number of triangles around a given node (clustering coefficient) describe the level of functional segregation – the presence of functional groups/clusters – in the network. Path length and average shortest path length provide information about the ability of the network to combine information quickly from distant brain regions. Further specific measures can be found in [61].

[2] image source: http://www.scholarpedia.org/article/Brain_connectivity

3 Literature review of EEG artifacts and possible removal

This chapter starts with defining the different types of EEG artifacts, which can be formed by biological and external sources, then it gives an overview of the state-of-the-art used techniques for EEG artifacts removal. Since the measured EEG signals are regularly contaminated by ocular EOG, and cardiac artifacts (ECG) that are especially problematic due to their high amplitude and non-periodic (ocular) or quasi-periodic (cardiac) nature, they can easily turn valuable EEG measurements unusable. Thus, I focus here on the state-of-the-art used techniques for removing the EOG-ECG artifacts from the EEG signal.

3.1 Noise and Artifacts

The measured EEG signals are regularly contaminated by equipment and environmental noise. These noises vary between physiological or non- physiological sources. The non-physiological sources are represented by power-line noise, bad location of electrodes, unclean scalp, varying impedance of electrodes over the head, etc. as shown in Figure *3-1*and Figure *3-2*.

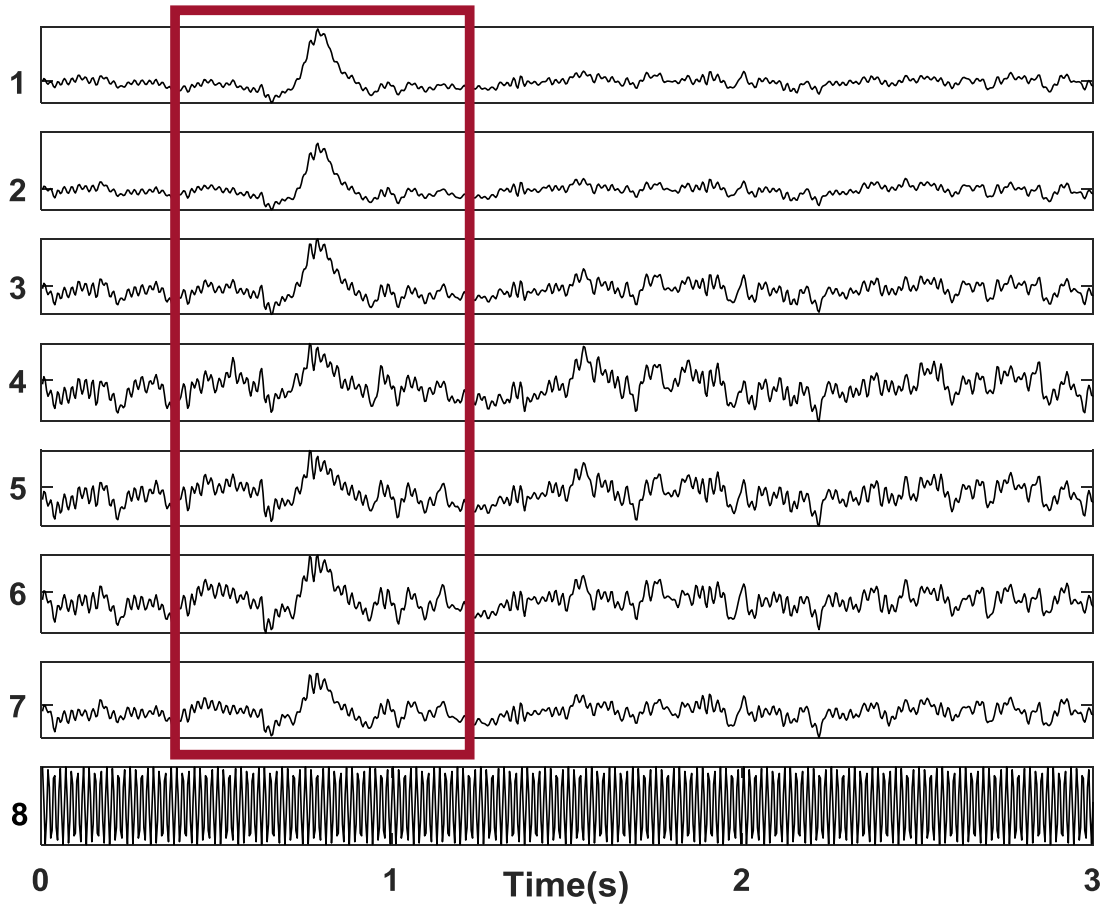

Figure 3-1: 60 Hz power line noise on channel 8 (affecting channels 1-7) and EOG artifacts (red highlight) spread over channels 1 to 7 (PhysioNet dataset- s01 rc02) [62,63].

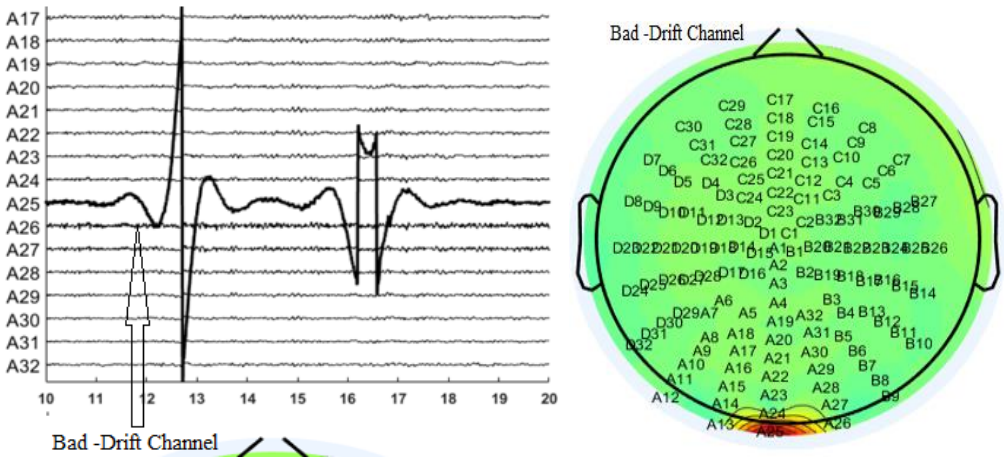

Figure 3-2: Illustration of a bad channel in a recording (electrode A25: potential drift, left panel) and its appearance in the scalp potential distribution (red spot in the topoplot on the right panel).

The second kind of artifacts caused by extracerebral physiological sources such as ocular, muscle and cardiac artifacts that are especially problematic due to their high amplitude. The artifacts are either non-periodic (ocular- vertical or horizontal eyes movements, muscle) or quasi-periodic (cardiac) nature that can easily turn valuable EEG measurements unusable. Eye blinks - eye movements are the most common artifacts in EEG recordings. Eye movement generates changes in the resting potential of the retina during eye- movements and eye- blinks, besides the muscle activities of the eyelid within blinks produces disturbances in EEG recordings. The amplitude of EOG is generally much greater than the EEG and its frequency spectrum overlaps that of the EEG signals. They are mainly presented in low frequency components of the EEG, that is in between 2-10 Hz.

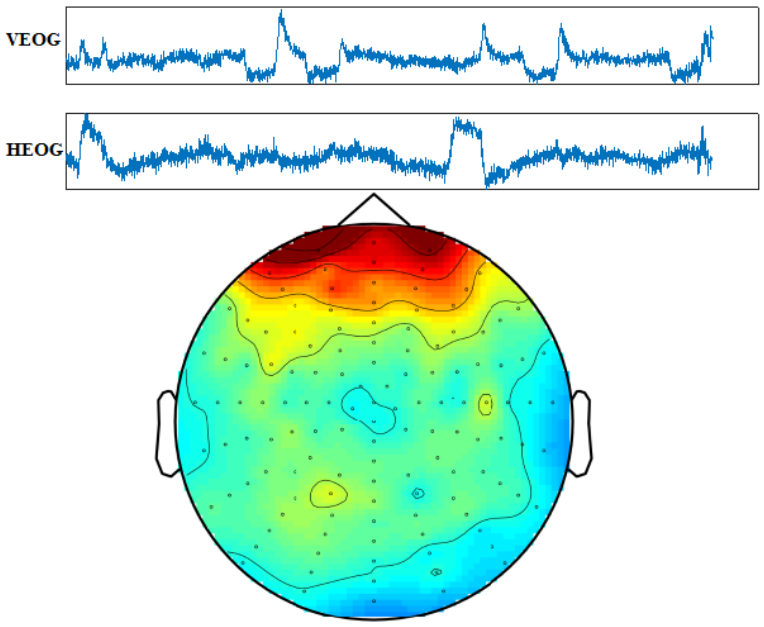

Figure 3-3: EOG physiological artifacts (horizontal and vertical eye movements) in the independent component (IC) space and their typical frontal high-amplitude pattern.

The heart also generates an electrical signal which can be recorded in numerous locations on the body, including the head which is called electrocardiograph (ECG) and has frequency band 0.5 - 100 Hz that overlaps with the EEG frequency [64]. Also, the heart during beating produces

artifacts that stem form voltage changes as blood vessels contract and and expand. This also generates low frequency components in the range of 0.5-3Hz affecting the characterization of K-complexes observed during stage N2 of NREM sleep and deep or slow-wave sleep (stage N3 of NREM).

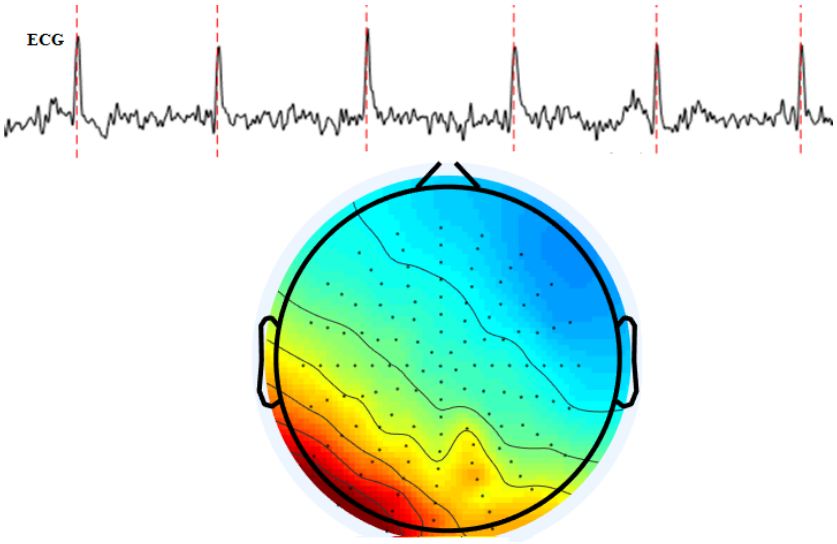

Figure 3-4: ECG physiological artifacts in the ICs space and the scalp potential distribution of the QRS peak. Note the superimposed high-amplitude area in the left-occipital region.

The muscle artifacts from face, neck, and jaw generate an electrical activity called electromyography (EMG) that has high impact on EEG quality [64]. When jaw muscles are activated (teeth clenching and chewing) or if the head moves that involve neck muscle contractions, high amplitudes (in the order of mV) can be observed on the EEG measurements in the 20-30 Hz frequency range. Because head muscle activations are an inherent part of normal daily routines, solutions are needed that handle such artifacts. ICA might be considered an appropriate method to remove EMG contamination since both EMG contamination and EEG have substantial statistical independence from each other both temporally and spatially [65,66].

Changes in the quality of the electrical contact of channels over the skin produce the largest disturbance in the EEG. These kinds of artifacts are called motion artifacts, which influence the contact surface size, introduce skin deformation, and cause changes to the interface layer due to changes in conductive gel thickness or amount of sweat, resulting in electrical impedance change in turn. Artifacts of movement produced during normal activity, including locomotion, may have amplitudes greater than the signals produced by brain activity.

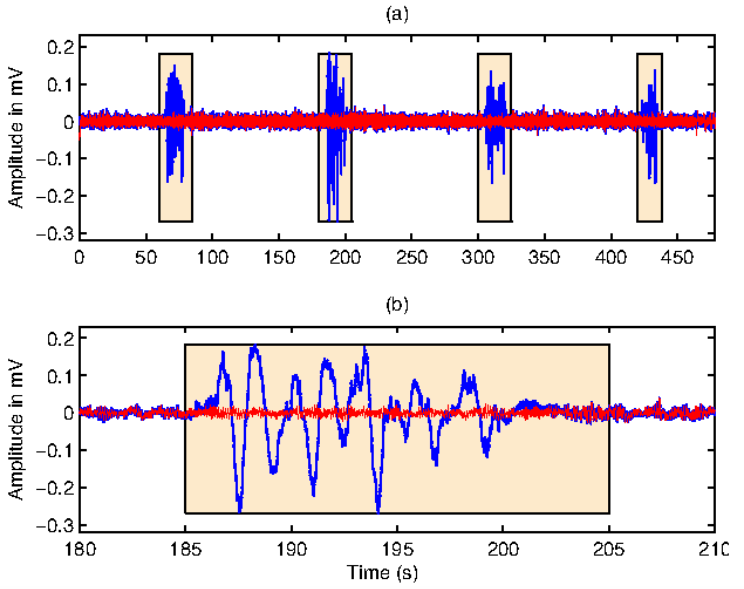

Figure 3-5: (a) Superposition of the true EEG signal (red) and the contaminating artifacts (blue). (b) Zoomed in view of the second contaminated signal section [67].

Unlike the artifacts mentioned above, which usually show stereotypical behaviour, movement or motion artifacts are non-stationary electrical signals. This makes cleaning of such artifacts one of EEG's major challenges. While the automated reduction of the artifacts has made substantial progress, there are only a few approaches that provide fully automatic artifacts handling methods for physiological artifacts [68].

3.2 Artifact Removal Methods

Artifact removal is a process of recognizing artifact components in the EEG signal and separating them from the neuronal sources. These strategies may use only EEG signals during artifacts rejection but may also rely on information from sources capturing physiological signals such as EOG, ECG, EMG. Most artifact rejection methods assume that the recorded signal is a combination of the signal of interest and the artifact signal, and the combination is additive in nature. Based on this fact, methods that are applied for artifact removal include regression, blind source separation (BSS : ICA and PCA), empirical mode decomposition (EMD), and wavelet transforms (WT) and in some cases, a combination of these methods is used [69,70].

A review of the most common EEG artefacts removal methods [71] provides a chart about percentage of the number of papers in the literature over the past five years (2015-2019), shown in Figure *3-6*. It shows that Independent Component Analysis is the most frequently used method, moreover it was introduced with regression, WT, etc. as known as hybrid method to enhance the performance. Although there was an extensive research centred on artifact detection and removal of EEG signals reported in many literatures to date, there is no consensus on an optimal solution for all forms of artifacts, and the topic is still an open research problem [71].

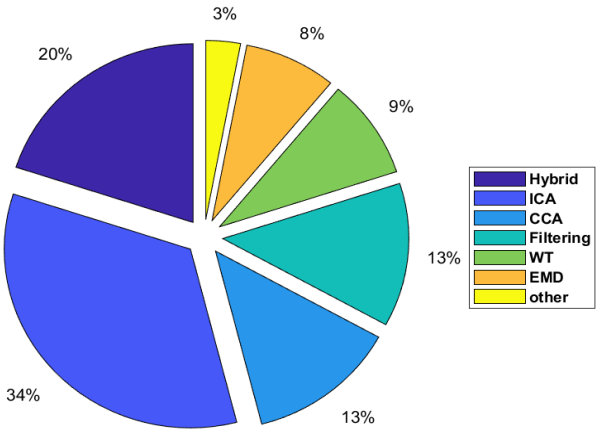

Figure 3-6: Percentage of the number of literatures published during the past five years [71].

Visual inspection is one of the traditional methods used to remove artifacts; artifact contaminated or bad channel data segments (epochs) are simply rejected. This approach is laborious and can potentially lose useful neural information. Epoch rejection can largely reduce the number of usable epochs and reduce the signal-to-noise ratio. Manual inspection prevents the automatic and high-speed analysis of large-scale EEG experiments. The ICA-based source separation methods [72] could help in bad channel detection too, since bad channels show up as easily identifiable components as illustrated in Figure *3-7*.

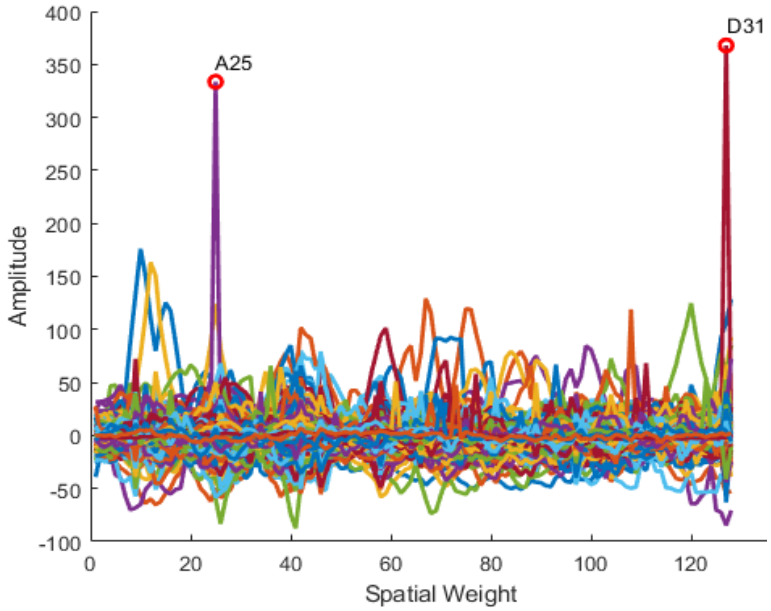

Figure 3-7: Bad channels (A25, D31) detected in the independent component space.

Spatial correlation with the other channels can be used to identify the bad channels [16,73,74] but if correlation is low, these algorithms cannot identify the bad channel correctly. The correlation is mainly dependent on the distance between the electrodes: two distant electrodes might show low correlation although they might be phase-correlated. Automatic selection criteria based on statistical features are used in the FASTER [15] and EEGLAB [75]packages using pre-defined threshold such as z-score [15,18], which is still not robust since not all bad channel features can be described by the implemented features.

The DETECT package [50] is a MATLAB toolbox for detecting irregular event time intervals by training a model on multiple classes. The method showed results close to what they manually

identified, but is still dependent on the supervised learning method. An automatic bad intracranial EEG (iEEG) recordings was introduced by Viat et al, [74], using machine learning algorithm of seven signal features. The machine learning algorithm is supervised learning dependent and needs a large number of datasets and a variety of conditions for the training session. Correlation, variance, gradient, etc., were used as marker features identifying the deviation between the channels, however the method is dependent on supplying seven features to the trained network. This implies that the data has to be pre-recorded to extract the features from the raw data, and consequently lose the real-time processing.

More sophisticated artifact removal methods rely on cross-correlation based filtering that require the use of so-called reference channels that record horizontal, vertical eye movements (EOG) and ECG activity. The use of reference electrodes can be acceptable in strictly controlled laboratory situations, but they can be problematic in clinical settings due to patient discomfort or movement.

3.2.1 Independent Component Analysis

Independent Component Analysis (ICA) [72] was originally developed for solving the Blind Source Separation (BSS) problem, which is considered a robust method for artifact removal able to minimize the mutual information between the different sources. ICA decomposes the EEG signals into independent components assuming that the sources are instantaneous linear mixtures of cerebral and artifactual sources. The two main approaches for measuring the independent sources are: minimization of mutual information and maximization of non-Gaussianity. The mutual information approach, informs how much information about the variable **X** could be gained from the information about the variable **Y.** The smaller value of mutual information means that more information about a given system is stored in the variables [76], so ICA algorithms based on mutual information approach are used to minimize the mutual information of the system outputs [19]. In the maximization approach, the algorithm has to modify the components in such a way to obtain the source signals of high non-Gaussian distribution (using the fact that: the stronger the non-Gaussian, the stronger the independence [76]). Different kind of metrics are used for maximization calculation as kurtosis, entropy, negentropy, approximations of negentropy and others [72].

Since ICA has unsupervised learning characteristics and works without a priori information and extra reference channels, it is used widely in the field of EEG noise (such as ECG and EOG artifacts) [11,21,70,77,78] removal. After source separation, estimated sources have to be identified as neuronal or artifactual sources to reconstruct the artifact-free EEG matrix where the unwanted artifacts (components) can be rejected by visual or automatic inspections.

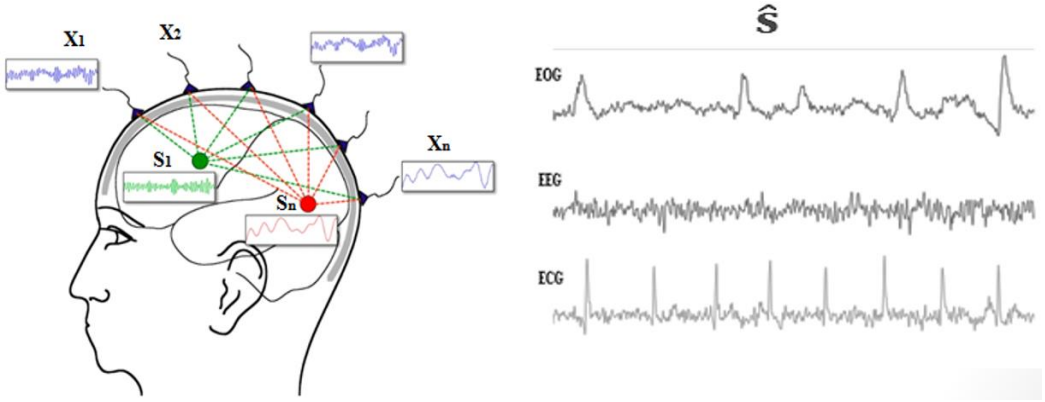

Figure 3-8: Independent component analysis.

The recorded signal can be described as a linear combination of independent sources (components) and mixing information as shown in the following equation:

$$x_t = As_t \quad (3.1)$$

where x_t is the vector of observed signals, s_t is the vector of original source signals, and A is the mixing matrix (square spatial weight matrix, channel×components). The original unmixed sources can be recovered using the following equation:

$$\hat{s}_t = Wx_t \quad (3.2)$$

and $W = A^{-1}$ is the "unmixing matrix" which must be obtained in order to calculate the estimate $\hat{s}_t$ of the original sources.

ICA algorithm was applied for the first time to analyse EEG and EPR signals by Makeig et al. [47]. Unlike traditional approaches to cancelling artifacts, Vigaro et al. tested the ICA method on simulated and experimental data and demonstrated good performance in separating signals from their linear mixtures and extracting the eye information present in EOG signals [48].

In 2000, Jung et al. extended the ICA approach and effectively improved the results by combining it with regression algorithm to remove artifacts from EEG [79]. In different sleep stages, Romero et al. applied ICA to reduce EOG artifacts, and a bidirectional property of EEG and EOG was found, which had little effect on ICA [80]. Probability approach, pre-defined threshold, and machine learning algorithms with extracted features from the estimated components have been used for automatically identifying artifacts to save efforts and time [16]. Delorme devised a semi-automatic method using probability and kurtosis as feature extraction from the estimated components to eliminate the artifacts [14].

A state-of-the-art published review in 2015 reported that the information maximization (Infomax) and second order blind interference (SOBI) algorithms are the most popular algorithms used for EEG signal processing [81]. ICA was used with multivariate empirical mode decomposition (MEMD) to remove the EOG and keep the EEG information. However, much EEG information was lost using this method and the results showed range of values of Root Mean Square Error (RMSE) around 18 µV to 22 µV between the corrected and original signals. Hence, using the traditional method based on rejection the artifactual component, makes the reconstructed signal different from the original data and might cause distortion in the signal spectrum that can lead to an overestimation of the coherence between different cortical sites [70,82].

Automatic and unsupervised component identification algorithm has still been an active research area to characterize more precisely and flexibly [83–86]. Automation not only saves time, but also allows scalable analysis and reduces the barriers to reanalysis of data, thus facilitating reproducibility and help for real time data processing [87]. Joyce et al. developed a fully automatic method applied to the estimated ICs to remove eye artifacts and avoid the errors introduced by manually selected components [88]. It has been reported that wavelet-transform based ICA is a superb method for artifact rejection [89], therefore, a number of researchers focused on them in recent years. ICA merged with WT for artifacts rejection increased in many application [11,12] either applied the ICA to the decomposed WT signal (AWICA) [69] or applying the WT to the artifacts IC components (wICA) [70] and finally inverse the calculation to reconstruct the cleaned signal. Kurtosis and Renyi's entropy were introduced as markers to measure the artifactuality on the AWICA method as previously proposed in [90]. However, in higher dimensions Renyi's entropy requires time-consuming calculations due to the kernel density needed for the component [91].

Enhanced Empirical Mode Decomposition (EEMD) was combined with ICA by Wilson et al. for the first time in 2006 to remove EMG and ocular artifact from EEG [79]. The proposed algorithm was compared with single-channel ICA and WT-ICA on real EEG signals and showed that the EEMD-ICA algorithm has the best performance.

ICA and Support Vector Machine (SVM) were combined to remove the identified components where the temporal, spatial and statistical features are extracted from the estimated components and passed as input to a set of linear SVM classifier. Once the classifier identifies the artifact components, the remaining components are used to reconstruct the artifact-free data [81]. Shoker et al. used this algorithm to remove eye-blinking [92], while Halder used it to remove the EMG artifacts from EEG [93].

3.2.2 Regression Method

The most commonly used method in artifacts removal was the regression algorithm until the mid-1990s [94]. An observed EEG signal $\boldsymbol{X(n)}$ and the artifacts $\boldsymbol{X_{art}}$ should be supplied to this method. The artifact would be corrected by estimating propagation factors to calculate the relationship between the observed EEG signal and the reference signal $\boldsymbol{X_{ref}(n)}$ and subtracting the regressed portion. Thus, this algorithm needs exogenous reference channels (i.e., ECG, VEOG-HEOG) to cancel different artifacts.

Hillyard et al. [95] proposed regression method in the time-domain to remove the ocular activity. Whitton [95] modified this method in the frequency domain and combined it with other EEG detection methods. Since the ocular potential contaminates EEG data, EEG data can also contaminate ocular recording, so in time-frequency domain bidirectional methods affect such regression approaches [96]. Consequently, Wallstrom applied filtering method prior to calculating the adaptive regression splines [97] thus, the bidirectional contamination issue was substantially reduced. Despite the simplified model and the reduction of computational demands of the regression methods, the need for one or more strong regression reference channels limits their ability to eliminate EOG and ECG artifacts [81].

If eye movement is recorded with special electrodes, this reference EOG signal can be used in ICA in combination with regression methods to automatically identify and remove the EOG artifacts from the contaminated signal, and as a result, increase the signal-to-noise ratio (SNR) [98,99]. A similar protocol introduced ICA with the Auto-Regressive exogenous (ICA-ARX) [100] to remove the ocular artifacts using EOG reference signal.

3.2.3 Wavelet Transform (WT)

Wavelet transformation [101] has emerged as one of the best techniques to analyse non-stationary signals such as EEG. Its ability to transform a time-domain signal into time and location of frequencies helps to better understand a signal's behaviour. Also, it was used to remove the EOG and other kind of artifacts from EEG in many applications [70,90,102]. It performs low-high pass filtering to generate low-high frequency components. Once the signal is decomposed, a threshold is applied to discard the signal that contains artifacts and the remaining details are used to reconstruct the clean signal [43]. Amorim et al. applied the Discrete Wavelet Transform (DWT) in the raw data space to remove the EEG artifacts by decomposing the measured signal using one of the basis functions of the wavelet families such as Symlets, Coifs, Haar etc.,[103]. Others combined it with the statistical approach, to extract the artifacts features from the decomposed EEG raw signal using Symlets as basis functions [104,105] giving an absolute average error of 14 to 24 dB between the cleaned and the noise free signal.

In spite of its versatility for artifact attenuation, the DWT does not fully identify artifacts with overlapping spectral properties, so recent work prefers to combine DWT with other methods, such as ICA [70,90]. In many applications, DWT was merged with ICA for artifacts rejection [11,12] either applied the ICA to the decomposed DWT signal AWICA [69] or applying the DWT to the artifacts IC components as in the wICA method [70] and finally inverse the calculation to reconstruct the cleaned signal. Other approach was proposed by Kelly et al. [91] where the artifactual coefficients above a threshold were replaced by the median of a set of coefficients outside the artifacts.

An adaptive threshold based on DWT was used to identify and remove the EOG [106] without losing the related EEG information. This approach was slightly modified by Nguyen et al., [107] who introduced Wavelet Neural Network (WNN) (clean and contaminated EEG data is used to train the network) and achieved 9.07 μV Root Mean Square Error (RMSE) between the cleaned and the noise free data. Their method works without a reference EOG signal that is normally required in the linear regression based methods [98].

3.3 Literature Review of EOG Artifacts Removal

Removing EOG artifacts from the EEG signal by manual inspection and rejection is not a recommended approach since removing contaminated trials by setting a rejection amplitude threshold [108] may remove too many trials and lead to losing important EEG-related information. Since the EOG spectrum overlaps with that of the underlying EEG signals, normal filtering methods are unable to entirely remove their effects [109].

Avoiding artifacts, i.e., reducing the occurrence of these artifacts by asking subjects to refrain from or minimize blinks and eye movements might be an alternative, but it introduces unnecessary stress on the subjects that results in undesirable activities that affect Event Related Potential (ERP) components [110]. Moreover, this method cannot be used with children and clinical patients where movement control might be problematic. Another removal approach is based on the use of reference EOG channels [98] to record eye movements which information then can be used to subtract artifacts from the recorded EEG using adaptive filtering based on autoregressive models. These methods however do not take into consideration that the reference EOG channels are also contaminated by EEG data which introduces problems in obtaining an accurate estimate of EOG effect [108].

Joyce et al. [111] proposed the use of ICA for automatic EOG artifact removal. Their approach was based on rejecting those sources (components) that correlated highly with the reference EOG channel. Zeng et al. [112] claimed that using a stationary subspace analysis (SSA) algorithm to the BSS problem concentrates artifacts in fewer number of components than BSS and it requires neither the independence nor the uncorrelation ICA restrictions among the sources. This method, however, results in loss of EEG information as reported in [113]. While ICA-based methods show encouraging results in EOG artifacts removal, it has been shown that ocular sources are not entirely separated from neural sources [111], which makes the full rejection method a non-preferred solution. Consequently, ICA should be integrated with more sophisticated methods to achieve more accurate artifact removal.

FASTER [15] and DETECT [50] are automatic MATLAB-based processing pipelines for complex artifact removal. They include an EOG removal step that relies on statistical properties and EOG reference channel data. The ADJUST [16] tool uses a similar approach by extracting

statistical features such as kurtosis, average variance, etc. to automatically remove the EOG artifacts with reported 95% accuracy [114].

Burger and van den Heever [78] improved on this method, however, their solution can only remove eye blinks, and it does not work for eye movements. In another application, a combination of ICA and DWT (wICA) [70] was used, based on the fact that wavelet coefficients of the artifact component typically have higher amplitudes than that of the cerebral activity components, so by setting the coefficients greater than a certain threshold to zero value, EOG artifacts can be removed from the signal.

3.4 Literature Review of ECG Artifacts Removal

Early ECG removal attempts included subtraction and ensemble average subtraction (EAS) [4] methods. Current mainstream methods are based on adaptive filtering [5,6] blind source separation (such as ICA) [7,8] or wavelet decomposition [9,10] methods, although wavelets are increasingly more often used in combination with ICA-based methods [11,12]. The works of Dora and Biswal [9] and Jiang et al. [10] use wavelet decomposition-based ECG detection methods. In both cases, the Continuous Wavelet Transform is used to detect QRS waves in the EEG signal. In the first case, a reference ECG channel and linear regression are used to remove the detected QRS waves. Reported sensitivity varies between 91 and 100% depending on the input dataset, providing lower values in more difficult cases, such as sinus arrhythmia. In the second case, no reference channel is used; the detected artifact signal (wavelet coefficients) is subtracted from the original signal to obtain the clean one. Although the reported detection performance of this method is above 97.5%, the method ignores the removal of the P and T waves that may also contaminate EEG data.

Hamaneh et al. [11] use an automatic ICA-based approach. A reference spatial distribution template of the ECG artifact [77] and a Continuous Wavelet Transform-based periodicity test are used in combination to identify ECG independent components. If a component shows correlation with the spatial template (threshold > 0.6) and passes the wavelet periodicity test, it is marked for removal. The spatial ECG template was used as reference ECG signal. While the method provides good true detection rate (95-99% depending on the ECG contamination rate), the required spatial ECG component template has to be created by averaging manually selected ECG components of several subjects, which reduces the level of possible automation.

Mak et al. [12] propose an automatic ECG removal method for EMG (Electromyography) signal cleaning. Similarly to others, the wavelet transform is used to detect R peaks, after which a set of decision rules are applied to the candidate component (checking heart rate, RR interval, variance of RR interval) to detect the ECG component. Although the method is developed for cleaning trunk muscle signals instead of EEG, the reported excellent ECG detection sensitivity (100%) makes it worth mentioning. Unfortunately, there are no testing results for detecting pathological ECG artifacts.

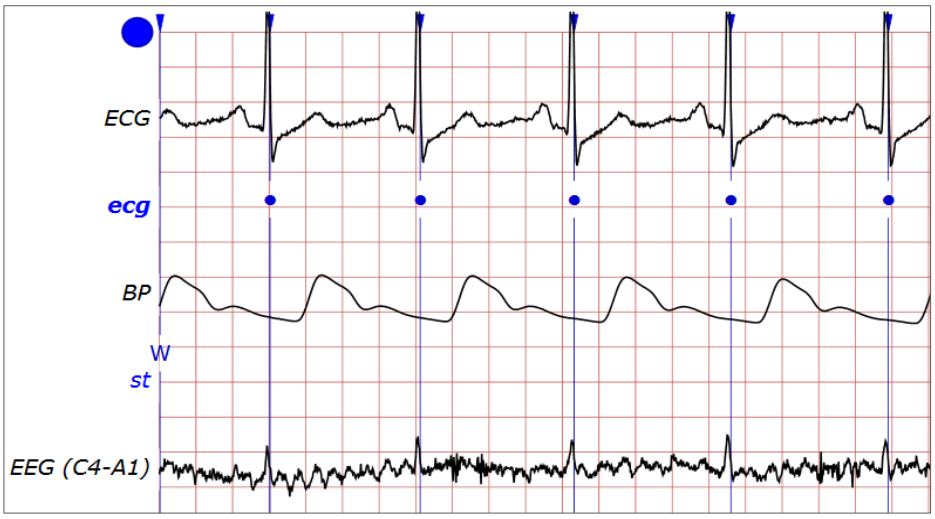

Figure 3-9: Annotated measurement from the MIT-BIH Polysomnographic database showing ECG, Blood Pressure and EEG signals. Note the pronounced ECG artifact contamination on the EEG channel (data record: https://physionet.org – slpdb/slp32).

4 Removal of EOG Artifacts

This chapter focuses on the automatic removal of ocular artifacts. Eye movements and blinks are transient activities occurring relatively infrequently but unfortunately, they generate very high amplitude peaks. These might be located visually by checking the corresponding component. The usual approach is to reject an independent component entirely if it contains EOG artifacts. This, however, may lead to loosing important EEG data present in the component [78,100,111]. Building on the Wavelet-enhanced ICA method proposed by Castellanos and Makarov [70], I developed a method to selectively remove EOG artifacts from ICA components instead of rejecting the entire component. This will keep most of the relevant EEG information in the component. The proposed method does not require visual inspection and manual intervention, which can significantly speed up pre-processing steps and can lay the foundation for online and potentially real-time EEG analysis.

4.1 Subject and Motivation

EOG artifacts are random, high-amplitude distortions in EEG recordings that, if appear frequently, can make entire measurements unusable. Due to the unpredictable nature of artifacts, traditional artifact removal is based on manually data inspection and rejection of contaminated data segments. This process is both time-consuming and prone to human errors. The introduction of Independent Component Analysis for artifact removal [115] revolutionized the field, first by providing a theoretical framework for separating artifacts, then secondly, by paving the way to automatic, intervention-free implementations. Unfortunately, the strong statistical independence assumption of ICA does not always hold in practice, resulting in neural data leaking into artifact components. In these cases, independent component rejection-based artifact removal methods lose valuable neural activity information.

The literature reviews gave different solutions for EOG artifacts removal. Some of them used a reference channel for the processing which make this protocol impossible without the EOG reference channel, others used a statistical threshold which removed a lot of EEG information, and other rejected the ICAs-EOG related component which removed EEG related information in the rejected component. The aim of my proposed ICA-based artifact removal method is to clean the EEG from the EOG artifacts without reference information and to keep as much neural information of the original signal as possible during removal.

4.2 Method Details

The main steps of my method is described first in algorithmic form, also illustrated as a flowchart in Figure *4-1*, then a detailed description of each step follows. The algorithm form of the proposed method is shown in the following steps:

1. Each measured dataset (recorded signals in 128 channels) is bandpass filtered (1-47Hz, zero phase 4^{th} order Butterworth), then re-referenced to the average reference.
2. Infomax ICA is applied to the dataset to estimate the source components.
3. Automatic identification of the EOG component (EOG source in the EEG signal): the EOG component is identified based on the correlation between each component and data of each frontal EEG channel. The component with the highest correlation and above a threshold weight is selected as an EOG component.

4. The identified EOG components are searched for EOG peaks.
5. One-second windows are placed around the detected EOG peaks.
    a. If the windows cover more than 60 percent of the given component (Greater than 60 percent means the component worth to be rejected, this usually did not occur since EOG are just few peaks in the identified component), the entire component is marked for rejection. Continue at Step 7.
    b. Otherwise, the windowed areas of the component are the target of the artifact removal.
6. Wavelet decomposition using Symlet *sym4* [10,103,105] wavelets of 5 levels is applied to decompose signals in each target window to different wavelet components, and only the high frequency components are retained for the signal reconstruction process (low frequency of the EOG peaks are rejected, while the other peaks in the EOG component are left untouched). These retained components are used in the inverse wavelet transform to reconstruct the cleaned independent component.
7. Using the inverse ICA process, the artifact free signals are estimated from the corrected components.

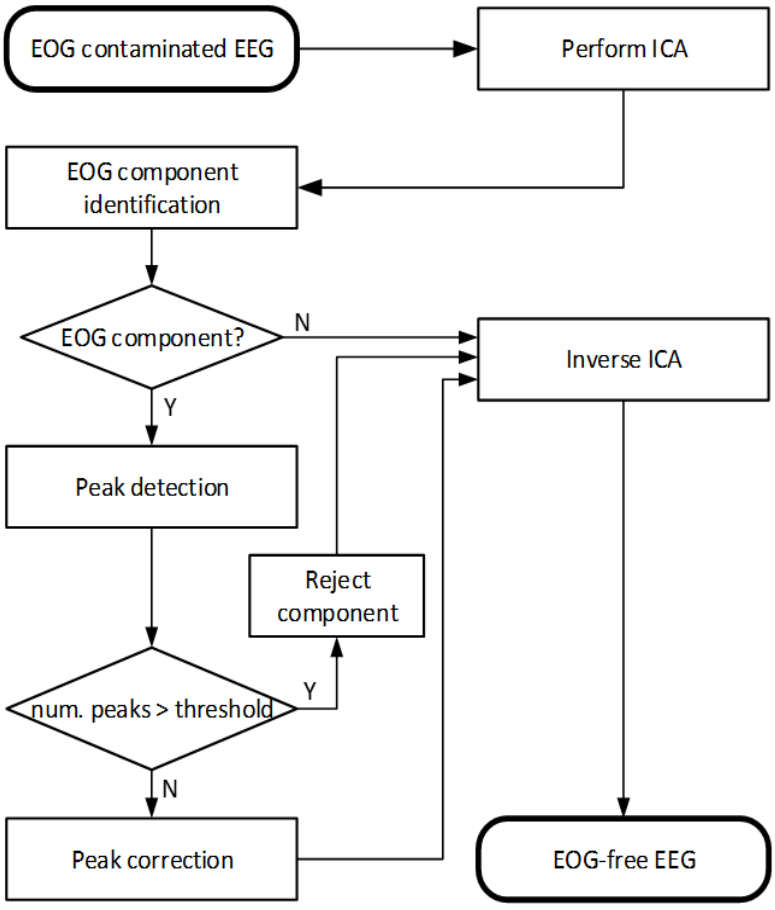

Figure 4-1: The data processing flowchart of the proposed EOG removal method.

EEG frequency of interest is located in this band (Delta 1:4, Theta 4:8, Alpha:8:12, Beta:12:30, Gamma:30:45)[116]. This band avoids the appearance of the power line noise 50 and 60 Hz. Also, it is known that alpha frequency activity decreases in stroke patients, while low frequency, especially delta band, increases, so this was selected for the connectivity calculation.

Once the input signal is filtered and the ICA process is executed, the first step is to identify which component shows signs of EOG artifacts. This is carried out by computing the Pearson correlation $R_{X,Y}$ between a given independent component Y and each of the frontal channels X (shown in Figure *4-2*). The underlying assumption is that EOG artifacts appear primarily in the frontal channels and the component describing EOG activity should have high correlation with some of these channels. Pearson correlation is computed by the following formula:

$$R_{X,Y} = \frac{Cov(X,Y)}{\sigma_X \sigma_Y} \qquad (4.1)$$

where $\sigma_X$and σ_Y are the standard deviations of channel *X* and component *Y*, respectively. Components with the highest *R* value are identified as candidate EOG components to be examined further. Naturally, a different set of frontal electrodes must be selected for different electrode layouts. The number of frontal channels does not affect the accuracy of the proposed method as long as there are at least two frontal channels on the forehead, one close to the left and one to the right eye. This ensures that high correlation between ocular artifacts and EOG components can be found.

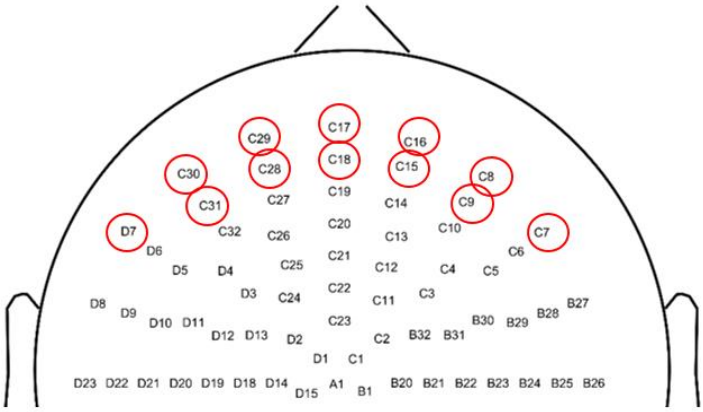

Figure 4-2: Frontal channels (marked by red circles) used for correlation calculation in EOG independent component identification. Top view of scalp with nose pointing upwards, 128-channel Biosemi ABC electrode layout.

The candidate components are further examined for weight value distribution and only those with weights greater than a threshold are kept as EOG components. Elements of the weight vector **w** are defined as:

$$\overline{w}_j = \frac{1}{K}\sum_{i=1}^{K} |w_{ij}|, \quad j = 1,2,\dots,N, \qquad (4.2)$$

where $\overline{w}_j$ is the average weight of component *j* over the frontal channels, w_{ij} is the weight element of the mixing matrix **A**, *K* is the number of the frontal channels and *N* is the number of components. The distribution of values in the weight vectors are used to calculate a statistical threshold. The distributions are shown for all three datasets in Figure *4-3*, Figure *4-4* and Figure *4-5* as boxplots. Red crosses represent weights for the EOG components. Note that the maximum value of each distribution acts as a reliable threshold for detecting the EOG component (outliers).

4.2.1 EEG Datasets

Three different EEG datasets have been selected for the evaluation of the proposed method. These include publicly available datasets, as well as data recorded in our laboratory.

Semi-simulated dataset: The publicly available Klados EEG dataset [117] was created for the purpose of EOG artifact removal validations; to serve as a reference dataset that can be used for comparison purposes. Data were recorded from 27 subjects (males and females), using the standard 19 electrode 10-20 layout EEG system, with sampling frequency of 200 Hz, resulting in 54 datasets. Simulated EOG artifacts were then added to the pure, artifact-free data using the following expression:

$$\text{Contaminated\_EEG}_{i,j} = \text{Pure\_EEG}_{i,j} + \text{a}_j V_{EOG} + \text{b}_j H_{EOG}\,, \qquad (4.3)$$

where $\text{Pure\_EEG}_{i,j}$ is the signal obtained with eyes closed (no EOG artifacts), and the V_{EOG} and H_{EOG} terms are the additive vertical and horizontal EOG activities.

PhysioNet EEG datasets: The PhysioNet database contains Brain-Computer Interface datasets [62,63] that were recorded during BCI experiments to measure the event-related potential (ERP) of the P300 waves in a spelling experiment. Data were collected using the BioSemi Active Two EEG system, with 64 EEG electrodes and additional VEOG, HEOG ocular electrodes at 2048 Hz sampling rate.

Laboratory resting-state dataset: I have recorded 2-3 minute closed and open-eye resting state EEG in our laboratory from 22 adult volunteers (males, age from 16 to 21 years). During the experiment, subjects had to sit and relax in a silent room. Data were recorded using a Biosemi ActiveTwo EEG system (f_s = 2048 Hz) using 128 active electrodes arranged in the ABC radial electrode layout. The volunteers gave their written consent for participating in the experiments. The entire klados' datasets were tested and Figure 4-3, only shows 20 datasets to fit with the figure width.

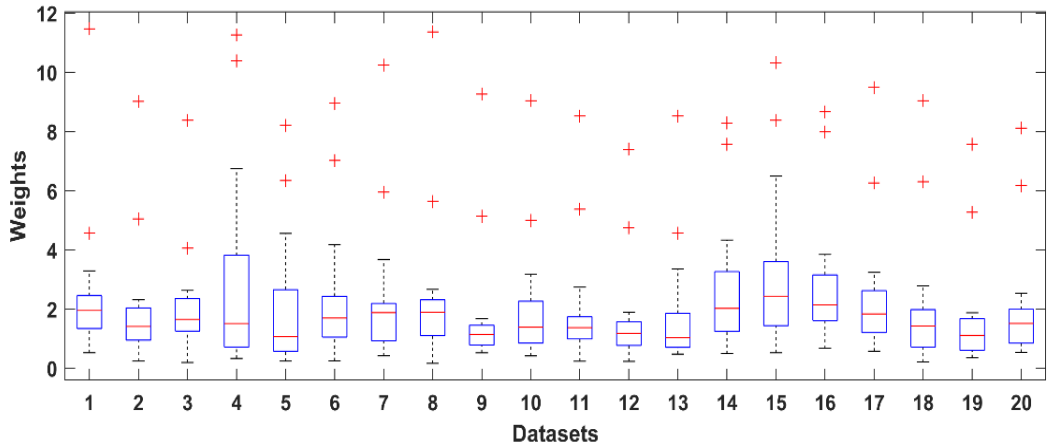

Figure 4-3: Distribution of the normalized weights of the components of 20 EOG contaminated measurements (datasets) selected from the Klados datasets. The red crosses represent the weight of the EOG (Horizontal EOG, Vertical EOG) components.

Two EOG components are located in each record in Klados datasets related to the VEOG and HEOG, where these components are artificially added to each dataset for creating semi-simulated datasets to be used by artifacts removal algorithms, however, in the normal EEG measurements, usually there is one strong EOG component appears in the datasets as shown in the following figures.

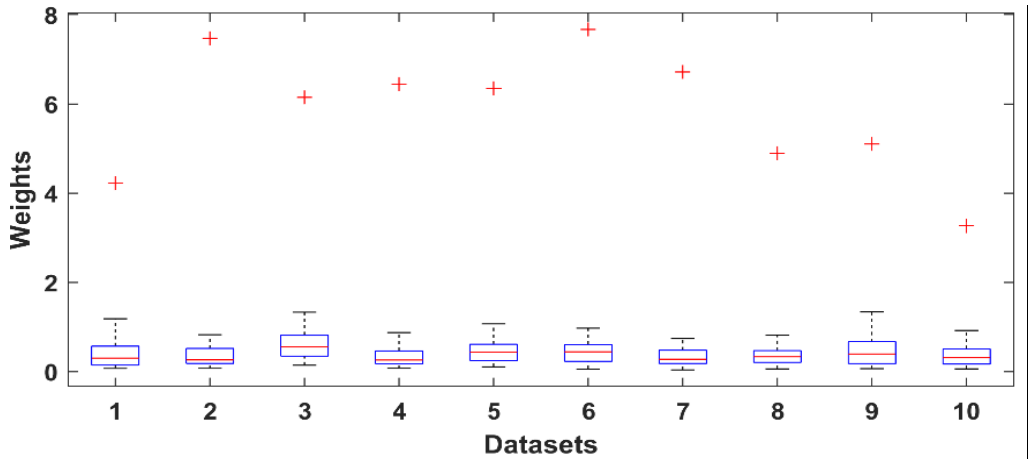

Figure 4-4: Distribution of the normalized ICA component weights of 10 selected PhysioNet datasets.

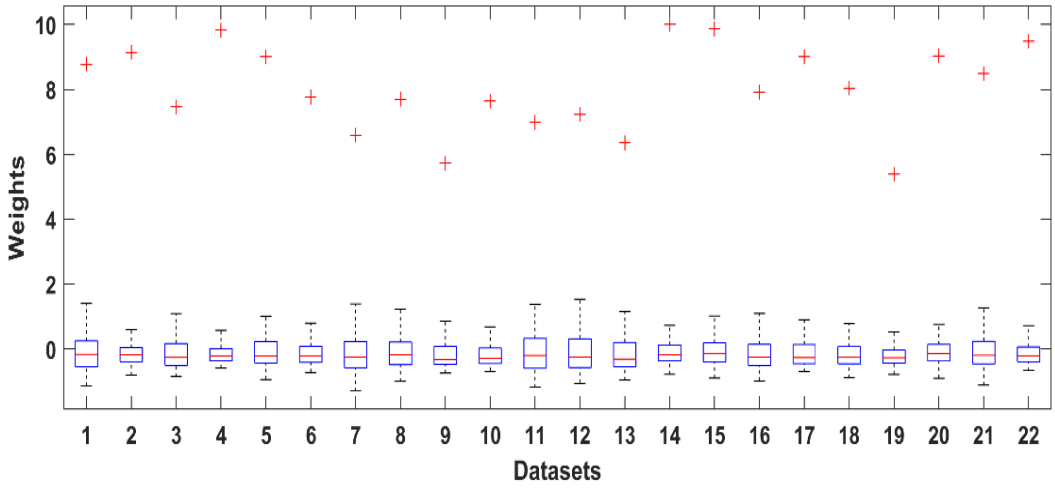

Figure 4-5: Distribution of the normalized ICA component weights of the 22 datasets obtained in our laboratory.

The threshold is computed from the distribution of weights and each weight vector element is tested against it to decide whether the component is, in fact, an EOG component:

$$\mathrm{Y_i\ is\ EOG, if}\ \bar{w}_i > Q_3(\mathbf{w}) + 1.5 * IQR(\mathbf{w}), \qquad i = 1..N, \tag{4.4}$$

where $\bar{w}_i$ is the weight of component Y_i, $\mathbf{w}$ is the averaged weight vector, and Q_3, IQR are the upper quartile and interquartile range, respectively [118]. The result of this step is illustrated in Figure *4-6* and Figure *4-7*. Figure *4-6* shows the independent components of a selected dataset. Components 1 and 2 contain EOG artifacts (blinks and eye movements, respectively). Figure *4-7* shows the result of the component selection and threshold application that identified the EOG components for the sample datasets 1-4.

The next step in the algorithm (Step 4) is the detection of EOG peaks within the components. First a normal peak detection is performed on the component values (finding local maxima [119]), then the peaks are further examined whether they are, in fact, EOG peaks. The decision whether a local maximum m_k belongs to the set of EOG peaks P is made using the following rule containing amplitude and duration constraints.

$$P = \{m_k \mid |Y_i(m_k)| > 3 \cdot E\{|Y_i|\} \text{ and } t(Y_i(m_k)) - t(Y_i(m_{k-1})) \geq 0.5\text{sec}\} \qquad (4.5)$$

where m_k is k^{th} peak in component Y_i and $E\{|Y_i|\}$ is the expected value of the component vector Y_i, and t refers to the timestamp of peak m_k. Each two consecutive selected peaks must satisfy the peak amplitude condition and the between-peak time distance of 0.5 second to correctly classify peaks as EOG artifacts.

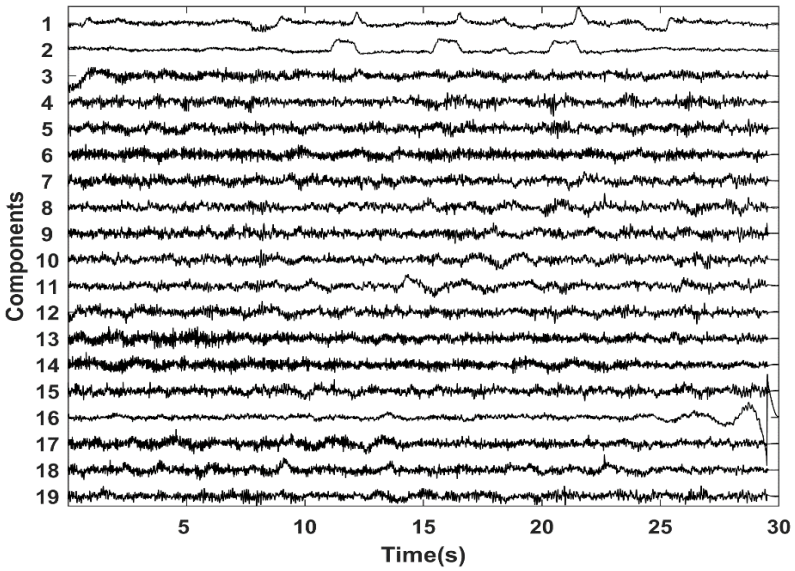

Figure 4-6: ICA components (Decomposed original sources of the recorded EEG signal) of a selected Klados dataset.

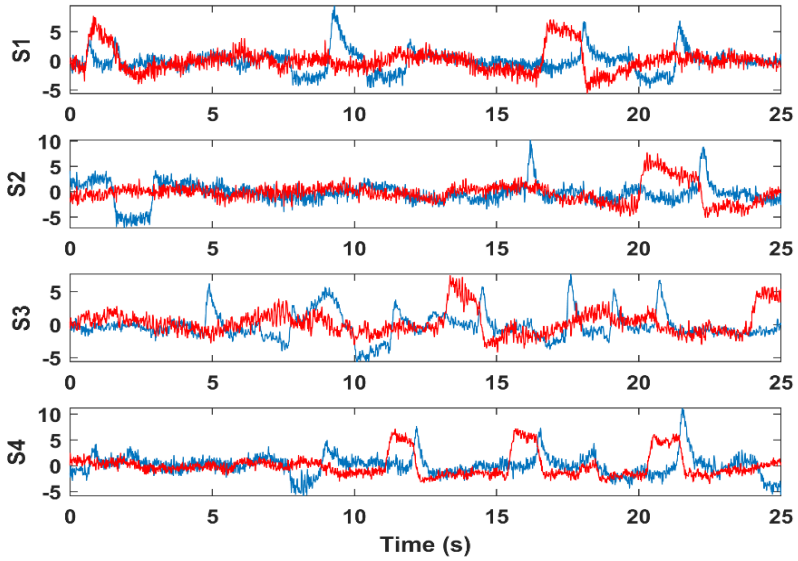

Figure 4-7: Sample sections of VEOG (blue) and HEOG (red) EOG components from four selected Klados datasets, Y axis is the weight of the calculated components, which has to be adjusted to transform it to normal potential values in micro volts.

After locating the EOG peaks, target windows are placed around the peaks for EOG artifact removal (Algorithm: Step 5). A window size of 1 second duration is used, as this spans the length of the EOG artifact waveforms [120,121]). These windows will equally designate vertical-EOG

(VEOG) and horizontal-EOG (HEOG) sections. Figure *4-8* illustrates the results of this step showing the windows marking blink and eye movement EOGs, respectively.

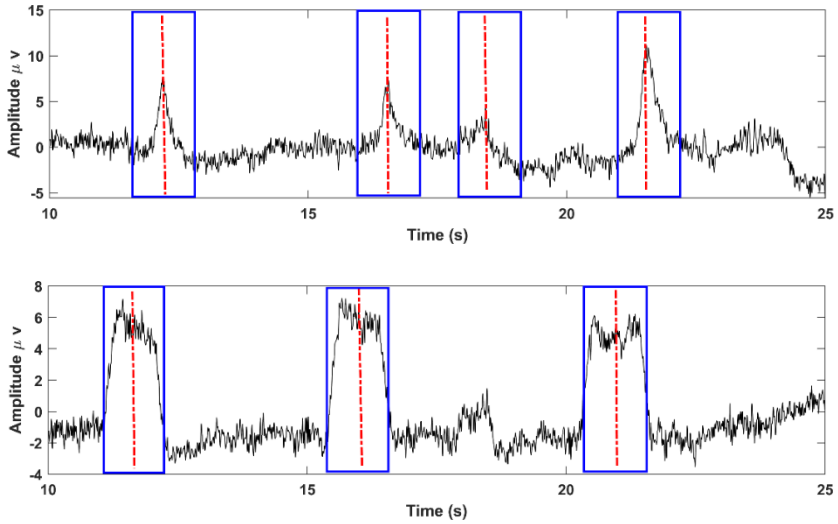

Figure 4-8: Correction target windows around the detected VEOG blink (top) and HEOG eye movement (bottom) peaks in the EOG ICA components.

Artifact removal is performed on the EOG components selectively, only within the target windows, using wavelet decomposition (Algorithm: Step 6). The discrete wavelet transform (DWT) of a signal *f(t)* is defined as

$$\mathrm{F}_W(\mathrm{j},\mathrm{k}) = \frac{1}{\sqrt{2^j}} \sum_{t=0}^{N} f(t)\, \varphi\left(\frac{t-k2^j}{2^j}\right) \qquad (4.6)$$

where φ is the wavelet basis function, j is the scale parameter and k is the shift parameter. The success of EOG detection in a component is dependent on the choice of wavelet basis function [103] and the level of decomposition [122]. Several wavelet basis functions, e.g. Haar, Daubechies, Coiflet, Symlet, can be used to detect and correct EOG waveforms [104,105,123]. It has been shown [123] that the *Symlet* wavelet family (*sym2* to *sym20*) is the most suitable for EOG peaks and has been used successfully in several artifact removal applications. The *sym-4* wavelet was selected as final basis function due to its smallest error (RMSE) between the corrected and artifact-free signals [123]. My tests with the Symlet wavelets confirmed the same results (mean RMSE -- Haar: 9.85, db4: 7.42, sym3: 7.37, sym4: 6.29, sym5: 6.54, sym6: 6.96).

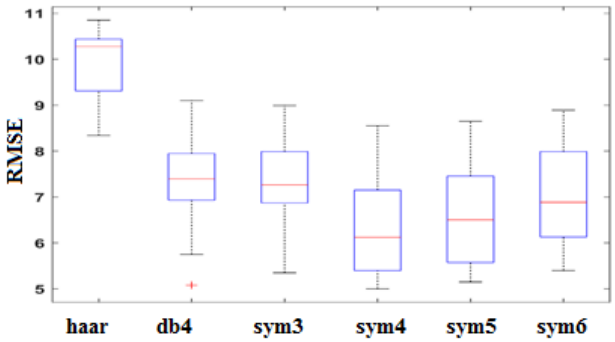

Figure 4-9: Avg. RMSE for different used wavelet functions.

The ICA component signal is decomposed into wavelet components by passing through a quadrature mirror filter performing low-pass and high-pass filtering followed by down-sampling

the input signal at each level of decomposition and generating the output coefficients related to lower and higher frequencies [124]. The details of this process is shown in Figure *4-10*.

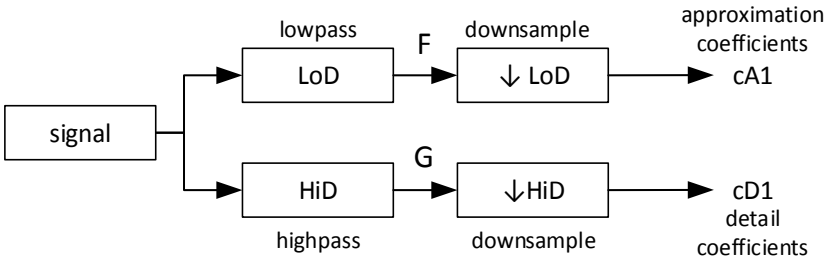

Figure 4-10: The wavelet decomposition process and calculation of coefficients.

In order to find the optimal parameters, different levels of wavelet decomposition were tested. Five levels of DWT were used to decompose the component into detail (D1:D5) and approximation coefficients (A), as illustrated in Figure *4-11*. Coefficients D1:D3 represent the higher frequency components while coefficients D4:D5 while A represent low frequency components. Since the spectrum of the EOG artifacts is concentrated in the frequencies below 7 Hz [125], the signals were reconstructed only from coefficients D1:D3, which represent the high frequencies related to the EEG signal; the other components were discarded. The reconstructed signals are then projected back to the EOG components and inverted to obtain the artifact free data.

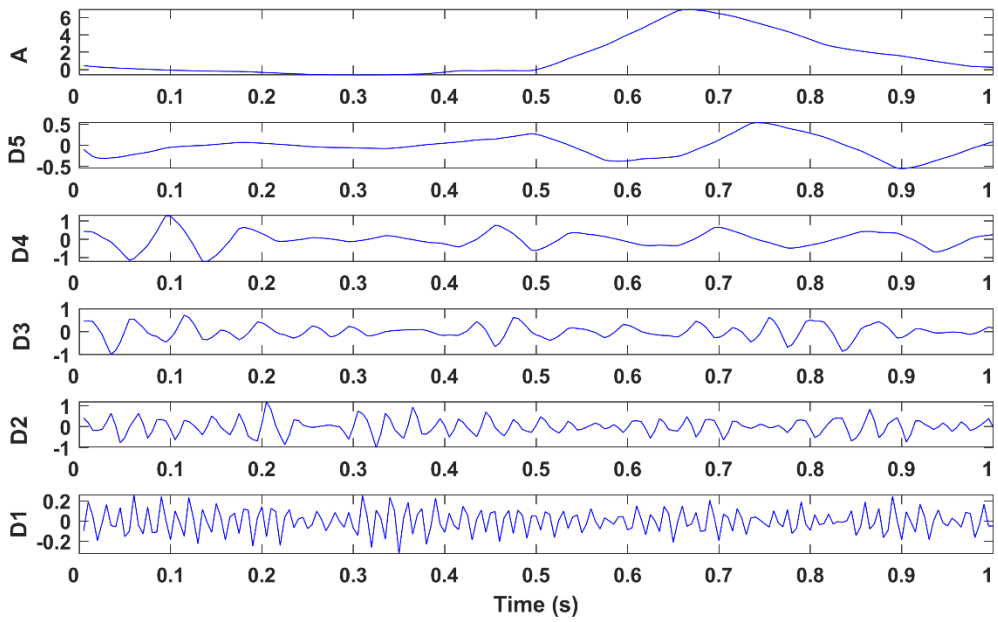

Figure 4-11: Wavelet decomposition of a target EOG peak signal window within an EOG artifact independent component.

4.2.2 Performance Metrics

The quality of artifact removal methods can be quantified by two basic types of metrics; metrics which describe the amount of artifact removed by a given cleaning method, and metrics that measure the distortion introduced in the signal by the cleaning process [126]. Two metrics of the first type are the artifact removal percentage λ and the signal-to-noise ratio difference [127].

When the true, uncontaminated EEG and the added artifact signals are known, the artifact removal percentage can be calculated as

$$\lambda = 100\left(1 - \frac{R_{ref} - R_{cleaned}}{R_{ref} - R_{contam}}\right) \quad (4.7)$$

where R_{ref} is the autocorrelation of the true EEG signal with time lag 1, $R_{cleaned}$ is correlation between the true EEG and the cleaned signals, while R_{contam} is the correlation between the true EEG and the artefactual signals. When $R_{cleaned}$ is close to the reference R_{ref}, the negative term tends to 0, hence a high lambda value indicates high efficacy in artifact removal. The difference in signal-to-noise ratio ΔSNR [127] is a similar measure characterizing the amount of artifact removed from the signals. It is defined as

$$\Delta SNR = 10\,log_{10}\left(\frac{\sigma_x^2}{\sigma_{e_{cleaned}}^2}\right) - 10\,log_{10}\left(\frac{\sigma_x^2}{\sigma_{e_{contam}}^2}\right), \quad (4.8)$$

where σ_x^2 is the variance of the true EEG signal, and $\sigma_{e_{contam}}^2$ and $\sigma_{e_{cleaned}}^2$ are the variances of the error signals $e_{contam}(n) = r(n) - x(n)$ and $e_{cleaned}(n) = r'(n) - x(n)$ with $x(n)$, $r(n)$ and $r'(n)$ representing the true EEG, contaminated and the artifact cleaned signals, respectively. Distortion in the time-domain can be quantified using the root mean square error calculated between the true EEG $x(n)$ and the cleaned signals $r'(n)$.

$$RMSE = \sqrt{\frac{1}{N}\sum_{n=1}^{N}(r'(n) - x(n))^2} \quad (4.9)$$

Spectral distortion can be measured by the magnitude squared coherence (MSC) [128] that computes the frequency-domain correlation between the pure and the cleaned EEG signals:

$$MSC = C_{xy}(f) = \frac{\left|R_{xy}(f)\right|^2}{R_{xx}(f)R_{yy}(f)}, \quad (4.10)$$

where $R_{xy}(f)$ is the cross spectral density between the two signals *x* and *y* at frequency f, and $R_{xx}(f)$, $R_{yy}(f)$ are the auto-spectral density of *x* and *y*, respectively. MSC is a frequently used metric for evaluating frequency-related distortions after artifact removal [70,83,129–132].

4.3 Results

This section presents the performance evaluation of the proposed EOG removal method. Three datasets were used; the Klados, the PhysioNet and the laboratory resting-state datasets. For each dataset, the proposed method (PM) is compared to the traditional full component rejection method (ICArej) [133] and the wavelet-enhanced ICA (wICA) [70] component correction methods using the performance metrics specified in section 4.2.2. wICA is also compared to rejection ICA to confirm its claimed higher performance.

4.3.1 Semi-Simulated EEG Dataset

The performance of the proposed method was first evaluated on the Klados datasets [117]. These measurements contain semi-simulated signals, containing resting-state measured signals with

and without added simulated EOG contamination. Access to the pure EEG signal allows for calculating accurate performance metrics. For illustrative purposes, Figure *4-12* shows the contaminated and pure EEG signals, as well as the absolute difference between the wICA-cleaned signal and the pure EEG, and the difference of the signal cleaned with the proposed method and the pure EEG signal. Note that the amplitude scales are different in order to make the difference signals visible. The contaminated segment shows three strong blink (Ch 1-4, 17-19) and two eye movement (Ch 11-12) artifacts. Note the difference between the difference signals (wICA–EEG_{true}, PM–EEG_{true}) obtained after cleaning with the wICA and the proposed method. The high-frequency content in the wICA difference signal indicates the removal of non-EOG signal components. Figure *4-13* shows a zoomed-in section of dataset12 (channel Fp1) illustrating how the PM cleaning method leaves the EEG signal intact outside the EOG zones, and how it follows the true EEG within the zones. The figures qualitatively indicate the improved removal quality of the proposed method.

a) Contaminated EEG signal, ±150 µV

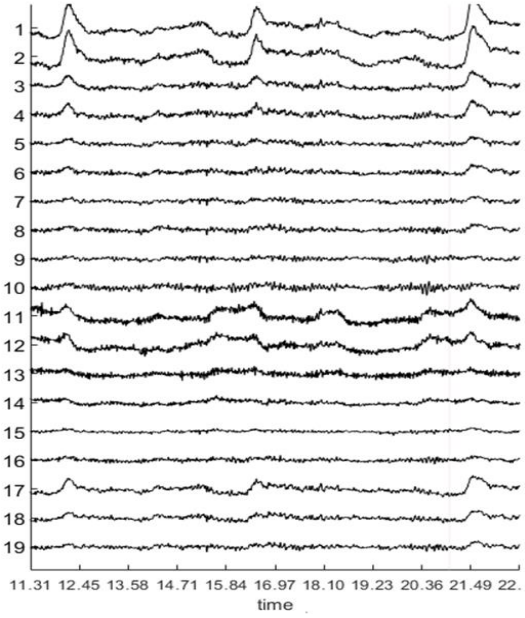

b) True EEG signal, ±50 µV

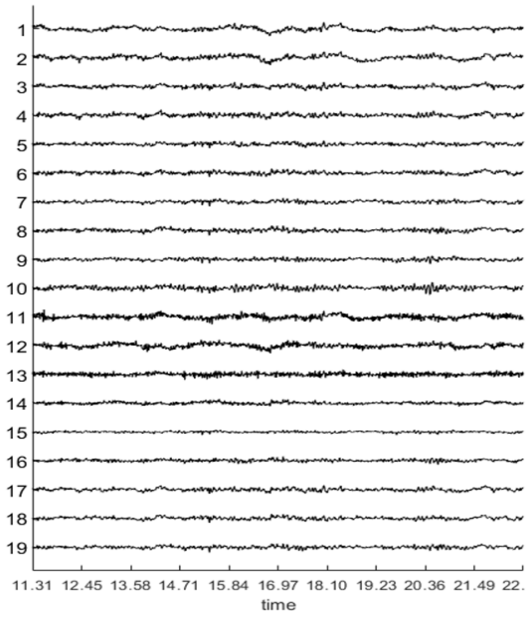

c) Difference of wICA-cleaned and true EEG signals , ±5 µV

d) Difference of PM-cleaned and true EEG signals, ±5 µV

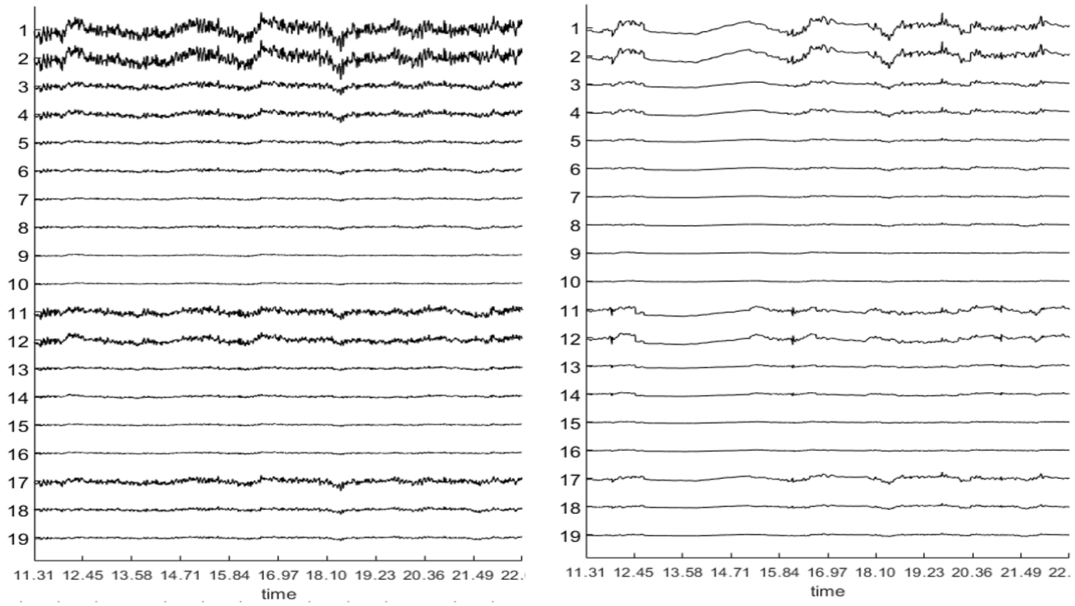

Figure 4-12: Illustration of the cleaning performance on one artifact contaminated section of the Klados dataset9. The two subplots on the bottom show the difference of the pure EEG data and the wICA and PM cleaned signals, respectively. Amplitude scales are different to make difference signal visible.

A quantitative statistical comparison was performed on the entire dataset (54 measurements), in which the λ, ΔSNR, $RMSE$ and MSC metrics were computed for each channel in each dataset with the three removal methods (rejection ICA, wICA, Proposed Method) under study. After λ, ΔSNR, $RMSE$ fare calculated for each channel, the distributions of the metrics for the dataset population are shown in Figure *4-14*. Each metric value set was checked for normality and equal variance (F-test). A two-sample t-test ($\alpha = 0.05$) was performed to decide whether there is a significant difference in performance between the PM and the wICA/ICArej methods for any metric. Performance of the wICA with respect to the rejection ICA method is also examined to verify claims that wICA outperforms rejection-based removal. The λ value showed no significant difference (average improvement: 11.34%, $p = 0.102$) between the wICA and the reject ICA methods. The Proposed Method, on the other hand, was significantly better (19.1%, $p = 0.00236$) than the wICA and 32.6% better ($p = 1.43\times10^{-5}$) than the reject ICA methods. With respect to the ΔSNR metric, the wICA method was significantly better than the reject ICA method (50.05%, $p = 2.08\times10^{-5}$). The Proposed Method, however, resulted in significantly increased SNR compared to wICA (79.5%, $p = 7.78\times10^{-15}$) and reject ICA better (169.34%, $p = 7.96\times10^{-36}$). The RMSE results are similarly positive; wICA improves upon reject ICA by 39.1% ($p = 3.89\times10^{-18}$), while the Proposed Method showed 36.32% improvement ($p = 5.84\times10^{-33}$) over the wICA and 61.22% over the reject ICA ($p = 5.80\times10^{-9}$) methods, reducing the average RMSE from 5.579 μV (wICA) to 3.553 μV.

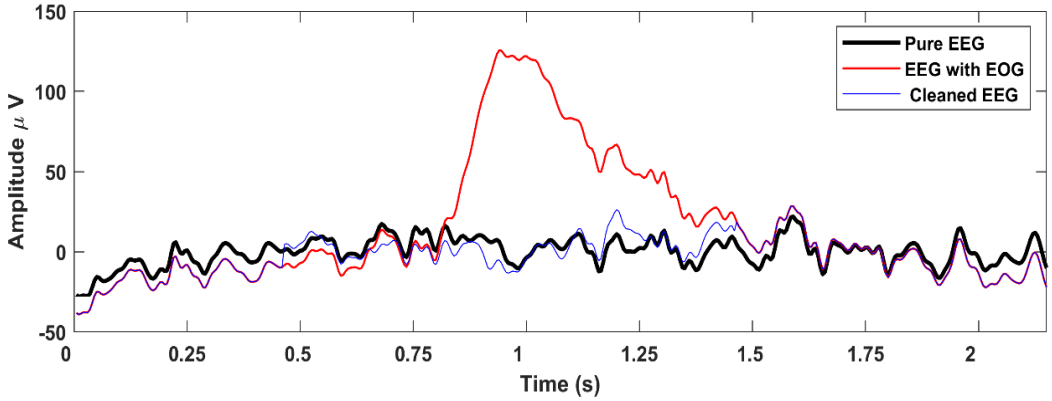

Figure 4-13: Comparison of the artifact-free, the contaminated and the PM-cleaned EEG signals of dataset9, channel Fp1.

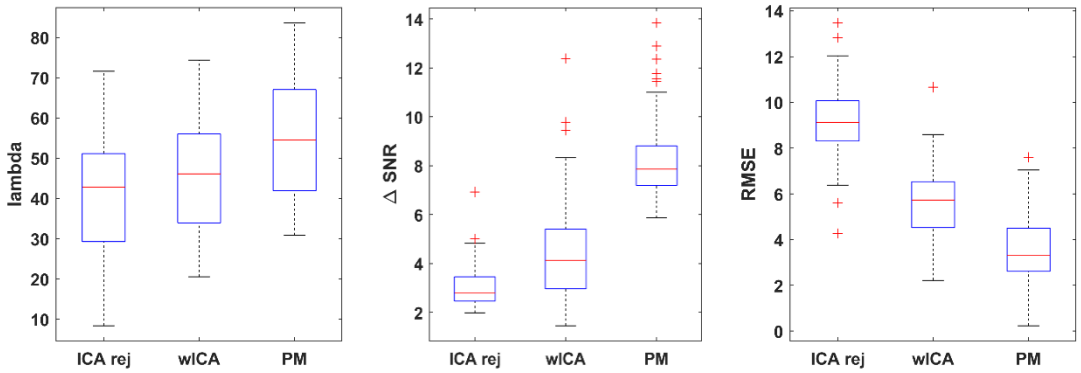

Figure 4-14: Distribution of the λ, $\Delta\ SNR$ and $RMSE$ dataset average values obtained with the rejection ICA, wICA and the proposed method. For λ and $\Delta\ SNR$ the higher, while for $RMSE$, the lower values mean better performance.

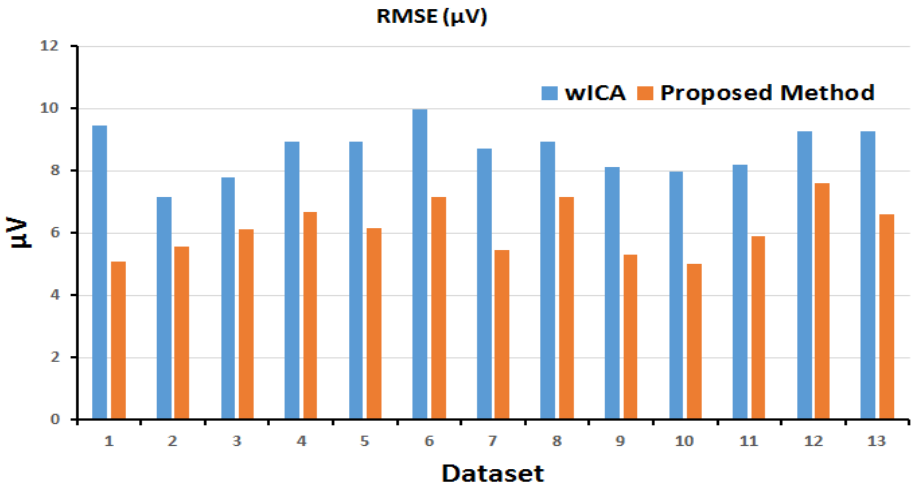

Figure 4-15: RMSE (μV) of the wICA and my proposed method on selected Kaldos dataset.

In addition to the statistical analysis, for enabling side-by-side comparison with the wICA method, Table *4-1* lists the RMSE values for the exact same datasets and channels that were reported in [70].

Dataset, channel	Contaminated EEG	ICA cleaned	wICA cleaned	Proposed method
Dataset 1, FP1	34.9	16.3	12.6	7.9
Dataset 1, F8	13.7	9.4	7.3	3.2
Dataset 2, FP1	37.8	14.6	8.7	4.6
Dataset 2, F8	15.9	8.4	5.4	1.5
Dataset 9, FP1	30.8	18.9	9.2	3.2
Dataset 9, F8	15.5	12.7	6.4	2.6
Dataset 12, FP1	38.4	14.9	9.8	7.2
Dataset 12, F8	18.8	11.3	7.2	3.5

Table 4-1: RMSE (μV) values of the different artifact removal methods.

While the RMSE result indicates improved removal quality in the time-domain, a key question remains as to how the spectral characteristics of the signal change after cleaning. Figure *4-16* illustrates the effect of artifact removal on the power spectral density of the EEG signals. The frontal channel Fp1 of *dataset12* was used to show the difference among the different methods. Note how the contaminated signal introduces strong $\delta - \theta$ frequency band distortions. The reject ICA and wICA methods decrease this low frequency distortion but introduce higher, α and β band frequency power increase. The proposed method, on the other hand, removes low frequency artifact-related distortions and follows the power density distribution of the pure EEG signal for higher frequencies with very little error.

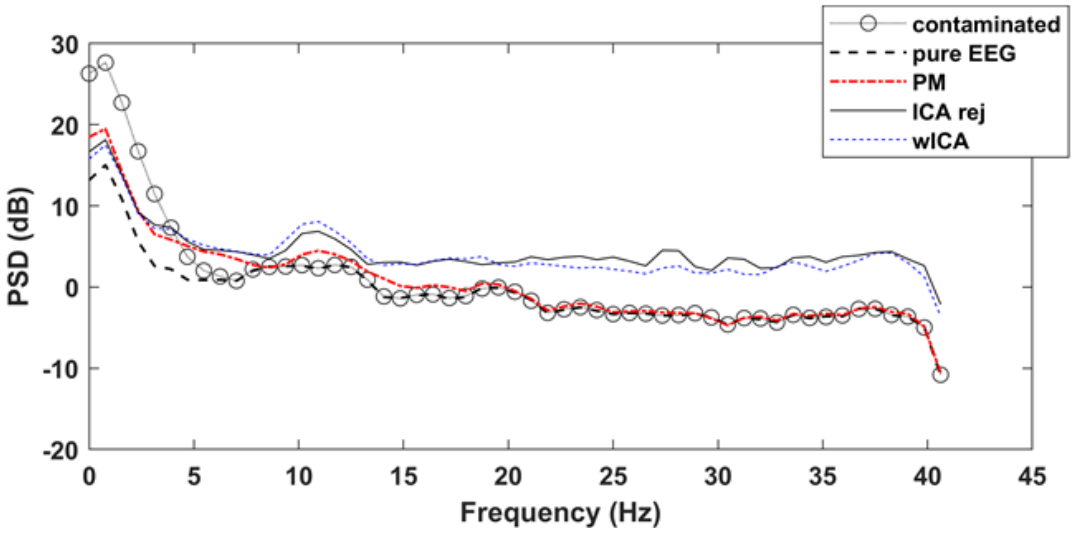

Figure 4-16: Power spectral density distributions of the pure, contaminated versus the ICA rej, wICA and PM method cleaned signals (dataset12, channel Fp1).

Performing the analysis for the entire dataset, the Magnitude Squared Coherence (equation 4.10) after cleaning with the Proposed Method was 13.69% better ($p = 4.20\times10^{-8}$) than the wICA results and 15.93% better ($p = 3.91\times10^{-8}$) than the reject ICA values. No significant difference was found between the wICA and reject ICA results ($p = 0.335$). Figure *4-17* shows the overall grand average MSC results for the three methods. The performance advantage of my proposed method over the rejection ICA and wICA methods is clearly demonstrated.

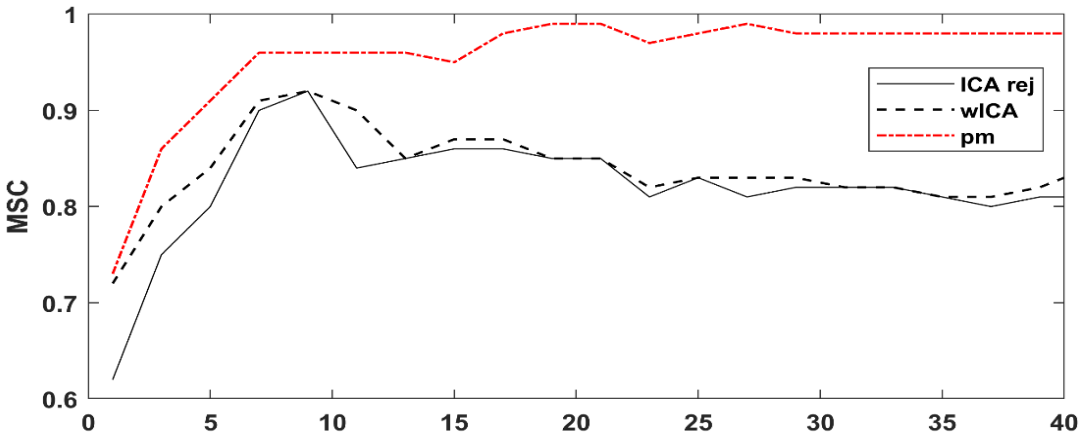

Figure 4-17: The grand average (20 datasets) MSC results of the three cleaning methods. Note the higher average performance of my proposed method.

Figure *4-18* shows, for a selected single frontal channel (Fp1, *dataset12*), the Magnitude Squared Coherence in order to compare the spectral accuracy of the different EOG removal methods in a non-averaged manner. The results indicate that the different EOG artifact cleaning methods produce different spectral distortion in frequencies below 7 Hz. Coherence is the lowest for the uncleaned, EOG contaminated signal. The rejection-based ICA and wICA methods both reduce this distortion, but it is my proposed method that produced coherence values closest to the ideal value of 1. Note that wICA also introduces slight distortion in the 7-17 Hz range as well, which might be the result of unnecessary removal of higher frequency wavelet components.

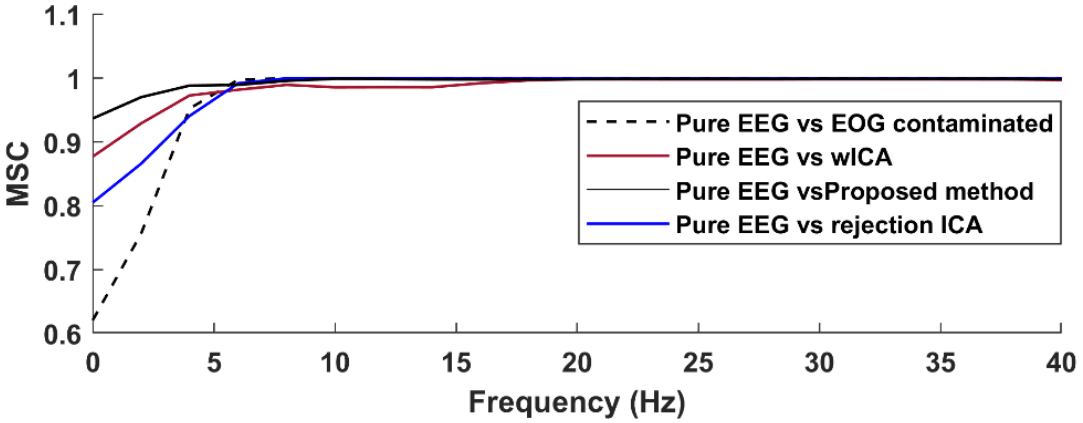

Figure 4-18: The magnitude squared coherence (MSC) between the pure EEG signal and the contaminated signal as well as the various cleaned signals (dataset12, Fp1).

4.3.2 Resting State EEG Dataset

To evaluate the performance of my method on real EEG data, 2-3 minute-long 128-channel resting state EEG measurements of 10 subjects (obtained in our laboratory) were used. Since the true, artifact-free EEG signals are unknown in this case, modified performance metrics were used. The true EEG signal was estimated for each subject from a manually selected 5-second long artifact-free segment. The datasets were then cleaned with the three different methods and partitioned into 5-second long segments. The performance metrics were subsequently calculated by using the entire signal (all 5-second segments) with respect to the reference segment in the corresponding formulae. The distribution of the results for each method are shown in Figure *4-19*.

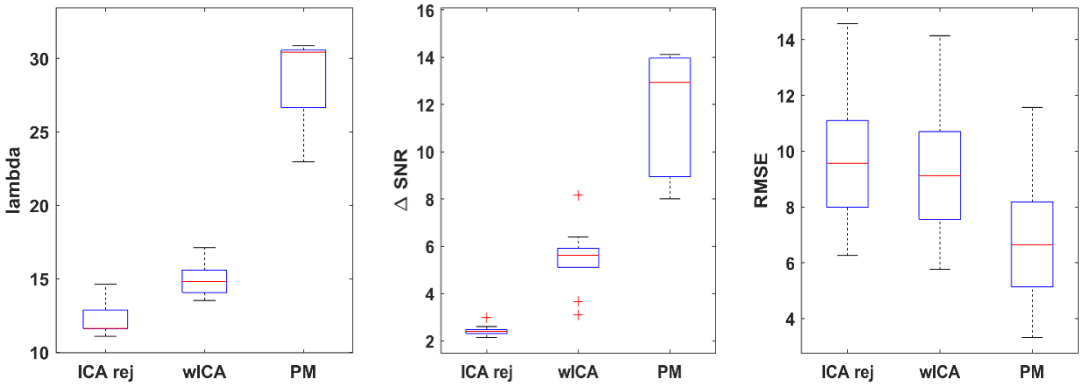

Figure 4-19: Distribution of the λ, $\Delta\ SNR$ and $RMSE$ dataset average values for the resting state laboratory measurements obtained by cleaning with the rejection ICA, wICA and PM methods. For λ and $\Delta\ SNR$ the higher, while for $RMSE$, the lower values mean better performance.

While the range of values are lower (λ and $\Delta\ SNR$) or higher ($RMSE$) than those obtained for the semi-simulated Klados dataset (due to the different estimation of the true EEG), the trend in performance is the same. Performing the same statistical analysis as for the semi-simulated Klados datasets, the Proposed Method achieved 154.61% (p = 6.86×10-9) improvement for λ over the wICA and 136.88% better (p = 8.28×10-10) than the reject ICA methods. The wICA method achieved 6.97% (p = 2.06×10-5) improvement over the reject ICA method. With respect to the $\Delta\ SNR$ metric, the Proposed Method achieved 388.88% improvement (p = 7.83×10-7) over the reject ICA and 116.45% (p = 6.28×10-6) over the wICA method. The wICA method performed better than reject ICA by 125.87% (p = 5.80×10-5). The $RMSE$ results showed the Proposed Method achieved 26.94% improvement (p = 0.039) over the wICA and 30.37% over the reject ICA (p = 0.0165) methods. No significant difference was found between the wICA and reject ICA methods (4.7%, p = 0.6887). For the spectral coherence MSC, the proposed method improved over both the wICA (19.12%, $p = 5.89\times10^{-5}$) and the reject ICA (23.5%, $p = 6.73\times10^{-6}$) methods. On the other hand, no significant difference was found between the reject ICA and wICA methods (3.68%, p = 0.423479).

Similar results were obtained for the spectral distortion. The MSC values for the proposed method are significantly higher than for the ICArej and wICA methods.

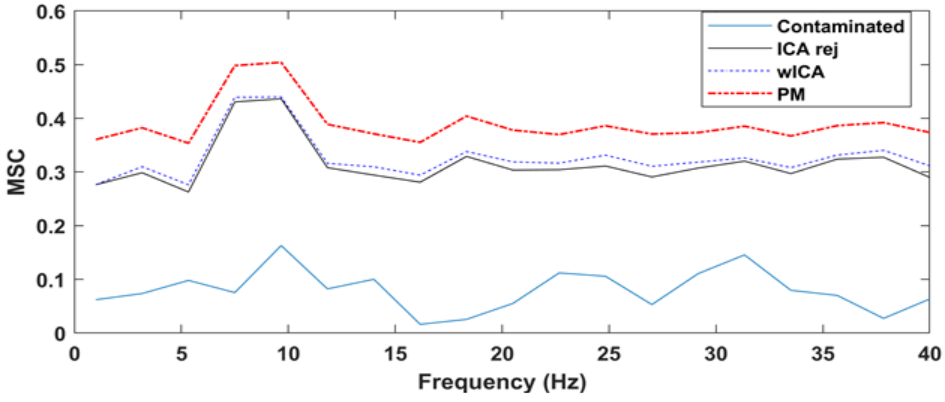

Figure 4-20: MSC values obtained with different cleaning methods for the resting state laboratory dataset (20 subjects).

As a qualitative illustration of the effect of my removal method on real measurement data, Figure *4-21* shows a 20-second section of the contaminated resting state EEG before and after EOG removal (Proposed Method). Figure *4-22* illustrates the same effect on a 2D scalp potential map at the peak of an EOG artifact. The EOG artifact is clearly visible in the frontal area that disappears after cleaning. Note also the emerging parietal topography in the cleaned version which is almost completely hidden in the contaminated map.

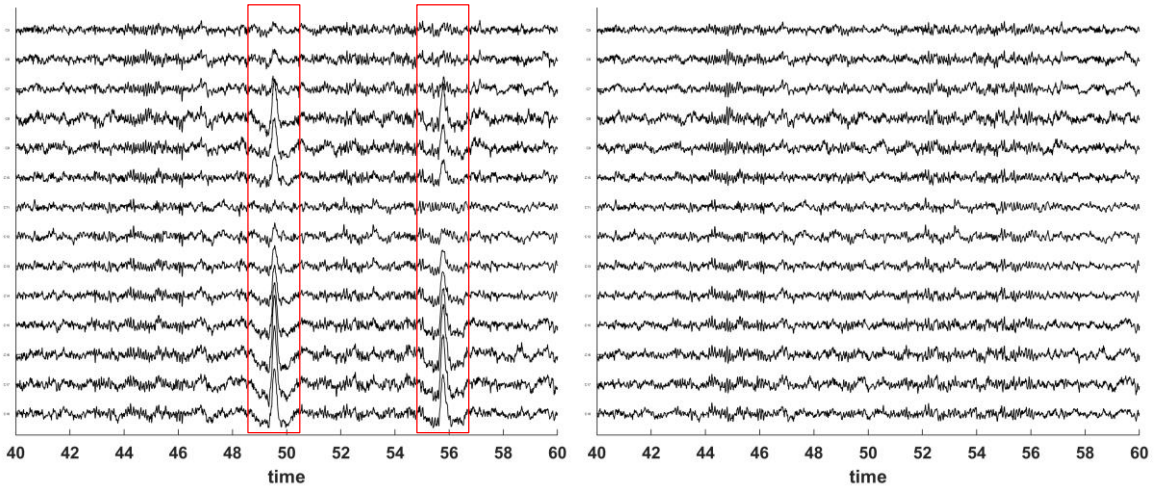

Figure 4-21: A 128-channel EOG contaminated EEG dataset before (left) and after (right) artifact removal.

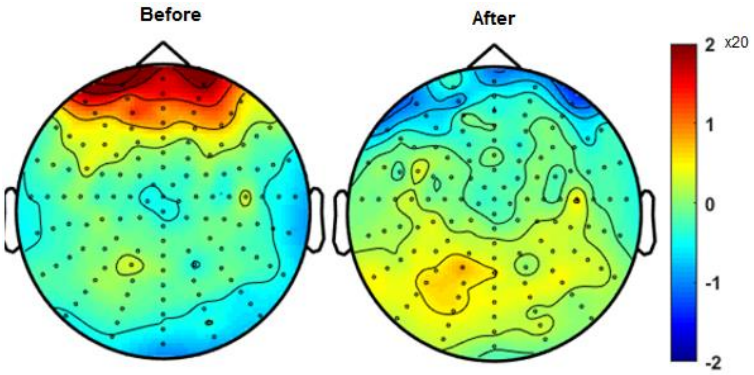

Figure 4-22: Topoplot potential map (µV) of a 128-channel EOG contaminated resting state measurement before (left) and after artifact removal (right).

4.3.3 PhysioNet P300 ERP Dataset

Peak detection performance

The accuracy of peak detection is crucial in the proposed method. Since the Klados and PhysioNet datasets contain annotations for EOG events, these were used to verify the performance of my EOG peak detection approach. Peak detection performance is characterized by the sensitivity measure, *Se* = TP/(TP+FN), where TP is the number of true positive (accurately detected), FN is the number of false negative (missed) peaks. The results are as follows. Klados dataset (218 EOG peaks, TP=217, FN=1): Se=99.54%; PhysioNet dataset (78 EOG peaks, TP=78, FN=0): Se=100%.

Artifact removal performance

The PhysioNet P300 dataset was originally created to detect and classify P300 peaks in the BCI speller experiment [62,134] and as such, can be used to examine the proposed method for cleaning task-oriented event related potential data. Two tests were conducted to verify whether or not the cleaning methods distort ERP waveforms and peaks. First, a statistical analysis was performed on the RMSE values to verify the presence of significant improvements; second, the distortion effects of the different cleaning methods were examined.

For the statistical analysis, from among the target and non-target epochs, the target epochs were selected that elicit the P300 component. These resulted in 21 stimulus-locked epochs of length 500 ms extracted from the original contaminated 64-channel measurements for each subject (subjects s03, s04, s08, recording *rc02*). From these 21 epochs, the artifact free epochs were selected manually and averaged for estimating the reference, pure P300 ERP signal ERP_{ref} (number of epochs varied from 16 to 19) and averaged to generate a pure reference ERP signal. The contaminated P300 (ERP_{contam}) was computed by averaging the 21 uncleaned epochs. Then, the original recordings were cleaned with the three removal methods in question (rejection ICA, wICA, PM), and an ERP signal for each method was generated by averaging the 21 segments of the cleaned signals resulting in ERP_{clean}^{rej}, ERP_{clean}^{wICA} and ERP_{clean}^{PM}. Since the ERP waveforms differ from channel to channel, the channels were not averaged to calculate group statistics. Instead, subjects were selected individually then a statistical test was performed using the 64 channel-ERPs as sample population for pairwise comparison of the removal methods. The two-sample t-tests for each subject produced the results shown in Table *4-2*. The Proposed Method performed significantly better than the wICA or rej ICA methods for each subject.

Dataset	**RMSE improvement (%)**		
	PM vs rej ICA	**PM vs wICA**	**wICA vs rej ICA**
s03, rc02	**17.16** (p = 4.74×10^{-4})	**34.18** (p = 0.0286)	**20.55** (p = 0.049)
s04, rc02	**24.64** (p = 0.0018)	**16.46** (p = 0.0264)	9.79 (p = 0.2062)
s08, rc02	**25.62** (p = 0012)	**14.43** (p = 0.0348)	13.08 (p = 0.0992)

Table 4-2: RMSE improvement between methods. Bold values mark significant differences.

The distortion of the removal methods was tested two ways. First, the pure ERP signal was compared to the cleaned ERP signals averaged from the same epochs as the pure ERP (artifactual epochs excluded). This shows the distortion of each method operating on artifact-free data (Figure *4-23*). The rej ICA and wICA introduce larger distortions, since the entire signal is affected by EOG removal, even if only artifact-free epochs are averaged afterwards. By using the Proposed Method, however, artifact-free sections of the signal are unaffected, and the averaged clean epochs are nearly identical to the reference signal. See inset in Figure *4-23*(a).

10^1

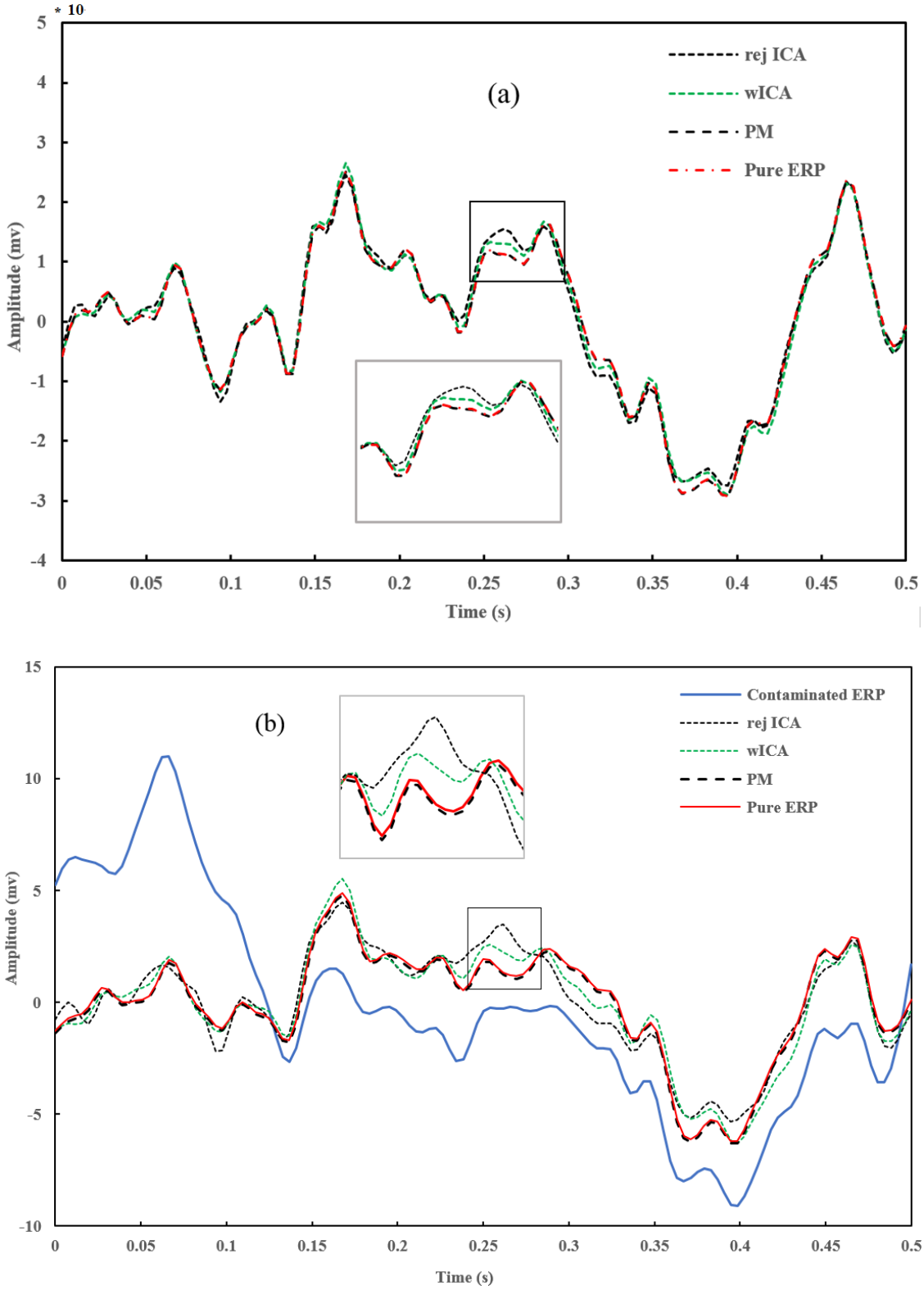

Figure 4-23: ERP signals computed from artifact-free epochs only (a) and ERP signals computed from all cleaned epochs (b) showing the distorting effects of the cleaning methods on ERP curves. ERP_{clean}^{PM} produced the smallest difference in both cases. (dataset, electrode Fpz).

4.4 Summary

In this chapter, I described an improved wavelet-based ICA method for removing EOG components from EEG measurements. The wavelet-enhanced ICA (wICA) [70] method showed that independent components can be cleaned from artifacts if they are not rejected entirely. As shown in the Results section, correcting components this way not only preserve information, but also reduce distortions that rejection ICA methods introduce in the time and frequency domain. Distortions in the frequency domain, for instance, can corrupt EEG-based connectivity analyses [70]. The novelty of the method proposed in this work is that component artifact correction is only performed in EOG contaminated sections of the component, ensuring that non-EOG contaminated sections are left untouched. The statistical analysis of the artifact removal performance metrics confirmed that while wICA outperforms rejection ICA methods in most performance parameters my Proposed Method significantly outperformed the quality of both the wICA and the rejection ICA EOG cleaning methods, both in the time and spectral domains, resulting in close-to-ideal pure EEG signals. The proposed method is able to automatically detect and correct both the vertical EOG activity (blinks) and horizontal EOG artifacts (eyes movements), which makes it suitable for unsupervised artifact removal applications. In addition, my method is fully automatic; it does not require manual component and artifact inspection, which can simplify and speed up high-quality artifact removal processes.

5 Removal of Cardiac ECG Artifacts

In this chapter, I propose a fully automatic method for removing ECG artifacts from EEG signals. As for EOG removal, my approach is based on using Independent Component Analysis (ICA) to separate the observed signals into statistically independent source components, some of which may be attributed to artifact sources. ECG-related independent components are then classified using an ECG detection method, and these identified components are removed from the component set to reconstruct the EEG data with ECG artifacts removed. A sophisticated classification method ensures that only components that reflect real ECG activity are rejected. The main advantage of my method is that (i) it is fully automatic, (ii) it does not require a reference ECG channel, thus can be used in situations where ECG data is not available, and (iii) it can also detect and remove ECG artifacts generated by pathological cardiac activities which can make the method more robust when analysing EEGs of elderly patients.

5.1 Subject and Methods

5.1.1 Pre-processing

Signals of each dataset were filtered with a 1 – 47 Hz 4th-order zero-phase Butterworth bandpass filter to remove the DC component, slow drifts, line noise and unwanted high-frequency components. The resting state measurements were then down sampled to f_s = 256 Hz. This optional step was chosen to reduce the execution time of the subsequent ICA algorithms (e.g. Infomax ICA, Fast-ICA, JADE, SOBI). Average reference (removing the average of all channels at each time point from each channel) was used for the resting state dataset.

The flow chart of the proposed method that includes signal pre-processing, independent component analysis and subsequently, component checks for ECG presence and artifact removal is shown in Figure 5-1. Each step of the method is described in detail in the following subsections.

The pre-processed signals were partitioned into 20-second long non-overlapping segments. The Infomax ICA algorithm was performed on each segment to generate components.

5.1.1.1 ECG Component Detection

The output of the ICA algorithm is a set of independent components, c_i , i = 1, …, N, where N is the number of components that is also equal to the number of EEG channels. The input of the ICA is the recorded dataset of n channels, and the output of the ICA are n independent sources, where each source collects its specific features which spread over the entire channels to be collected in one independent component. Since the order of the components produced by the ICA algorithm is arbitrary, I cannot pre-select components based on a-priori information; each component has to be examined for ECG-like activity. The underlying assumption is that an ECG independent component is similar to a real ECG signal in terms of its QRS interval, general waveform morphology, and quasi-periodicity [135] (see Figure *5-2* as an example). Since the most characteristic feature of an ECG signal is the QRS complex, the presence of this is used for identifying an ECG artifact component.

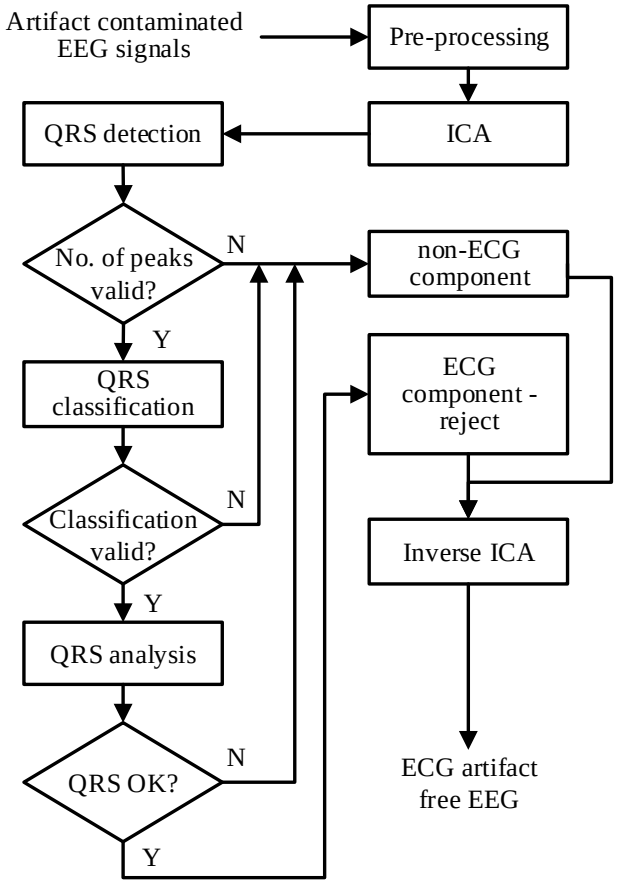

Figure 5-1: The flow chart of the ECG artifact removal method.

The complete ECG component detection hence involves the following two main stages: first, an automatic QRS detection is performed on an independent component, c_i, and then an ECG-cycle classifier decides whether the given component is in fact an ECG artifact component. These stages include several internal processing steps which I describe in detail as in the followings.

Step 1 – Amplitude range transformation

The component signal, c_i, is segmented into K consecutive, non-overlapping, two-second data segments, s_j, $j = 1, \ldots, K$. Then, the local maximum, $m_j = \max_{y_k \in s_j}(y_k)$, is calculated in each segment, where y_k is the vector of samples of segment s_j, $k = 1, \ldots, L$, and $L = 2f_s$. Once the local maxima of all segments are determined, their median is calculated, $med = \text{median}(m_j)$, and finally, the component signal is transformed into the ±700μV range that is required for the QRS detection algorithm:

$$\hat{y}_k = \frac{700}{med} y_k. \qquad (5.1)$$

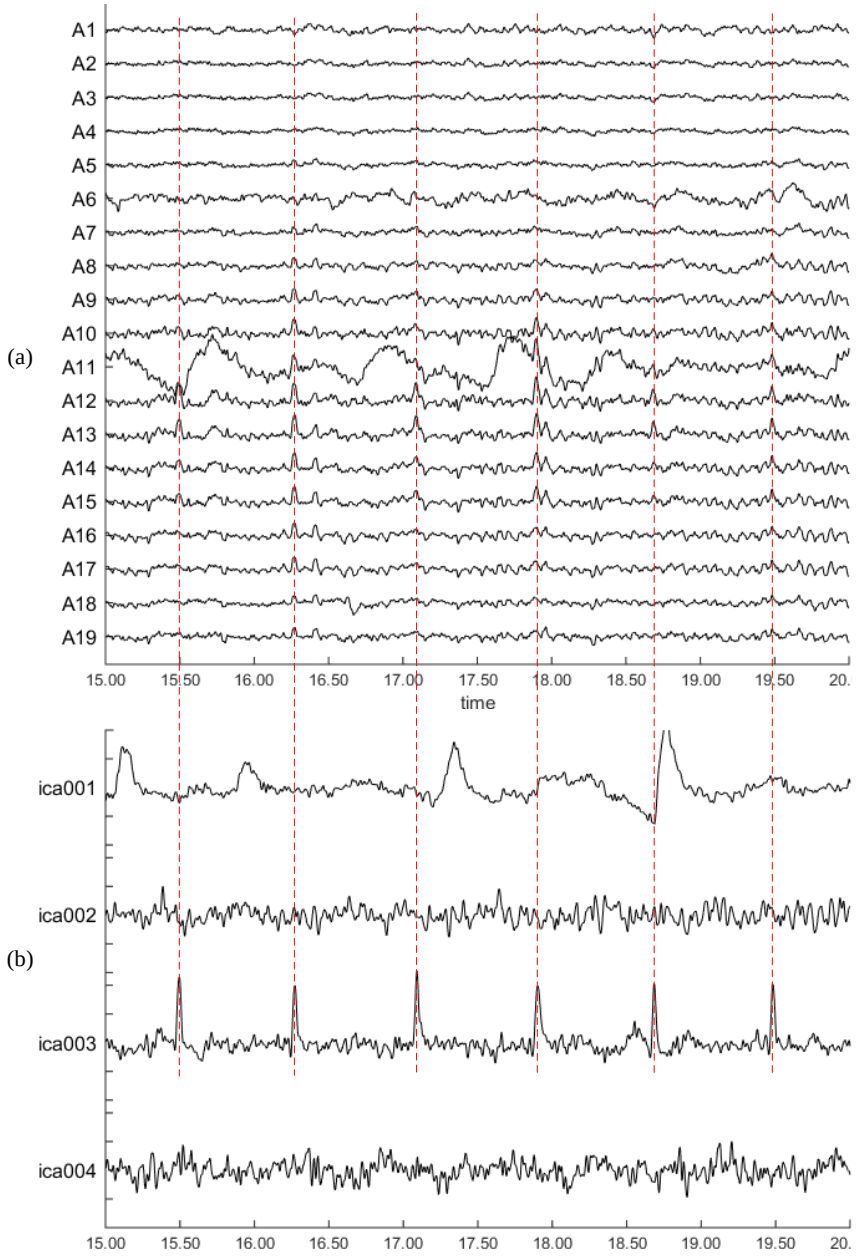

Figure 5-2: Input signals of a 128-channel EEG signal data segment contaminated with artifacts (a), and a subset of the resulting independent components representing EEG signals (ica002, ica004), ocular (ica001) and cardiac artifacts (ica003) (b).

Step 2 – QRS detection

The next step of the method is scanning the independent components for the presence of ECG waveforms, i.e. QRS complexes.

In my example in Figure *5-2*, component ica003 shows ECG features. The QRS detection step uses an adaptive threshold-based R-peak detection algorithm developed by Christov [136] (recent algorithm has better sensitivity, positive productivity and Numerical Efficiency [137]). The algorithm operates on the derivative of the component signal $c(t)$. Let $y(t)$ denote the absolute value of the derivate,

$$y(t) = |c'(t)| \approx \left|\frac{c(t+h)-c(t-h)}{2h}\right| = \frac{|c_{k+1}-c_{k-1}|}{2\Delta t}, \qquad (5.2)$$

where $c_{k+1}$and c_{k-1} are the $(k+1)^{th}$ and $(k-1)^{th}$ samples of the given component segment s_j of the current component.

A combined adaptive threshold function

$$MFR = M + F + R, \qquad (5.3)$$

is calculated for each time instant using: (*i*) *M* (the steep-slope threshold), (*ii*) *F* (the integrative threshold for high-frequency signal components, and (*iii*) *R* (the beat expectation threshold). The exact rules for calculating the adaptive threshold can be found in [136].

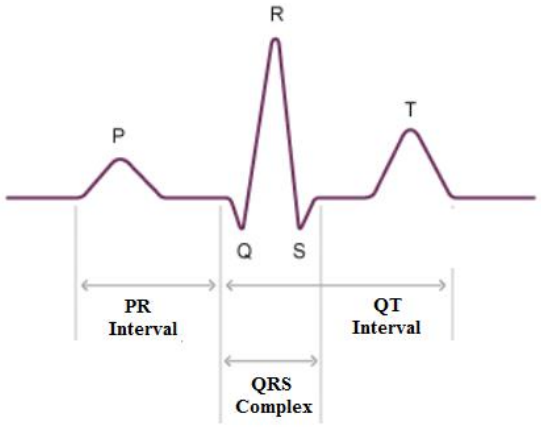

Figure 5-3: The simplified QRS interval[3] of a human ECG signal.

Each derivate sample y_k is compared to the *MFR* threshold, and the position of the first sample for which the condition $y_k > MRF$ holds is stored as an R-peak position. Since the algorithm may not always pick the true position of the R-peak, a local peak search is performed subsequently within the neighbourhood of each detected position to find the global maximum in the window centred on the initial R-peak position. The positions of the final detected peaks are then stored for the next (classification) stage of my method.

1) The first ECG detection criteria is related to the number of detected peaks; if it is outside the normal human heart rate (<30 or >250 beats/minute), the algorithm skips the component (i.e. marks it as non-ECG).

[3] Image source: https://www.nottingham.ac.uk/nursing/practice/resources/cardiology/function/normal_duration.php

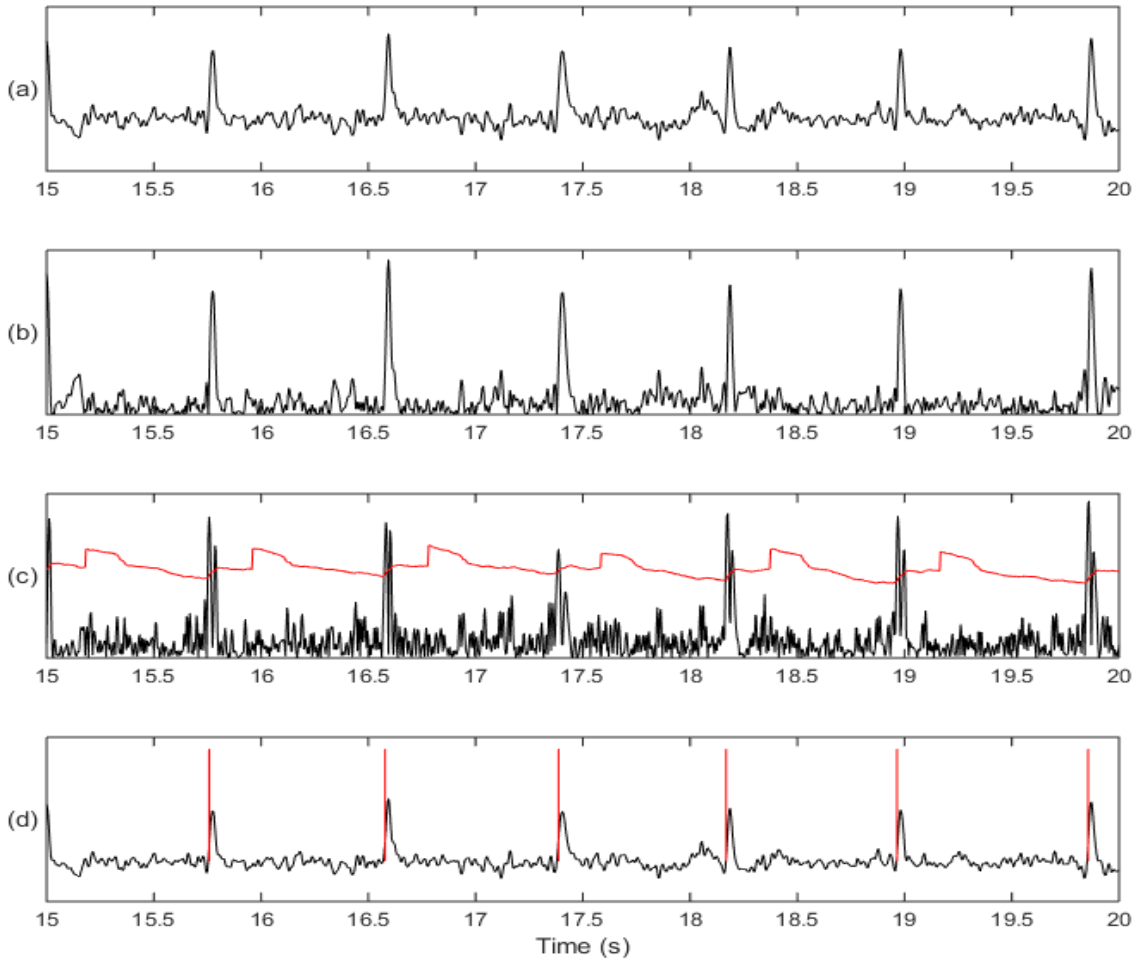

Figure 5-4: Successive steps of the ECG artifact detection process; (a) ECG independent component, (b) absolute value of the component, (c) absolute value of the component derivative and the MFR adaptive threshold (solid red line), (d) QRS peaks detected.

Step 3 – Cardiac cycle classification

The goal of the classification stage is to verify whether the detected peaks can be attributed to cardiac activity. If the peaks do not show characteristic ECG properties (cycling appearance, QRS distance) the component will be labelled as a non-ECG component. The details of the classification process are described below.

2) The next step is the classification of the cardiac cycles, $\boldsymbol{h}_k$, into a majority heart cycle class and possible extra classes (e.g. low-quality majority cycles, extreme amplitude artifacts). Using the detected R-peak positions as synchronization points, an average ECG waveform, $\boldsymbol{h}_{avg}$, is generated by defining a -300ms to 400ms window around each candidate peak, and the corresponding samples are averaged point-by-point. The selected time window -300ms to 400ms well representing the low and normal heart rates, this is proved based on the results, and since ECG is recorded from EEG during resting or task related, where the subject relaxed and no high heart rate is found.

The generated averaged ECG will serve as a reference waveform in the classification of each cardiac cycle.

After this step, the Pearson-correlation is calculated between the average baseline ECG, $\mathbf{h}_{avg}^{QRS}$, and each interval waveform, $\mathbf{h}_{k}^{QRS}$, using a narrower QRS [-60ms, 80ms] window. If the correlation and the amplitude of the waveform are above the pre-determined threshold values, the interval is assigned to the majority ECG class C_{ECG}. The following formula defines the rules more formally:

$$C_{ECG} = \{\mathbf{h}_k | k \leq H, \text{corr}(\mathbf{h}_{avg}^{QRS}, \mathbf{h}_{k}^{QRS}) \geq 0.7 \text{ and } | \max(|\mathbf{h}_{avg}^{QRS}|) - \max(|\mathbf{h}_{k}^{QRS}|) | < 0.5 * \max(|\mathbf{h}_{avg}^{QRS}|)\} \quad (5.4)$$

where $\mathbf{h}_k$ is the sample vector of the k^{th} detected cardiac cycle in the ICA component segment under test, H is the number of detected cycles, $\mathbf{h}_{avg}^{QRS}$ is the vector of samples of the averaged QRS cycles [-60ms, 80ms], and $\mathbf{h}_{k}^{QRS}$ is the vector corresponding to the same window of cardiac cycle k, $k = 1, \ldots, H$.

3) Next, the majority class is examined for consistency and beat periodicity. If there are too few ECG cycles in the majority class (less than 10% of the total number of detected cycles) or the detected heart rate in the class is outside the valid human heart rate (<30 or >250 beats/minute), the component is not considered as ECG artifact.

4) If the majority class test succeeds, the final verification step is based on the average QRS interval. ECG cycles in the majority class are averaged, then the QRS interval is calculated after locating the QRS onset and offset on the averaged cycle. If the QRS interval is too narrow or too wide (<30 or >200ms), the majority class – and consequently the current component – is not classified as an ECG artifact. The component is marked as ECG if and only if it was not rejected in any of the preceding steps.

5.1.1.2 Component Removal and Inverse ICA

The final step of the method is the reconstruction of the signal from its components. The rejected independent components are removed from the component set, $\hat{s}$, creating an artifact-free set, $\hat{s}^{af}$, by zeroing out the rejected component samples, $\hat{s} \rightarrow \hat{s}^{af}$, then the estimate of the cleaned observed EEG signal can be computed as

$$\hat{\mathrm{x}}_t = W^{-1}\hat{s}_t^{af} \quad (5.5)$$

Once the ECG classifier identifies an ECG independent component, the entire ECG component waveform (not just the QRS complex) is rejected from the set of components. Figure *5-5*, illustrates the result of the cleaning method, whereas Figure *5-6* compares the original, contaminated channel A13 of Figure *5-6* with the one after artifact removal. Note how the ECG peaks are removed from the signal without introducing any additional distortion. A different view of the cleaning effect is shown in Figure *5-7* which shows the scalp potential map of a QRS-peak interval before and after artifact removal. The original contaminated map clearly shows the typical spatial distribution pattern of an ECG artifact. The artifact-free map illustrates to what extent the ECG artifact concealed the underlying resting-state activity.

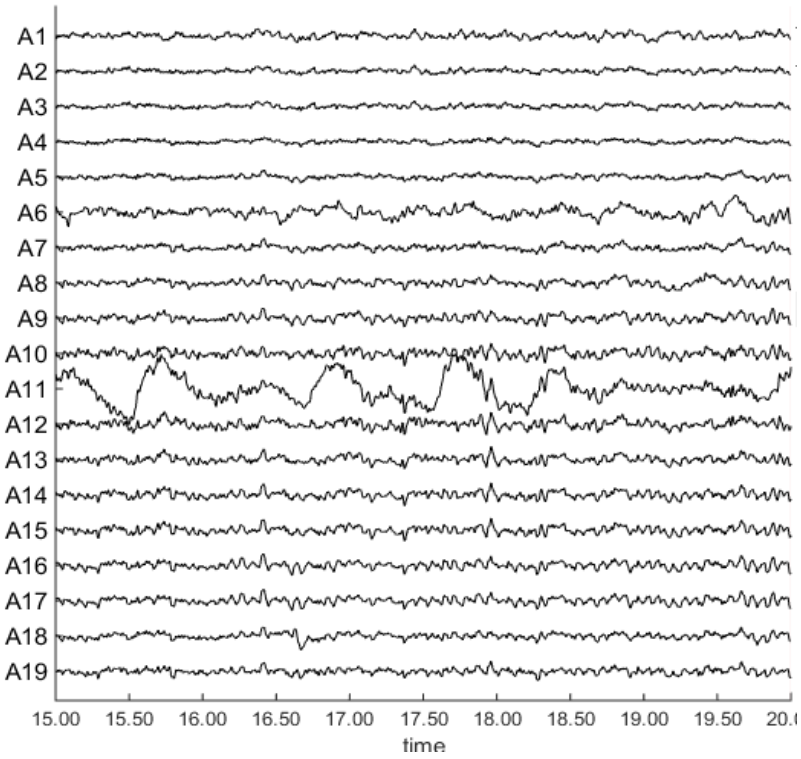

Figure 5-5: EEG signals with the ECG artifact removed. Compare channels A12-A15 with the contaminated originals in Figure 5-2.a.

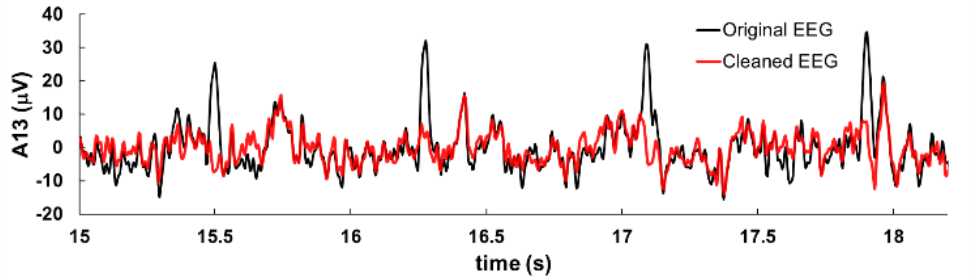

Figure 5-6: The original (black) and cleaned (red) samples of channel A13 of Figure 5-2.a. Note the four removed QRS peaks.

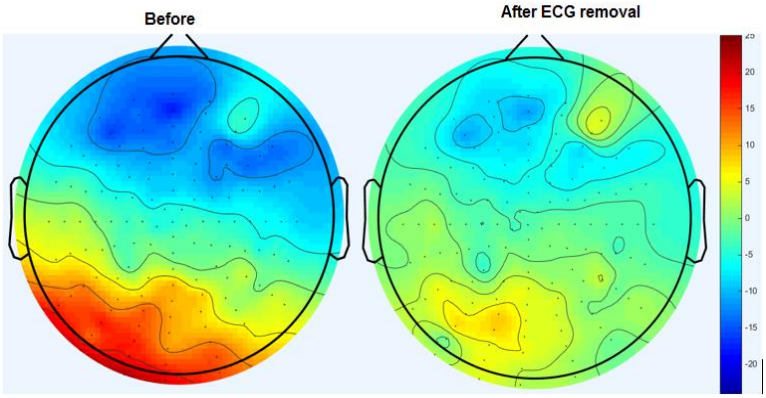

Figure 5-7: The scalp potential distribution of the averaged QRS peak before (left) and after (right) ECG artifact removal. Note the superimposed left-occipital–right-frontal ECG potential field (marked by the black arrows) disappearing after cleaning

Several metrics were selected to measure the performance of the proposed method. The accuracy of the QRS detection is described by the sensitivity, Sen $= TP/(TP + FN)$, where *TP* is the number of true positive (accurately detected), whereas *FN* is the number of false-negative (missed) QRS peaks.

The performance of the classifier is also measured by the sensitivity, as well as the specificity, Spe $= TN/(TN + FP)$. In both cases, *TP* is the number of true 20-second ECG independent component segments, *TN* is the number of non-ECG component segments, *FN* is the number of true ECG component segments rejected by the classifier rules (amplitude, periodicity, QRS interval, number of cycles in the majority beat class) and *FP* is the number of false-positive segments.

5.2 Datasets

Multiple EEG datasets were selected for testing my method. Public EEG datasets used in similar studies [9], [10] were included for performance comparison purposes. I have also used resting state EEG data measured by our group on healthy volunteers who all had given their written consent in participating in the experiments.

PhysioNet EEG datasets

a) The MIT-BIH Arrhythmia Database [138] contains 48 half-hour excerpts of two-channel ambulatory ECG recordings with sampling frequency is 360Hz, recorded at the Boston's Beth Israel Hospital.

b) The MIT-BIH Polysomnographic Database [19,134,138] contains sleep measurements of varying duration (ranging from 1:17 to 6:30 hours) from 16 patients monitored in the Boston's Beth Israel Hospital Sleep Laboratory. The datasets contain one EEG channel. The sampling rate of the measurements is 250 Hz.

c) The CAP Sleep Database is a collection of 108 polysomnographic recordings measured at the Sleep Disorders Centre of the Ospedale Maggiore of Parma, Italy [134,138]. Each dataset contains at least three EEG channels as well as ECG, EOG, respiration, etc. physiological signals. The sampling rate of the measurements is 250 Hz.

Resting state EEG dataset

Closed and open eye resting state EEG data was recorded from 61 adult volunteers (males and females, from ages 17 to 35) of 2-3 minute's duration. During the experiment, subjects had to sit and relax in a silent room. Data were recorded using a Biosemi ActiveTwo EEG system (f_s = 2048 Hz) using the 128-channel ABC radial electrode layout. The volunteers gave their written consent to participate in the experiments.

5.3 Results

My proposed method was tested on publicly available datasets and on resting-state EEG data obtained in our laboratory. The public datasets I selected are the MIT/BIH Arrhythmia, the MIT/BIH Polysomnographic and the CAP Sleep datasets. These allow my method to be compared with results reported in the literature [9,10]. The outcome of these comparisons can be found in Table *5-1*:Table *5-3*. The overall performance of my proposed method depends on the

performance of the QRS detector and the ECG component classifier. Both are examined in terms of their Sensitivity, Sen, and Specificity, Spe.

5.3.1 Artifact Detection Performance Metrics

The sensitivity of the QRS detector is calculated as Sen $= TP/(TP + FN)$, where *TP* is the number of true positive (accurately detected), whereas *FN* is the number of false-negative (missed) QRS peaks. I cannot use the standard formula for the Specificity, Spe $= TN/(TN + FP)$ for the QRS detection tests, as each input signal contained QRS complexes, consequently, the true negative case *TN* is undefined. Instead, I use the alternative formulation Spe* $= TP/(TP + FP)$ as suggested in [136].

The performance of the classifier is also measured by sensitivity and specificity. In this case, *TP* is the number of true ECG independent component segments, *TN* is the number of non-ECG component segments, *FN* is the number of true ECG component segments rejected by the classifier rules (amplitude, periodicity, QRS interval, number of cycles in the majority beat class) and *FP* is the number of false-positive segments (falsely detected QRS segments). The specificity of the component classifier is calculated using the traditional formula, Spe $= TN/(TN + FP)$.

5.3.2 QRS Detector Performance

Table *5-1* shows the results of my QRS detection method performed on ECG signals of the MIT/BIH Arrhythmia database using one and five-minute-long data segments.

Dataset	**Sen (%)**			**Spe* (%)**	
	Dora [9]	**PM** (1 min)	**PM** (5 min)	**PM** (1 min)	**PM** (5 min)
100m	97.1	100.0	100.0	100.0	100.0
101m	100.0	100.0	99.7	100.0	99.7
103m	100.0	100.0	100.0	100.0	100.0
106m	91.5	100.0	96.6	100.0	96.7
107m	100.0	100.0	100.0	100.0	100.0
117m	100.0	100.0	100.0	100.0	100.0
118m	100.0	100.0	100.0	100.0	100.0
208m	89.4	98.9	97.5	99.0	97.5
223m	92.2	100.0	100.0	100.0	100.0
231m	100.0	100.0	99.3	100.0	99.3
avg.	**97.0**	**99.9**	**99.3**	**99.8**	**99.0**

Table 5-1: QRS detection sensitivity and specificity, proposed method (pm, 1 and 5- minute segments) vs literature: MIT/BIH Arrhythmia dataset – ECG signal.

Table *5-2* and Table *5-3* show the results of my QRS detection method applied to the MIT/BIH Polysomnographic and the CAP sleep datasets. For both datasets, I ran the Infomax ICA to calculate the independent components. From this, each component is used as an input to the QRS detector to detect the ECG component.

Dataset	Sen (%)			Spe* (%)
	Dora [9]	**Jiang** [10]	**PM**	**PM**
slp01a	98.5	98.9	100.0	100.0
slp02b	95.2	98.1	100.0	100.0
slp03	97.1	96.3	100.0	100.0
slp16	100.0	-	100.0	100.0
slp32	100.0	-	100.0	100.0
slp41	100.0	-	100.0	100.0
slp59	100.0	-	100.0	100.0
slp60	100.0	-	100.0	100.0
slp66	100.0	-	100.0	100.0
slp67x	97.9	-	100.0	100.0
average	98.7	97.8	100.0	100.0

Table 5-2: QRS detection sensitivity and specificity, proposed method (pm, 1-minute segments) vs literature : MIT/BIH Polysomnographic Dataset – EEG signal.

	Sen (%)		Spe* (%)
Dataset	**Dora** [9]	**PM**	**PM**
ins_2	100.0	100.0	100.0
ins_5	98.9	100.0	100.0
n2	98.7	100.0	100.0
n8	98.4	100.0	100.0
nfle15	98.6	100.0	98.6
nfle35	96.5	100.0	100.0
plm3	96.7	100.0	100.0
plm4	97.0	100.0	100.0
plm9	100.0	100.0	100.0
average	98.5	100.0	99.9

Table 5-3: QRS detection sensitivity and specificity, proposed method (PM, 1-minute segments) vs literature : CAP Sleep Dataset – EEG signal.

We compared our method to Dora and Jiang (popular methods for removing ECG artifacts). The proposed method was tested on these selected subjects to compare our results to what DORA and Jiang got for the same subjects to be sure that we have reference results to compare with.

5.3.3 ECG Component Classifier Performance

This section shows the results of my proposed ECG component classification method on an arbitrary EEG dataset in automatic mode. For the tests, seven subjects were selected at random from a 61-subject 128-channel closed-eye resting-state EEG dataset.

Table *5-4* lists the performance results obtained on the recordings. For subjects s1 and s2, no sensitivity results could be calculated, since no ECG contamination was detectable in the datasets. Correctly, my method did not find any QRS complexes in the components, and consequently none of the independent components were classified as ECG, meaning, that $TP = FP = 0$. For both subjects s1 and s2, no ECG was recognised in the EEG measurements, as the heart effect was so small that it was undetectable.

Dataset	Proposed method		
	QRS detection Sen (%)	Classifier Sen (%)	Classifier Spe (%)
s1	N/A	N/A	100.00
s2	N/A	N/A	100.00
s3	99.11	100.00	100.00
s4	100.00	100.00	100.00
s11	99.61	100.00	100.00
s24	99.40	100.00	100.00
s25	92.81	100.00	99.61
average	98.19	100.00	99.94

Table 5-4: The ECG artifact detection performance of my proposed method on 128-channel resting-state EEG.

5.4 Summary

In this chapter I proposed a fully automatic ECG artifact removal method working without human assistance or reference ECG channel, which can be used in high-throughout, high-speed EEG analysis, continuous monitoring or clinical diagnostic systems. The acquired EEG signals are subjected to independent component analysis and the resulting independent components are examined for cardiac activity characteristics. The applied adaptive threshold-based QRS detector and subsequent rule-based cardiac cycle classifier identify ECG activity and mark component segments for rejection with high reliability.

In QRS detection, the proposed method achieves sensitivity above 99.3% on the PhysioNet datasets (specificity > 99%), higher than all known automatic methods reported in the literature. For our high-density resting state EEG data, the QRS detection sensitivity is above 98.1%, however, the sensitivity of the ECG component classifier is 100%. This is due to the fact that the classifier does not need all the component QRS peaks to identify a component segment as ECG.

The significance of my method is that due to its excellent sensitivity and specificity, it can be used reliably for automatic, unsupervised artifact removal, where similar reported methods might incorrectly remove non-artifacts or leave contaminating components in the dataset.

My method advances the current practice of ECG artifact removal, and due to its clear advantages, i.e. the fully automatic operation, better sensitivity than previous approaches, and the capability of detecting pathological ECG waveforms, such as frequent ventricular ectopic beats or bundle branch blocks, it will help practitioners in producing more accurate analysis results.

6 Functional Connectivity in Ischemic Stroke

As scientific evidence emerged establishing that the operation of the brain is not purely functional (assuming that different parts of the brain are responsible for different well-defined functions) but connectionist (networks of multiple areas execute functions in coordinated cooperation) [139], the focus of research in understanding brain execution mechanisms and brain mapping started to shift from finding individual activated regions to identifying brain networks. When brain imaging and measurement technology advanced the point that it could efficiently support these types of investigations, a new research area, brain connectivity research was born.

As stated in the Introduction, brain connectivity can be divided into three groups as follows:

- *structural connectivity:* tracks the anatomical fibre pathways between different brain regions [140]. Diffusion Tensor Imaging is used to detect these the interconnecting fibre bundles. The patterns of these structural connections are relatively persistent at shorter time scales (hours, days), whereas at a longer time scale (months), these patterns may change due to neuroplasticity.
- *functional connectivity:* is defined as the temporal dependency of the activated neuronal patterns during the flow of information between brain regions. Functional connectivity is based on statistical dependencies between the distant brain regions and can be classified as bivariate or multivariate. The resulting network is represented by undirected graphs.
- *effective connectivity:* is the measure of causality where one neuronal region has a direct or indirect influence on the activity of another region. This type of connectivity is described by directed graphs.

Connectivity research emerged from MRI technology, first aiming to construct and discover structural pathways (connectome) in the human brain. The emergence of high spatial resolution functional (1-3 mm^3) MRI (fMRI) made it possible to conduct functional connectivity studies. These investigations led to the identification of several fundamental resting-state and task-based brain networks [141–143]. Due to technological limitations, however, fMRI functional connectivity analysis is not suitable for the examination of millisecond range changes typically found, for instance, during cognitive task execution [144]. An alternative to fMRI in connectivity studies is EEG technology that provides superior temporal resolution and measures signals generated directly by neurons as opposed to blood oxygenation changes, such as BOLD fMRI.

EEG functional connectivity can be sensor or source based. If statistical dependence is calculated between the electrode signals, we refer to sensor-level (a.k.a sensor-space) connectivity. If the electrode signals are projected to the cortex by solving the inverse problem that identifies the original sources of bioelectric activities and calculated the association among these cortical regions, we refer to source-level (or source-space) connectivity. Source-level connectivity has the potential to achieve higher spatial resolution (the cortex can be partitioned to thousands of potential source areas) but requires accurate 3D anatomical models and solving the ill-posed inverse problem. For these reasons, sensor-level connectivity would be preferable as an experimental method.

The general process of generating a functional connectivity network from EEG measurements is the following. The cleaned, pre-processed signal is input the first stage of the process that establishes associations between electrodes or cortical sources based on a selected association measure described below. The output of this stage is a square association matrix. Each entry of the matrix represents the strength of the connectivity between two electrodes or sources. This matrix is then used as an adjacency matrix, from which various features can be extracted. To reduce the number of edges in the network graph, normally the association matrix is thresholded

and only the top few percent of the edges are kept. The structure of the final connectivity graph can be analyzed by the network features and input to statistical tests.

Functional EEG connectivity has the potential to provide more information than fMRI, due to its higher temporal resolution. Oscillations in the brain regions provide a certain coordination mechanism emerging as synchronized rhythms. These oscillations may transfer information from a local network or region to another region. Examining the flow of information between regions may help to reveal the connectivity relation between the neural assemblies either at rest or during task execution. Connectivity information between the distant brain regions may explain how the neural networks are altered e.g. in stroke or neurodegenerative diseases [145]. It can provide new insights about the large-scale neuronal communication in the brain and may help to understand the origins or track the progress of recovery of stroke or monitor the status of brain diseases such as Alzheimer's disease [146], and predict outcome of treatment to many other deficits related to the brain. In this chapter, I will focus on how EEG-based functional connectivity can be used to describe brain plasticity in stroke, which is the brain's natural ability for re-wiring that is essential for successful recovery from stroke.

6.1 Overview of Connectivity Association Measures

In this section, I briefly overview the various methods that can be used to establish connectivity associations between electrodes or brain regions. Measures for functional connectivity are listed first, followed by ones that can be used for effective connectivity calculations.

6.1.1 Functional Connectivity Association Measures

Functional connectivity is defined as statistical dependencies that exist between sensors or cortical regions [147]. These dependences can be described by bivariate methods such as cross-correlation or covariance, mutual information in time-domain, or coherence [148], and phase differences in the frequency domain.

6.1.1.1 Cross-Correlation

Cross-correlation (CC) is used to measure the linear relationship between the observations of two time series x_1 and x_2 shifted by lags (j) to establish the largest value of the correlation [149].

$$R_{12}(j) = \frac{1}{N}\sum_{n=0}^{N-1} x_1(n)x_2(n+j) \qquad (6.1)$$

where N is the total number of signal samples. In practice, Eq (6.1) is used in its normalized form, which is

$$\rho_{12}(j) = \frac{R_{12}(j)}{\frac{1}{N}[\sum_{n=0}^{N-1} x_1(n) \sum_{n=0}^{N-1} x_2(n)]^{1/2}} \qquad (6.2)$$

Cross-correlation can take up values in the range of -1 to 1 and will show high correlation between the two signals if they are in-phase or anti-phase. Small values around zero indicate that the two signals are almost independent. The advantage of cross-correlation is its simplicity but it presents problems in EEG-based connectivity calculations, since it is based on the signal amplitude, which is sensitive to noise and volume conduction, hence can generate false, spurious

connectivity values. Volume conduction (i.e. the current of a cortical source is measurable at spatially distant scalp electrodes due to the conductance of the brain and skull) represents a serious problem in estimating sensor-level connectivity as it generates false, spurious connectivity between electrodes. Nunez et al., [150] claimed that the volume conduction effect may be reduced by using a high-density caps in which the inter-electrode distance is small. Unfortunately, this does not help in reducing spurious connectivity.

6.1.1.2 Coherence (Magnitude Square Coherence)

Magnitude Square Coherence (MSC) is a bivariate model used to describe the correlation between two signals, x and y, in the frequency domain, and it identifies the significant frequency correlation in terms of magnitude values ranged between 0 to 1. The normalized form of the MSC [128] measures the cross-spectral density S_{xy} with respect to the auto-spectral density of both x, y as shown in the form,

$$Coh_{xy}(f) = \frac{|S_{xy}(f)|^2}{|S_{xx}(f)|S_{yy}(f)|} \quad (6.3)$$

Coherence equation is derived by applying the Fourier Transform (FT) of the correlation equation,

$$S_{xy}(\mathrm{j}) = \frac{1}{N-j}\sum_{n=1}^{N-j}\left(\frac{(x_n - \bar{x})}{\sigma_x}\right)\left(\frac{(y_{n+j} - \bar{y})}{\sigma_y}\right) \quad (6.4)$$

where j is the time lag, σ_x and $\bar{x}$ indicate variance and mean respectively. The coherence depends on the stationarity of the signal, which may be achieved by using the short-time Fourier transform (STFT) for selected data window for which stationarity can be assumed.

Instead of using a fixed window size in STFT that may cause a lack of temporal localisation in low frequencies, Wavelet Coherence (WC) [151] can be used as an alternative approach, which localizes the coupling coherence regions more accurately both in time and frequency. This method is characterized by choosing varying window sizes: the size of the window is changing with the frequencies so, a narrow window is used for high frequencies to achieve good time resolution and larger ones for low frequencies, however the problem of spurious connectivity is present in wavelet coherence as well the [152] [153] [154].

Nolte et al. [155] claimed that discarding the real part of the coherence and using only the imaginary part of the complex coherence (*ImC*) mitigates the spurious interactions related to the field spread mentioned in [156,157]. Phase synchronization (PS) is an alternative approach to the coherence, the nonlinear coupling version is based on the fact that although the two signals may have zero coupling in terms of amplitudes, they may strongly synchronize in phase [158]. In order to reduce the effects of noise and volume conduction, state-of-the-art EEG connectivity methods are all based on phase information.

6.1.1.3 Phase Locking Value (PLV)

Theoretical analyses of amplitude-based connectivity estimators have shown that the accuracy of connectivity estimation can be improved by moving to phase-based connectivity measures [159] [160] as these reduce the spurious effects of the volume conduction and noise [54,161].

Consequently, connectivity methods based on phase synchronization (PS) are the most frequently used in connectivity estimators for EEG signals [162–166]. Under this assumption, two brain regions have similar oscillation properties that said to be related or functionally connected, then, if this coupling between the related regions can be assessed mathematically, then we can obtain phase connectivity.

One of these methods is based on the Phase Locking Value (PLV) [163] that computes the phase difference between observations normalized to all differences between pairs of signals. For all the trials (n = 1,…,N), and for each channel pair, x and y, at time t, PLV is calculated as:

$$PLV_t = \frac{1}{N}\left|\sum_{n=1}^{N} e^{j(\varphi_x(t)-\varphi_y(t))}\right| \quad (6.5)$$

where φ_x and φ_y are the instantaneous-phases of signals *x* and *y* respectively. PLV is used to evaluate the instantaneous phase difference of the signals under the hypothesis that connected regions generate signals whose instantaneous phases evolve together, then we can say the phases of the signals are said to be "locked", and their phase difference is consequently persistent.

Since in practical situations the measured signals contain noise, we cannot be sure that the evaluated signal originates from one cortical oscillator. This issue can be solved by permitting some deviation from the condition of a constant phase difference. Thus, PLV assesses the spread of the distribution of phase differences, and the connectivity assessment is connected to this spread.

Due to the low capacitance of the brain tissue and the small distances that the currents have to travel, the signals of interest are said to have an instantaneous propagation [155,167]. Following from this hypothesis, volume conduction/source leakage effect occurs at two electrodes only if the signals are recorded with zero phase delay. Since the imaginary part of coherency proposed by Nolte et al. [155] and the PLV are both detect zero phased signals, Stam et al. [167] suggested and improved method for the phase lag index (PLI) that can distinguish between 0 and 180 degree phase differences. The introduction of the Weighted Phase Lag Index [168] resulted in a method that is not sensitive to phase/anti-phase signals, hence volume conduction generated spurious connectivity.

$$WPLI_t = \left| < \frac{|\sin(\Delta\varphi_{i,j})|}{\sin(\Delta\varphi_{i,j})} > \right| \quad (6.6)$$

where $\Delta\varphi_{i,j}$ is the phase difference between channel i and j.

In this thesis, I focused on sensor-space functional connectivity. From the association measures discussed above, the PLV and the WPLI measures will be used as these are the least sensitive to signal noise, and minimize spurious connectivity. For the sake of completeness, effective connectivity measures are overviewed next, but these will not be used in the proposed methods.

6.1.2 Effective Connectivity Association Measures

Effective connectivity is defined as directed and dynamically changes according to a certain context or a task executed. Consequently, one of the important aspects of effective connectivity analysis is identifying the directionality of causal effects. If the observation given by the fluctuation of one of the brain regions is able to predict the future fluctuation of another brain region at certain time, then the first region is said to be temporally causing region two and this

gives the main concept where Granger causality (GC) is established [169]. For two variables X_1 and X_2, the GC formula if X_2 causes X_1 is given by

$$X_1(t) = \sum_{j=1}^{p} A_{11,j} X_1(t-j) + \sum_{j=1}^{p} A_{12,j} X_2(t-j) + E_1(t) \quad (6.7)$$

where p is the model order and A is coefficients matrix.

Zhou et al. [170] proposed a combination of PCA and GC for studying the direct influences between functional brain regions within fMRI measurements. PCA method was used for dimensionality reduction to select some principal components from fMRI time-series that were used later as input to identify the effective connectivity. Although these approaches do not involve temporal aspects, another method based on dynamic Bayesian networks (DBNs), was used to estimate the EC between the activated brain regions from fMRI data sets [171]. Despite of the potential usefulness of the principle of effective connectivity, it remains a source of concern and ongoing arguments, mainly because of the temporal blurring caused by the hemodynamical response. The most popular methods used to estimate the EC are Directed Transfer Function (DTF) and Partial Directed Coherence (PDC) described in the following subsection.

6.1.2.1 Directed Transfer Function (DTF)

The Directed Transfer Function [172] used the GC concept to determine the coherence direction between a pair of signals in a full multivariate spectral dataset. Kaminski et al. [160] claimed that DTF is not influenced by brain volume conduction, so it is unnecessary to use a Laplace transform (LP) or cortical projection that causes in some cases destroying in the connection structure of the original signal. Brunner et al. [173] contradicted the results given by Kaminski and gave a simulation example which proved that the DTF method was effected by volume conduction. DTF can be computed by the multivariate autoregressive model (MVAR) that is given by:

$$X(t) = \sum_{m=1}^{p} A(m) X(t-m) + E(t) \quad (6.8)$$

where $X(t)$ refers to vector data of length (t=1: number of channels(k)), E(t) is a vector of uncorrelated white noise, p is the fitted model order, and A(m) are coefficient matrices of dimension $k * k$. Equation 6.8 tends to the frequency domain to give the DTF by the form:

$$\gamma^2_{ij}(f) = \frac{|H_{ij}(f)|^2}{\sum_{m=1}^{k} |H_{im}(f)|^2}, \quad (6.9)$$

which describes the flow of information at frequency f from channel j to channel i with respect to all channels (k).

6.1.2.2 Partial Directed Coherence (PDC)

PDC [174], is a GC modification used to describe the directed out flows between n time series $\boldsymbol{x}(t) = [x_1(t), \ldots, x_n(t)]^T$. PDC is given thought the normalization form as shown in the following equation,

$$PDC_{ij} = \frac{A_{ij}(f)}{\sqrt{a_j^*(f)a_j(f)}} \quad (6.10)$$

where $A_{ij}(f)$ are the Fourier Transform of the MVAR coefficients, $a_j(f), j = 1,2 \ldots, n$ represent the columns of $A(f)$, and a_j^* is the transpose and complex conjugate of a. Unlike the DTF, PDC is normalized regarded to the channel that sends the signal and it shows the ratio between the outflows from channel j to i with respect to all outflows from j to other channels. This underlines partly the sinks, not the sources, which smears the absolute strength of the coupling [175].

6.2 Overview of Connectivity Network Metrics

Once the association matrix is established for the cortical regions of EEG electrodes, a graph can be constructed to describe and visualise the connectivity structure. In the graph, connectivity is represented as edges connecting cortical areas or sensors. If a binary graph is used, the association values must be thresholded and turned to 0, 1 values depending on whether the value is below or above the threshold. In the weighted graph case, edges will represent association weights, hence the thresholding step can be ignored.

Rubinov et al., described the brain connectivity networks by graphs, consisting of nodes (brain regions) and edges (connections) [61]. Nodes ideally should represent coherent structural or functional brain regions without spatial overlap. It provides a clear analysis to and insight towards the topological network's changes over time. It presents the modularity approach which allows dividing the main network into subnetworks of different modules. EEG measurements can be problematic in this sense, since EEG electrode locations may not be aligned with the boundaries of regions. In addition, because of volume conduction, electrodes may detect spatially overlapping signals. One solution to the latter problem is to compute functional connectivity networks on the cortex instead of the scalp using spatial deconvolution [176]. Links represent anatomical, functional, or effective connections (link type) but can also have weight and direction associated with them. Binary links only represent the presence or absence of a connection. Weighted links, on the other hand, can represent various properties. In anatomical networks, weights may represent the size, density, or coherence of anatomical tracts, while weights in functional and effective networks may represent respective magnitudes of correlational or causal interactions. In functional and effective connectivity networks, links with low weights may represent spurious connections that obscure the topology of strong connections. These can be filtered out using suitable thresholding policies.

Brain network can be identified by using a variety of measures such as calculating the modularity of the different nodes-electrodes in the network, which tracks the extent of community structure of the network [198]. Other measures could be used to identify the network flexibility, how many times the regions of the brain switch from one node or module to another over time [199].

Graph theory provides the necessary tools to characterise the structure of these networks in an efficient way. We can investigate whether the resulting network is optimal in terms of segregation and integration (Figure *6-1*) determine the complexity of the networks developing and how they respond to different kind of damages, e.g. stroke. A large set of network metrics has been identified that can be used in the analysis of the connectivity networks [61]. In the followings, I describe the most important metrics.

a) **Degree**

Degree is the number of connected links of a node *i* and is defined as

$$d_i = \sum_{j \in N} a_{ij} \quad (6.11)$$

where a_{ij} edge connecting node *i* and *j* in a set of *N* nodes.

b) **Local and Global Efficiency**

The efficiency [177] of a network describes how efficiently it exchanges information. Global efficiency measures the amount of information that can be exchanged across the whole network, while a network's resistance to failure on a small scale is given by the local-efficiency (LE). Thus, for node i the LE characterizes how well information is exchanged by its neighbours when this node is erased. Global efficiency (GE) is the functional integration of the network (the average inverse of shortest path length in the network), and is calculated by:

$$E = \frac{1}{n} \sum_{i \in N} \frac{\sum_{j \in N, j \neq i} \left(d_{ij}^{w}\right)^{-1}}{n-1} \quad (6.12)$$

where d_{ij} is the characteristic path length (Shortest path length, between nodes i and j).

c) **Betweenness Centrality**

Betweenness Centrality (BC) [178] is defined as the fraction of all shortest paths in the network that comprise a given node *i*. It is a measure which can characterize the degree to which nodes stand between each other and is shown in the following formula:

$$b_i = \frac{1}{(n-1)(n-2)} \sum_{\substack{h,j \in N \\ h \neq j, h \neq i, i \neq j}} \frac{\rho_{hj}(i)}{\rho_{hj}} \quad (6.13)$$

where ρ_{hj} is the number of shortest paths between nodes *h* and *j*, and $\rho_{hj}(i)$ is the number of shortest paths between *h* and *j* that pass-through node *i*. For example, the higher the information passes to the node the higher the betweenness centrality of the node.

d) **Modularity**

Modularity [179] is one indicator of network structure or graphs. It was conceived to quantify the strength of a network's division into modules (also called classes, clusters or communities). High-modularity networks have dense node connections within modules but sparse node connections in separate modules. Modularity is also used to identify group structure in networks in optimisation methods.

$$Q = \sum\nolimits_{u \in M} \left[e_{uu} - \left(\sum_{v \in M} e_{uv} \right)^2 \right] \quad (6.14)$$

where the network is fully segmented into a set of non-overlapping modules M, and $e_{uv}$is the proportion of all links that link nodes in module u with nodes in module v.

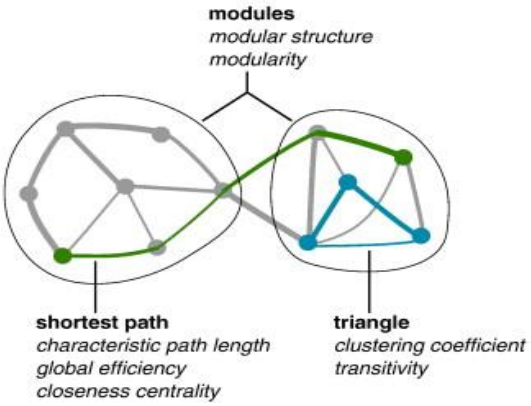

Figure 6-1: Modules Structure [61].

e) **Characteristic path length**

The characteristic path length L of a graph G is defined as the average number of edges in the shortest paths between all vertex pairs and is considered the most commonly used measure of functional integration [61]. It can be given by:

$$L = \frac{1}{n}\sum_{i\epsilon N} L_i = \frac{1}{n}\sum_{i\epsilon N} \frac{\sum_{j\epsilon N\, i\neq j} d_{ij}}{n-1} \tag{6.15}$$

f) **Assortativity**

In the weighted network where the node has weight values not binary value, assortativity is a correlation coefficient between the strengths (weighted degrees) of all nodes on two opposite ends of a link. The positive value of the coefficients shows that nodes are linked with other nodes having the same strength.

6.3 Functional Connectivity Biomarkers for Monitoring Ischemic Stroke Recovery

Ischemic stroke is considered one of the major causes of either death or permanent disability with increasing frequency of occurrence as the population in developed countries is aging. The resulting neurological deficits caused by stroke have a huge impact on the patients' daily activity, quality of life, as well as on healthcare costs [180]. A number of brain regions could have deficits after stroke such as, hemiparesis [181], and functional disability that happens through the motor system [182,183]. Prompt and effective treatment can help in speeding up the recovery and improve rehabilitation outcome. To track the rehabilitation process, a complete insight about the mechanisms would need to underlie neurological deficits and the recovery. This helps to design novel interventional approaches and suggest the appropriate treatments needed for the recovery.

Identifying bio markers of brain networks, could help in enhancing therapeutic impact by informing individualization of the scope, timing and length of therapy [184]. These bio markers include measurements of function and structure in white matter and gray matter. White matter integrity or lesion load tests were found to correlate with motor dysfunction in chronic hemiparetic stroke patients [185,186], while increasing in motor status function have been associated with increasing activity in secondary sensorimotor regions [187].

The usual timeline of treatment for stroke starts with an MRI and/or CT scan to identify the location and extent of brain damage. The underlying stroke deficits are usually caused by focal brain lesions, for example in aphasia [188]. Diagnosis by imaging is complemented by clinical evaluations using standardized stroke scales such as the National Institutes of Health Stroke Scale (NIHSS) [22,23], the Fugl-Meyer Assessment for Upper Extremity (FM-UE), the Nine Hole Peg Test (NHPT), etc.) [22,23,189,190]. Once the diagnosis is established, treatment starts and the condition of the patient is monitored by the medical staff based on patient status. To confirm the level of recovery at patient dispatch from hospital, a second MRI scan might be performed.

Peter et al. [191] have investigated the impact of the lesioned hemisphere of stroke patients using fMRI-based functional connectivity. Three groups of 14 healthy controls, 14 stroke survivors with left hemisphere lesion and other 14 stroke survivors with right hemisphere lesion were examined during the resting state. The brain was devised into four regions, two on the left and two on the right and they extracted the functional connectivity from the primary (S1) and secondary (S2) somatosensory cortical areas. The group with lesion in the left hemisphere showed lower FC compared to the control group, from left S1 to S2 in the right side of the brain. Inter-hemispheric FC in healthy controls was higher than in the stroke group in both regions S1 and S2. The lesion hemisphere was associated with various patterns of altered functional connectivity within the somatosensory network and was associated with various patterns of altered functional connectivity within the somatosensory network and related functional networks.

A resting-state functional magnetic resonance imaging experiment was performed on a group of 37 stroke patients to predict the functional outcome after acute stroke [192]. The correlation coefficient for each pair of brain regions was calculated at 3 and 90 days after the stroke onset. Graph analysis was used between regions of interest to detect the changes in FC between patients. The results showed that higher FC is related to patients with better outcome.

Researchers examined whether the default mode network function in stroke patients is decreased compared with healthy control subjects in resting state condition [193]. Brain network properties of 21 control subjects and 20 first-ever stroke patients were examined during resting state functional MRI. Independent Component Analysis was applied to the recorded datasets to detect the default mode network between the control and the stroke group. Correlation coefficient matrices were calculated from each group, and FC of the regions of interest was explored. Two-sample t-test was applied to identify the significant differences between the two groups. Power spectrum density was calculated for each subject and the average power spectrum was calculated for each group. The results did not show significant differences in the frequency between the two groups, however, there was a reduction in the FC in the stroke regions.

The efficiency of the treatment is difficult to evaluate without monitoring quantitative stroke metrics since the stroke deficit can develop in the hospital in short time, for example, Delayed Cerebral Ischemia (DCI), which can only be discovered once symptoms worsen [24]. The normal tracking protocol for neurological deficits is to localise the lesion with imaging methods and monitor the deficits developing with time. An experiment was performed after stroke to show brain recovery from neurological deficits, and dynamic variations was located in areas near to per-lesioned areas[194]. They claimed that the recovery can arise from reorganization of preserved perilesional regions to the functions previously assumed by the damaged tissue [195].

The continued monitoring of mechanisms underlying stroke deficits is very important, since it could be calculated though tracking the metrics of the network representing stroke deficits without the need to a sophisticated protocol. The simplicity of these metrics could help in

selecting the best treatment path, and be used as predictors for the level of recovery at the end of the rehabilitation period [25–28].

The limitation of the published studies are that the biomarkers are extracted from fMRI-based measurements which result in low temporal resolution, high cost of measurement and increased inconvenience for patients. Some of the studies [193] focused on comparing biomarkers between stroke and normal groups, and did not include monitoring the course of recovery for stroke measurements. We are proposing quantitative metrics and connectivity pattern analysis for brain networks based on EEG measurements that are easy to obtain, technically reliable and provide useful predictive parameters. The introduced biomarkers may provide greater insight to the rewiring and plasticity of the brain after acute stroke, and could improve patient monitoring and therapeutic interventions.

In the remaining of this chapter, I examine the use of high-resolution EEG technology as an aid for monitoring and quantifying patient recovery progress, complementing the use of clinical stroke scales. Reliable biomarkers are introduced that characterize progress of recovery and track the outcome. The simplicity of resting state EEG analysis is that measurements can be performed quickly without moving the patients; it does not require task execution and can be repeated daily for effective progress monitoring.

6.3.1 Subject and Methods

The use of the time-frequency quantitative metrics have already been suggested [28–31] for accurate monitoring of patients. These metrics can monitor the stroke related deficits and track neurological changes well before symptoms develop [28]. The reported methods all rely on the calculation of one or two metrics from measurements using low-density 19-electrode clinical EEG systems. In this section, I propose the use of connectivity network metrics as biomarkers based on high-density, 128-channel EEG measurements. A topographical mapping of the metrics is used to show the location and extent of the stroke area. This representation also facilitates measurement of change as an indicator of the speed of recovery and outcome.

Graph connectivity metrics were introduced for resting state connectivity measures collected from control subjects and stroke patients. Graphs were generated from the connectivity matrices for quantitative analysis and visualization purposes. The structure and properties of the brain connectivity networks were compared for healthy subjects and stroke patients. In the case of stroke patients, networks from the beginning and end of the rehabilitation period were compared as well. The diversity of the connectivity graphs reflects the difference between the healthy and patient resting-state behaviour. The sub-networks around the stroke lesion were explored and compared to the left or right unaffected hemisphere to detect the hubs, patterns, and measure density and the recruitment of brain regions [61]. These patterns show the network structure on the stroke-affected hemisphere and other unaffected areas.

Twenty-seven healthy volunteers (males, aged 16-19) were used as a control group. Eleven ischemic stroke patients were selected with different lesion location and stroke severity for analysis. All volunteers and patients gave their written consent for participating in the experiments. The measurement details of the stroke patients are listed in Table 6-1.

patient	age	stroke location	First measurement (days)	Second measurement (days)	NIHSS 1st/2nd	FM-UE 1st/2nd	NHPT 1st/2nd (sec)
1	48	35x45 jobb temporoparietalis	8	91	2/1	64/66	NHPT: 83/28
2	50	j. lacunaris	8	103	1/0	65/65	NHPT: 42/27
3	63	Small left subcortical lacunar infarct	8	99	2/0	58/65	NHPT: 42/27
4	64	20x20 right frontal	12	100	1/0	61/65	NHPT: 326/97
5	65	right parietal 15x13	9	100	5/2	40/57	NHPT: failed/117
6	65	17x10x23 left caudatus, frontal capsula	7	84	1/0	64/66	NHPT: 31/27
7	66	22x40 left occipital	5	84	2/1	64/65	NHPT: 41/29
8	67	36x25 right frontal	15	100	3/1	60/65	NHPT: 57/41
9	67	48x24x33 left caps. Putamen	15	107	4/1	54/63	NHPT:162/34.5
10	70	56x51 right parietal	22	104	2/2	44/48	NHPT:failed/failed
11	77	20x13 right frontal under M1	12	98	1/0	51/64	NHPT: 3 pegs in 2 minutes/56.5

Table 6-1: Summary information of stroke patients. NIHSS scale: 0-42, the lower the better; FM-UE scale: 0-66, the higher the better; NHPT: the shorter the time the better.

6.3.1.1 EEG Measurement

Three-minute resting state EEG with closed and open eyes were recorded for each participant. During the experiment, subjects had to sit in a relaxed position in a silent room. For stroke patients, two measurements were performed. The first measurement was performed 5-20 days after the stroke onset while the second measurement took place 90-100 days after the onset. All measurements were carried out using a Biosemi ActiveTwo EEG system (f_s = 2048 Hz) with a high-density 128-channel ABC radial layout electrode cap. Data were recorded and made available for the analysis by the National Institute of Neurosurgery, Budapest. All healthy volunteers and stroke patients gave their written consent to participation in the study and allowed the measurements to be used for research purposes. The measurements were approved by the Ethical Committee of the National Institute of Neurosurgery.

6.3.1.2 Data Pre-processing

Each dataset was filtered with a 1–47 Hz 4th-order zero-phase Butterworth bandpass filter to remove the DC component, slow drifts, line noise and unwanted high-frequency components. EEG frequency of interest is located in these bands band (Delta 1-4 Hz, Theta 4-8 Hz, Alpha 8-12 Hz, Beta 12-30 Hz, Gamma 30-45 Hz), [116]. The selected frequency band avoids the appearance of the power line noise 50 and 60 Hz. Also, it is known that alpha frequency activity decreases in stroke patients, while low frequency, especially delta band, increases. The data sets were re-referenced to the average of the signals, then down sampled to f_s = 256 Hz in order to reduce the execution time of the subsequent Independent Component Analysis. The filtered signals were partitioned into 10-second non-overlapping consecutive segments. The Infomax ICA algorithm [76] was performed on each segment to identify artifact components. EOG and ECG components were identified and rejected using the methods introduced in Chapter 4 and 5 to generate an artifact-free dataset. All analyses were carried out in the Fieldtrip toolbox [19] using custom scripts.

6.3.1.3 Functional Connectivity Calculation

The connectivity matrix of each data set was calculated using the debiased weighted Phase Lag Index (*dwPLI*) [196] that measures the phase relationships between the nodes of the functional brain networks. The advantage of this method over other correlation-based methods is that it is not influenced by volume conduction, spurious connections and robust against the uncorrelated noise [197]. The *dwPLI* connectivity matrices were computed for each participant for four different frequency bands – delta (1- 4 Hz), theta (4-8 Hz), alpha (8-12 Hz), beta (12-30 Hz) – then thresholded to keep only the strongest 10% of the edges. All connectivity measures were calculated using the Brain Connectivity Toolbox [61] as described in [145,197,198]. The connectivity measures of the 27 healthy subjects were averaged to create control graphs for comparisons. Particular interests were in metrics that characterize network segregation and integration, such as the clustering coefficient of each node (a measure of its local connectivity), the global efficiency which reflects the importance of the node in the shortest paths and the degree distribution. For the analysis in this work, I selected four stroke patients, whose change in status by the end of the three months were the largest.

6.4 Results

Several brain metrics were calculated and analysed for the healthy subjects and the stroke patients to find significant differences in the connectivity networks and to check the level of recovery by comparing the first and second stroke measurements with the control group. Figure 6-2 shows the MRI scan of stroke patient 1 identifying the location of the stroke lesion of. This image can be used as a reference in studying the resting state connectivity graphs.

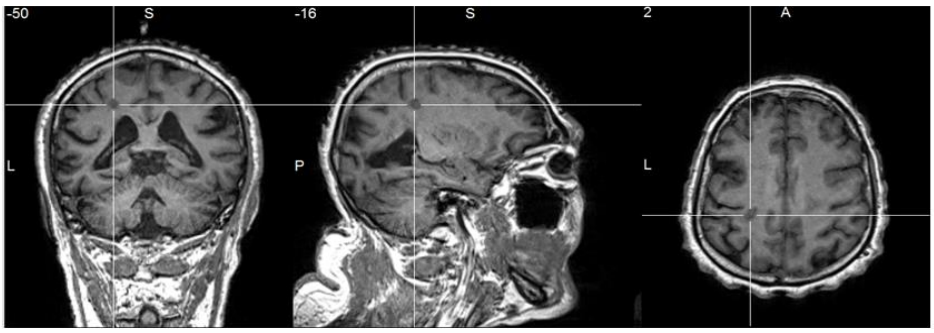

Figure 6-2: MRI scan of Patient 1 with crosshair indicating the stroke lesion.

Connectivity graphs for the delta, theta, alpha and beta frequency bands were generated from the healthy as well as from the first and second stroke measurements. The healthy connectivity graph is shown in Figure 6-3, the stroke connectivity graphs are in Figure 6-4. In the connectivity plots, nodes represent the electrodes whereas lines indicate pairwise functional connections. Only the strongest 10% of the links were retained.

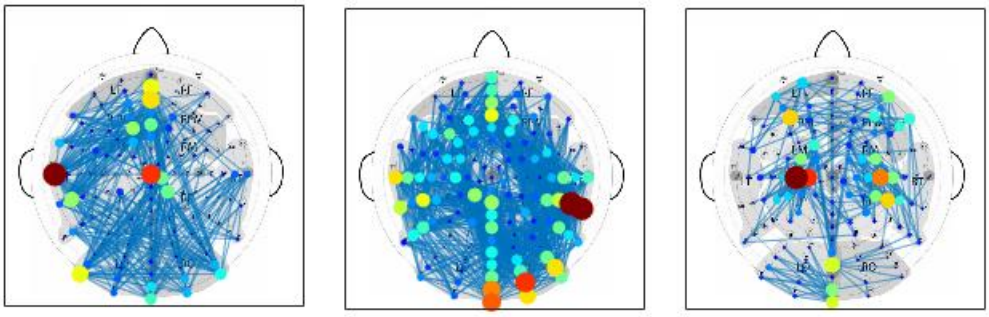

Figure 6-3: Connectivity graph of a control subject (theta, alpha and beta bands). The colour and the size of the nodes represent the strength of the connection and the degree, respectively.

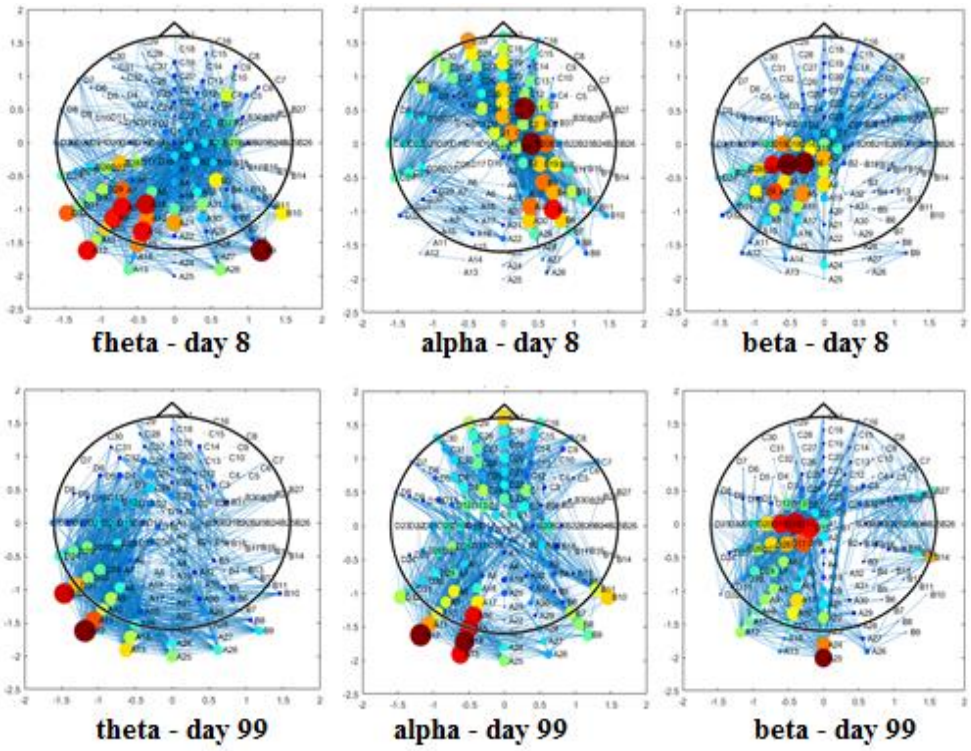

Figure 6-4: Theta, alpha and beta band connectivity graphs of first (top row) and second measurements (bottom row). The colour and the size of the nodes represent the strength of the connection and the degree, respectively.

The distribution of the node degrees of the connectivity graph of the three measurements are shown in Figure 6-5. The first stroke measurement group shows an average nodes degree around 60 (red line), while the average node degrees for the same group second-measurement reduces to 45 degrees similar to the normal group as shown in Figure 6-5. The Normal and the second stroke measurement group show very similar node degree distribution unlike the first measurement which has degrees in the range of 45 to 70. This result shows how the stroke patients recovered, i.e. converged to healthy connectivity network by approx.. 88 days after the stroke injury.

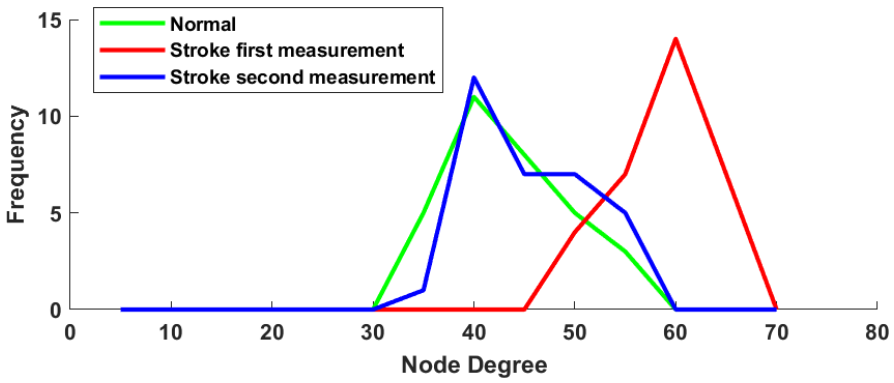

Figure 6-5: Histograms of node degrees of the normal group and of stroke patients at the first and second measurement.

Figure 6-6 shows box plots of the normal and stroke first (a)/second measurement (b) for delta to beta bands. The node degree of the first stroke measurement is greater than the normal group, but in the second measurement, both of the two groups has almost the same level of node degrees at theta and alpha bands. The numbers are shown at each boxplot are P values represent the level of statistical significant t-test of 95 % confidence interval between each group at each frequency band. The stats show significant between the normal/ stroke first measurements for delta, theta and alpha bands, and by testing the normal group with the second stroke measurements group, the level of significant reduced at all bands while no significant was shown at alpha band, which confirm the recovery of the stroke patient at 88 days from the injury.

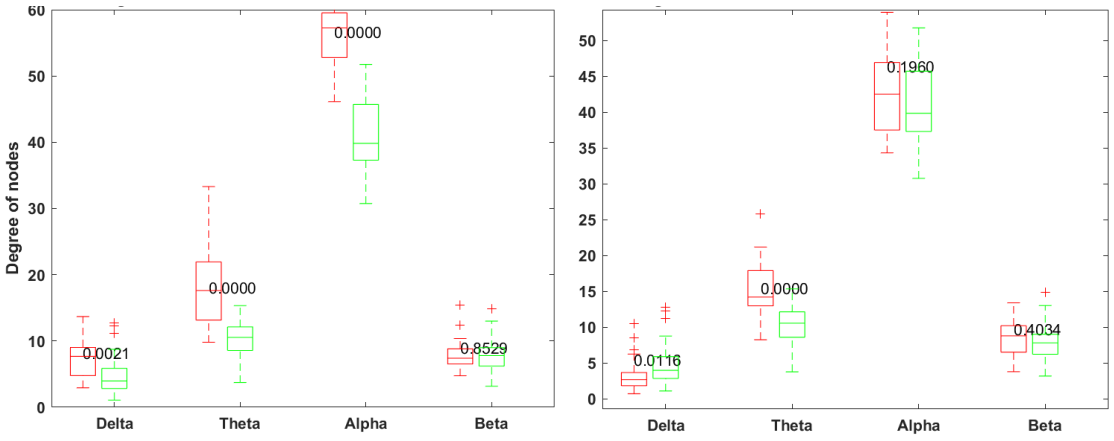

(a) (b)

Figure 6-6: Boxplots of node degrees (a) for the first stroke measurement (red boxes) and normal group, and (b) for the second stroke measurement (red boxes) vs. the normal group.

Figure 6-7 shows the edge betweenness metric which measures the importance of the edge where it is given by the fraction of all shortest paths in the network that contain a given edge. Edge with high level of betweenness centrality participates in a large number of shortest paths. Figure 6-7 on the left side shows a large difference of edge betweenness between the first stroke measurement and the normal group at theta and beta bands, but on the right side, similar values are obtained in all bands for the second stroke measurement stroke and the normal group.

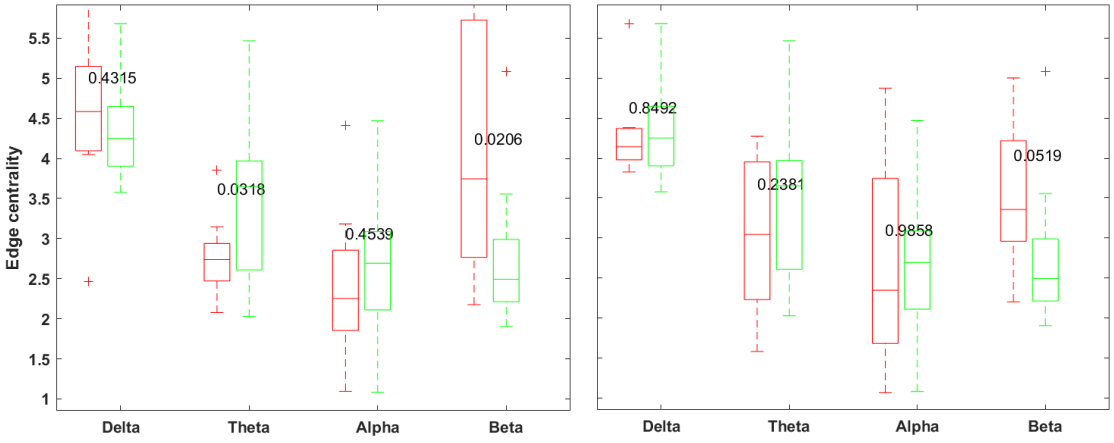

(a) (b)

Figure 6-7: Boxplots of edge betweenness centrality for the first stroke measurement (red boxes) and normal group (a), and (b) is the edge betweenness centrality for the second stroke measurement (red boxes) vs. the normal group.

The local efficiency of the left motor area was calculated as region of interest as shown in Figure 6-8. The level of significance reduced from first to second measurement at delta, theta and alpha band, but no significant difference was noticed at beta bands.

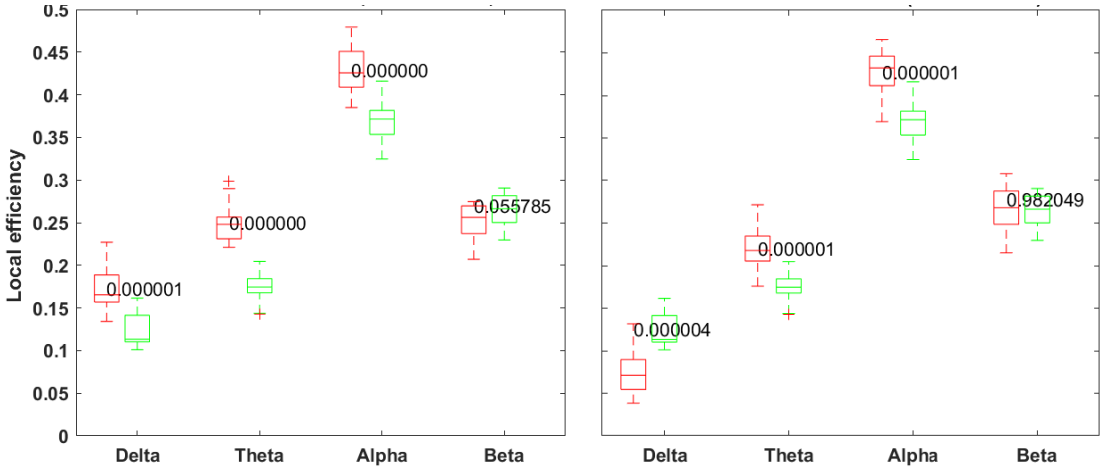

(a) (b)

Figure 6-8: Boxplots of Local Efficiency (LE) of the left motor area for the first stroke measurement (red boxes) and normal group (a), and (b) is LE for the second stroke measurement (red boxes) vs the normal group.

The small-world property is given by the ratio between the characteristic path length and the mean clustering coefficient. The small-world metric is given by the ratio between the characteristic path length and mean clustering coefficient. Small-world networks are known for their efficiency in that they enable a rapid integration of information from local, specialized brain areas even when they are distant [199]. In case of the normal subject the network gives higher small world values than the stroke subject since the normal subject' networks generate characteristic path length larger than the stroke patient because the distant networks in the normal subject can be integrated better than the stroke subject, e.g. networks of the normal subject are less segregated. Vertical dashed line in Figure 6-9 is for Delta to Gamma bands, and x axis refers to the threshold from 5 to 25 % of total connections.

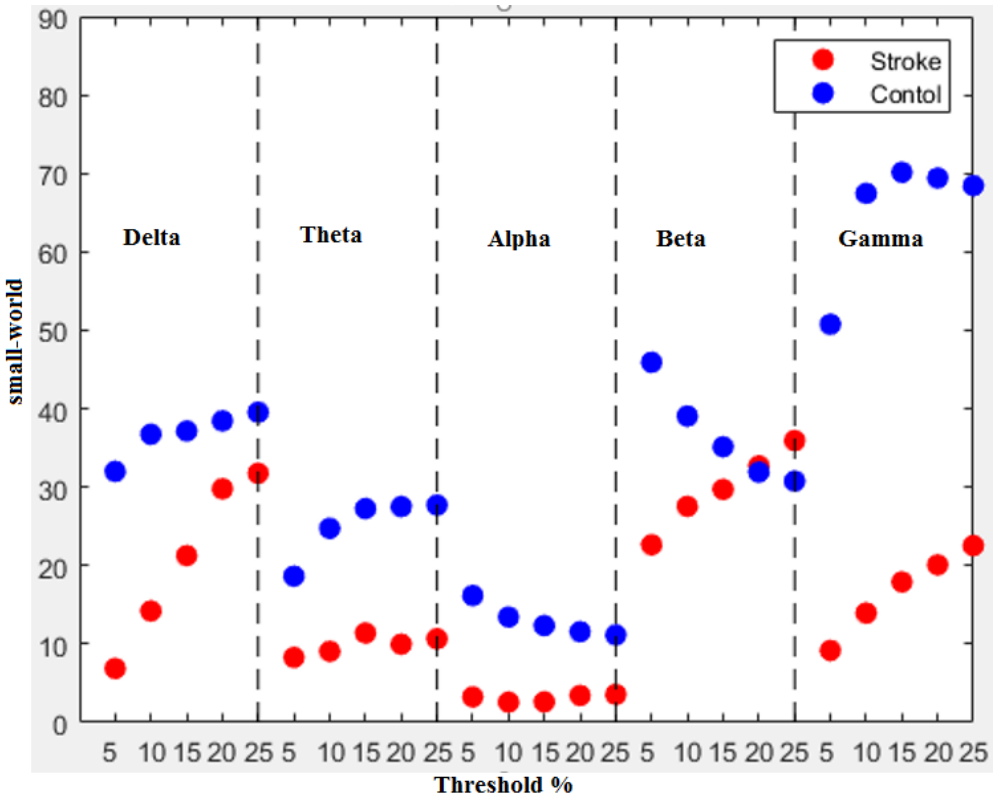

Figure 6-9: The small-world metric is given by the ratio between the characteristic path length and mean clustering coefficient, Vertical dashed line is for Delta to Gamma bands, and x axis refers to the threshold from 5 to 25 % of total connections.

6.5 Summary

It is well known that delta power increases while alpha power decreases in stroke-affected patients. Delta increase is coupled with a decrease of blood flow, while higher frequency alpha decrease is contributed to neural tissue death. Similar phenomena can be identified on the connectivity graphs. In the first measurements (few days after stroke onset) there is increase in connection strengths and node degree in the delta band. The stroke area is clearly unconnected in the alpha band indicating reduced activity. At the same time, alpha connectivity decreases on the unaffected hemisphere, and node degree increases in middle areas. In contrast, beta connectivity is increased over the stroke area, whose explanation is still sought for. The second measurement graph shows that theta and alpha bands return to near normal connectivity. Beta band is peculiar again as the highest connectivity increase moved to the sensor-motor area. The second stroke measurement shows node degree distribution similar to the normal group which indicates that the connectivity structure of the stroke-disturbed brain recovered close to normal within three months. Statistically significant differences were detected by t-test between the normal group with the first and second stroke measurements. Node degree, edge betweenness and local efficiency metrics show significant differences at different frequency bands between the normal group and the first stroke measurement, but the significance level is gradually reduced at some bands and vanished at others in the second stroke measurement which confirms that the rewiring of brain networks tend to be normal. These measures seem as potential biomarkers for stroke characterisation, and the results indicate the usefulness of functional connectivity for assessing stroke and predicting outcome of recovery.

7 High-Resolution Dynamic Functional Connectivity

This chapter investigates dynamic functional connectivity (DFC) and proposes a method for detecting fast temporal fluctuations in brain activity networks based on Ensemble Empirical Mode Decomposition. A large body of earlier research has established the spatial characteristics of neural connectivity [161,200] and for decades, functional connectivity computations relied on the assumption that the signals under investigation are stationary [201,202].

The brain generates activations that oscillate rapidly [203], consequently connectivity related to sensory and cognitive tasks would also change rapidly. The question is then, how and when the brain activation and connectivity among different brain regions propagate throughout the execution of a task. A change in the field of functional neuroimaging has been motivated by the concept that coordinated temporal patterns between specific neural regions send information above and beyond the independent behavior of these regions-groups. Investigation into the activation caused in certain regions by some stimulus or task-related has, in part, given way to analysis of patterns of co-activation or functional connectivity between distal regions, contradicting with the old theory where the stationarity of connectivity cannot be assumed [204].

The functional connectivity community has been looking beyond the stationary assumptions on which earlier research was based and has proposed approaches for integrating temporal dynamics in connectivity analysis. Since the most important goal of neuroscience, is to better understand how brain networks are integrated and dissolved in order to support continuing cognitive functions, accurate characterization of the dynamism of connectivity networks is of paramount importance [144,205,206]. Tracking the dynamics of fast activity changes, i.e. uncovering spectral variations in non-stationary signals, presents great challenges and has been a long-standing research problem.

The most commonly used method is that of a windowed analysis in which the signal is divided into windows of fixed duration and the connectivity is calculated in each window. Windowed connectivity originated from fMRI analysis. In a study performed by Maria et al., using fMRI measurements to identify the dynamics of functional connectivity [206], connectivity calculations were performed on selected time windows of length 30 seconds. Such a long-time window may be suitable for resting-state investigations but are not suitable for detecting task-related dynamism in the connectivity network. These time limitations generate doubt whether we can trust the results, whether the generated connectivity is related to true coupling or just due to random noise [207]. Although EEG has very high temporal resolution in terms of milliseconds, functional connectivity interactions are still identified by using trivial spatiotemporal patterns, defined in a static sense, i.e. the connectivity is analysed at large time scales using data windows of several seconds [208]. While this may reflect part of the connectivity, it cannot show a clear image of the dynamical connectivity changes that happened at millisecond scale [209].

True dynamic connectivity is vital if we are to explain the nature of how cognitive networks are generated. As an example, time-locked oscillatory reactions to stimulus in normal cases occur in the range of few hundred milliseconds after the stimulus. These reactions could be significant events, such as, e.g., right finger press, left finger press [201,202]. The main problem with the static approaches and very long-time windows that the results cannot reflect the true coupling that happened in the brain over this short time period.

The most important issue in time-frequency analysis is the principle of uncertainty, which stipulates that one cannot localize a signal with absolute precision both in time and frequency.

Long windows are needed for lower frequencies that provide good frequency but reduced temporal resolution, while short windows used for higher frequencies result in better time but lower frequency resolution [33,34]. Over the past 30 years research to non-stationary signals increasingly has grown resulting in a body of work called "time-frequency" (TF) methods. This included linear TF methods such as the Short Time Fourier Transform (STFT), Wavelet Transform (WT) that involve phase and magnitudes contributions, and non-linear methods that lead to real-valued transforms. STFT, the extension of FT, was modified to show nonstationary characteristics of the signal in the time-frequency domain. It consists of the successive FFT of the overlapped windowed signal, where each frequency distribution being correlated with each window's central time. The main drawback of the method that it has a smeared peak around the peak of the main frequency with decaying side lobes on the selected window. However, side lobes attenuation is associated with increasing of the window [32]. The spectral smearing can be reduced by increasing the length of the time window, but this also reduces the time localization by imposing increased stationarity. Thus, high time localization comes at the expense of the spectral smearing.

Using the Hilbert transform as a means to compute instantaneous frequency, promised better results, but the Hilbert transform breaks down for multicomponent, broadband EEG signals [210]. As an improvement, the Hilbert-Huang transform based on Empirical Mode Decomposition (EMD) and Hilbert Spectral Analysis have been recommended [210,211]. While used successfully in EEG studies [212,213] EMD has been criticized for being sensitive for noise and prone to mode mixing. Improvements, such as Ensemble Empirical Mode Decomposition [214] reduced noise sensitivity and mode mixing, while the CEEMDAN method [215,216] further reduced spurious modes and component noise, and provided completeness, i.e. the recoverability of signals from its immediate mode functions.

In this chapter section, I discuss the problems of increasing the temporal resolution of functional connectivity and go through a collection of used tools that have been developed to give possible solutions then show how my proposed method can uncover fast-changing connectivity patterns in a finger-tapping task.

7.1 A Critique of the Sliding-Window Dynamic Connectivity

The simplest analytical strategy to explore Dynamic Functional Connectivity (DFC) can be calculated by dividing the time-course of the measured signal into time windows say 100 ms or more, then the connectivity method (correlation, or coherence) are applied to each window. It has been widely used in EEG to represent the connectivity between regions or electrodes [144,177,217]. By measuring FC over subsequent windows, it became possible to recognize connectivity variations, which is why the term dynamic FC became coined. The sliding window can be called static or dynamic based on the way in which it can be calculated. For example, if the functional connectivity for the entire experiment is collected from one time window, then this approach is called static, otherwise if divides the time-course of the signals into window slides over time propagation and connectivity is calculated with these overlapped time windows, then this approach is called dynamic. Figure 7-1, presents an example for the sliding time window. It shows two signals are propagated form time 0 to 1000 ms. The two signals are divided into time windows of length d=200 ms moving with timesteps k=50 ms. The first window starts at 0 to 200ms, and with the moving step, the second window starts at 50ms and end at 250ms and so on, and the process is repeated so that we can generate a time course of connectivity as illustrated in Figure *7-1*. The top panel shows the two generated signals, and red dashed rectangle is located

around the selected time window of length d. The black arrow to the right refers to the direction where the time window slides while the function connectivity is calculated at each moving step. The bottom panel shows the connectivity results for each window, where the red cross refers to the centre of the time window along which the connectivity is calculated. Connectivity values start form 0 referring to no coupling and end with value 1 when the two signals are strongly correlated.

Besides the simplicity of the calculations based on sliding window approach, it suffers from limitations, for example, the selected time window 200 ms could not represent the fast-dynamic changes in the network and could not reflect the true coupling and consequently gives some doubt about the generated results. The second issue is the length of the selected time window; no certain criteria could decide the proper time window in which the coupling of the signals in time-frequency variations would be well represented. Too long window [218] impedes the identification of temporal variations while, too short window lengths means few samples for a reliable calculation which introduces spurious fluctuations in the observed DFC [144,219]. A trade-off between the length of the time window would come in the expense of the frequency calculations as shown in the next example.

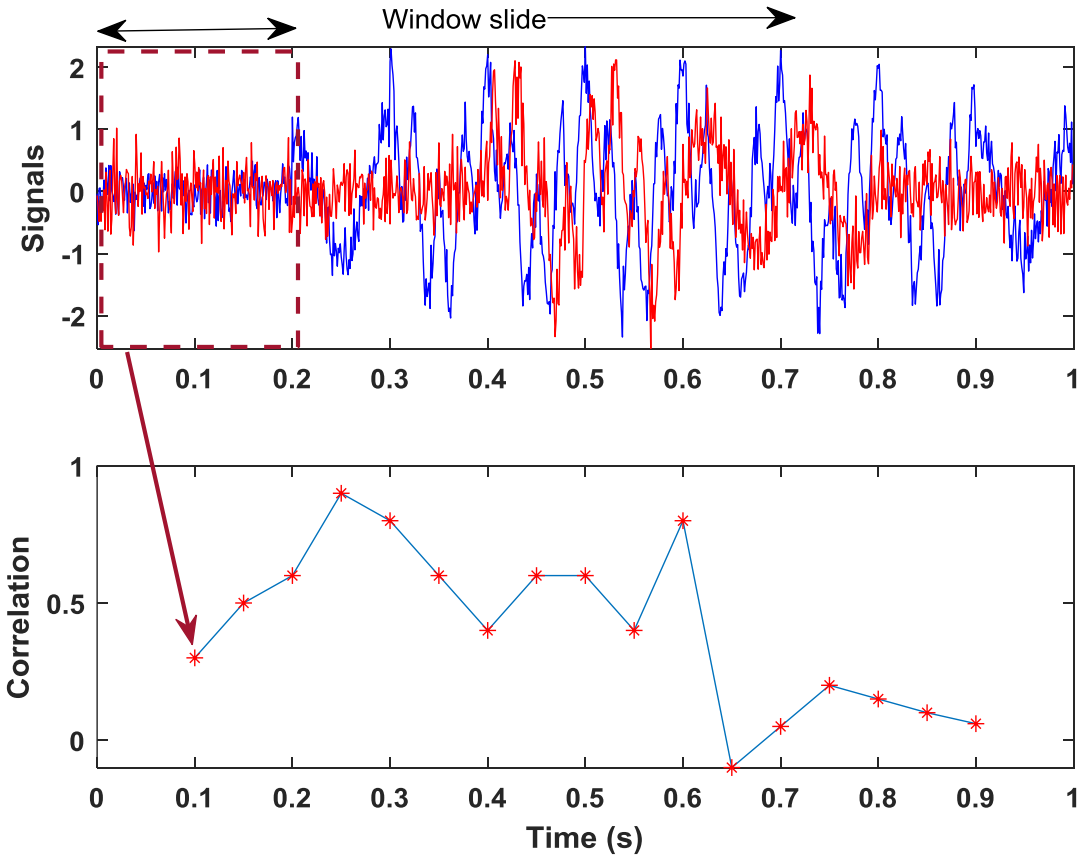

Figure 7-1: Illustration of the temporal resolution of functional connectivity (based on correlation) using a sliding window approach. The width of the window is 200 ms, window is stepped by 50 ms units. Red crosses represent the strength of connectivity based on the current time window.

Another example explaining the issue for a signal of 1 sec length and 1000 Hz sampling frequency: a window of minimum temporal resolution of 500 ms keeps the frequency resolution minimum to 2 Hz, while decreasing the window length lower than this interval smears the lower frequencies as delta band (1-4 Hz). So, the selected time window loses important details about the time-frequency varying information behind the scenes.

I give an example describing the problem of using the sliding window method for EEG brain connectivity calculation. Simulated two signals are generated with frequency components 10 and 40 Hz, with additive noise. The two signals have coherence in time period 400 to 600 millisecond as shown in the following figure.

$$x_1 = \cos(2\pi 10t)[t \geq 0.2, t < 1] + \sin(2\pi 40t)[t \geq 0.3, t < .9] + n1 \quad (7.1)$$
$$x_2 = \cos(2\pi 10t)[t \geq 0.4, t < .8] + \sin(2\pi 40t)[t \geq 0.4, t < .6] + n2$$

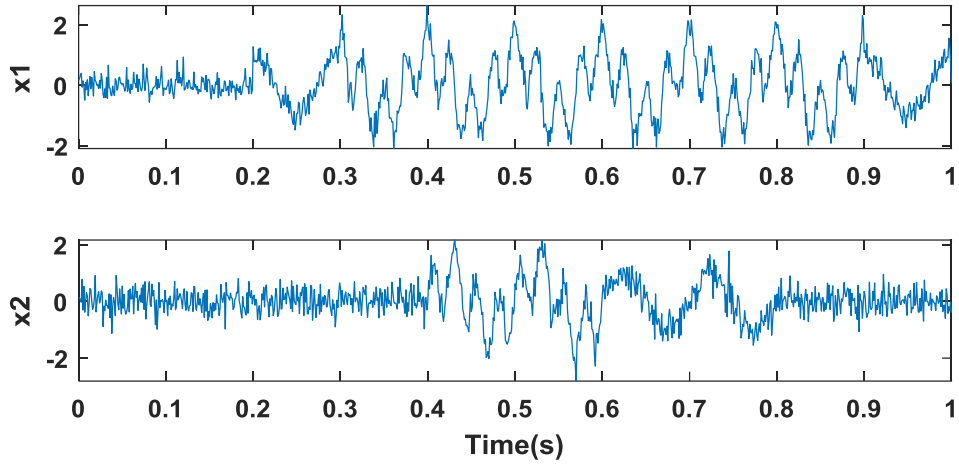

Figure 7-2: Simulated data for two channels. Signal length is 1 second and contains two frequency components at 10 and 40 Hz. Sampling frequency fs=1000 Hz.

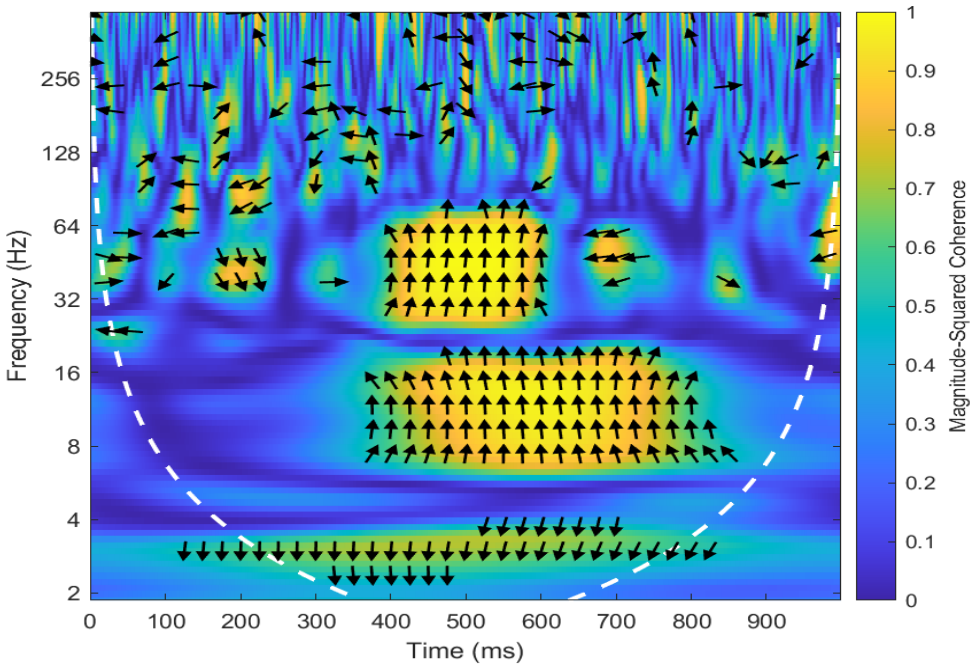

Figure 7-3: Wavelet coherence of the simulated data of 2 channels from Figure 7-2, note the low time resolution at frequency 3 Hz, and the low frequency resolution 64Hz to 128 Hz at 100ms.

Black arrows in the figure are used to represent phase lag of signal x_1 with respect to x_2. The direction of the arrows represents the phase lag on the unit circle: for example, a vertical arrow indicates a π/2 or quarter-cycle phase lag.

For one static time window of 1-second length, the connectivity is shown in Figure *7-4* without any details about the temporal resolution. Coherence (COH), Phase locked value (PLV) and Weighted Phase Lag Index (WPLI) are used for connectivity calculation.

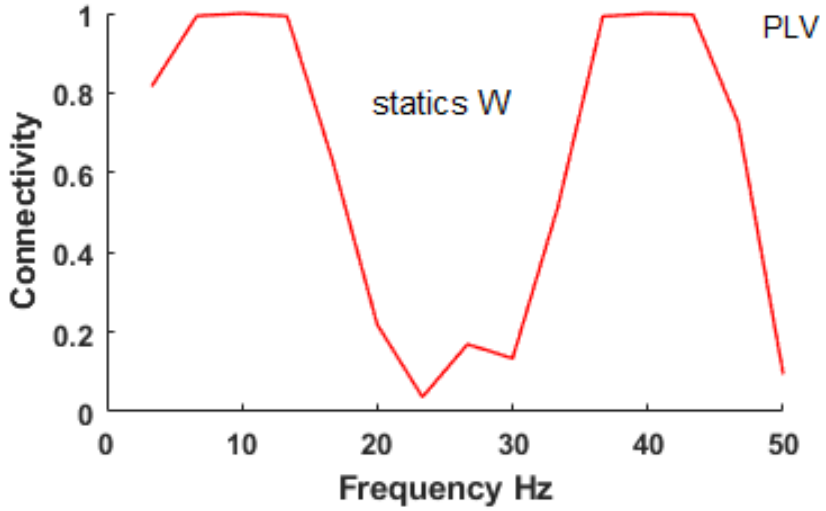

Figure 7-4:: Connectivity of simulated data based on PLV. Width of static time window is 1 second, coherence frequencies are 10 and 40 Hz.

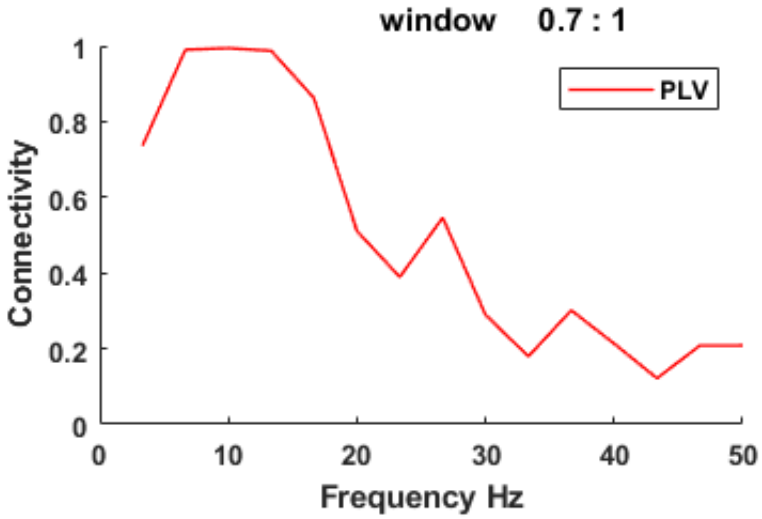

Figure 7-5:Connectivity of the simulated data based on PLV. Width of selected time window is 300 ms (0.7 to 1 second), at coherence frequencies 10 and 40 Hz.

Figure *7-5* shows that there is coherence between the two simulated signals at 10 Hz starting at time 0.7 to 1 seconds, which is not true, since the correct coherence at 10 Hz should end at 800 ms not to extend to the end of the time window.

Wavelet transformation was established for the time varying spectral estimate to overcome the spectral smearing. It used variable time window lengths which are adapted with the frequency of interest. So, long time windows are used for representing low frequencies therefore have good frequency, but low time resolution, while short windows are used for high frequencies estimate have good time resolution, but limited range of frequency resolution [33]. Thus, WT showed accepted temporal resolution on the high frequencies, while poor temporal resolution was located

in the low frequencies [34]. The chosen Wavelet function should be carefully selected with specific characteristics to improve the signal representation.

The synchrosqueezed Fourier transform is a derivation of the original Fourier transform [220] used to resemble the reassigned spectrogram through generating sharper time-frequency estimates than the traditional transform. It squeezes frequency contents to be concentrated around curves of instantaneous frequency in the time-frequency plane by convoluting it with a selected taper window function such as Hanning, Cosine and Blackman. The convolution process based on the selected window function causes time resolution limitations.

Autoregressive model was introduced by Yale et al.,[221] for time-varying frequency analysis. It was known by a liner prediction method, where the future values of signal could be predicted by the past P (model order) values generating the autoregressive coefficients. John Burg [222] used the autoregressive coefficients to calculate the autoregressive spectra. This has significant implications for the resulting frequency localization since the signal is not strictly windowed as the FFT-based approach. The autoregressive coefficients depend on two main parameters, the model order P and the window length of the signal, which has to be twice more than the model order. Since the model order is the curtail parameter in the method so, it should be neither too low, which generates a very smooth spectrum and other spectral peaks will be misplaced, nor too high, to avoid the spurious peaks and there may be spectral line splitting [223]. Since the window length one of the restrictions which controls the model order value, this procedure imposes the stationarity of the signal window.

7.2 Dynamic Connectivity based on the Empirical Mode Decomposition

Empirical Mode Decomposition (EMD) had been established by Huang et al. [210] to decompose non-stationary geophysical signals. It has been shown to be very adaptable in a wide range of many applications to extract signals from data generated in noisy nonlinear and non-stationary processes. When used for EEG, the decomposed signal can be expressed as the sum of the Intrinsic Mode Functions (IMF) representing the frequency bands (Delta, Theta, Alpha, Beta and Gamma), plus a residual. According to the data-local nature of the EMD, the decomposed signal is not totally separated mode function, since oscillations can be generated with very different scales in one mode, or with similar scales in different modes. Since similar scales can spread through mode functions, while the desired solution to have specific scale for each mode function, this issue is called mode-mixing and makes the EMD undesirable to be used in the sensitive application.

The frequent occurrence of mode-mixing problem resulted from signal intermittency, not only induced extreme aliasing in the time-frequency distribution, but also questioned the physical significance of the individual IMFs. Zhaohua et. al. [214] proposed a new method called Ensemble Empirical Mode Decomposition (EEMD) to solve the problem of mode-mixing. They introduced sifting an ensemble of white noise added to the signal, and considered the mean as the final true result and the new generated IMFs components consisting of the signal plus a white noise of finite amplitude.

They applied statistical properties of the white noise that proved that the EMD is effectively working as a filter bank once applied to noise. The dyadic filter bank is outlined as a group of band-pass filters that have a persistent band-pass form (e.g., a normal distribution) however with close filters covering half or double of the frequency of any single filter within the bank. The

additional noise would populate the full time–frequency scale uniformly with the constituting parts of various scales. The additional white noise would uniformly fill the complete time – frequency space with parts of various scales.

The EEMD was used in a wide range of applications. It was used for pathological voices processing by extracting the instantaneous fundamental frequency [224]. Despite its wide range of use, EEMD created new difficulties where the reconstructed signal, the final trend and the sum of the modes contains residual noise. Also, different signal realizations plus noise will generate a different number of modes, making final averaging difficult [216]. Yeh et. al. [225] proposed a complementary method to the EEMD which greatly alleviated the reconstruction issue by using complementary noise pairs (i.e., addition and subtraction). However, the completeness property could not be proven, and the final averaging issue remained unsolved since different noisy copies of the signal could generate a different number of modes.

Torres et al. [215] introduced important improvements to the EEMD to solve the problem of the reconstructed signal which still contains residual noise, by proposing a new approach called Complete Ensemble Empirical Mode Decomposition (CEEMDAN). They proposed that a particular noise has to be added at each stage of the decomposition and a unique residue was computed to obtain each mode. The resulting decomposition was complete, with a numerically negligible error. The new approach achieved a negligible reconstruction error and solved the problem of different number of modes for different realizations of signal plus noise. A better spectral separation of the modes with a lesser number of sifting iterations was achieved, moreover the computational cost was reduced. CEEMDAN was used in many applications in areas such as biomedical engineering [226], time-frequency analysis [227] and was used as pre-processing techniques for the analysis of Vibroarthrography signals [228].

In this work, I propose the use of the Improved Complete Ensemble Empirical Decomposition with Adaptive Noise [216] method to calculate instantaneous phase synchronizations and show that this new method radically improves the temporal accuracy of the calculated time-varying functional connectivity graphs. The application of EEMD-HH for dynamic EEG connectivity is completely new method in the tracking dynamic changes of brain connectivity and has not been suggested before in the literature.

The core of the proposed new method is to compute the instantaneous phase information of the EEG signal at different frequencies at high temporal resolution, from which a functional connectivity association matrix can be constructed to any time point. After thresholding the weights, a connectivity network can be created at each time instance and the temporal variation of the network metrics can be determined, or further graph-theoretic methods can be used to identify, e.g. dynamic community changes. The method will be tested on data from a finger-tapping experiment.

Using the Hilbert transform as a means to compute instantaneous frequency, promised better results, but the Hilbert transform breaks down for multicomponent, broadband EEG signals [210]. As an improvement, the Hilbert-Huang transform (HHT) based on Empirical Mode Decomposition (EMD) and Hilbert Spectral Analysis have been recommended [210,211] and was used successfully in EEG studies [212,213]. HHT was applied to the improved version of the CEEMDN, known as CEEMDAN-HHT and features were extracted from the estimated IMF of the non-stationary linear signal to show the wide range of frequency variation in time [228]. It is considered one of the best method used to localize the active brain sources by showing a good temporal resolution and identifying the frequency-band of EEG signal [229,230]. The high performance of the method regarding to time-frequency resolution, significantly made it to be used in neuro-sciences identification diseases, including a focus on detecting abnormalities in

sick new-borns in a Neonatal Intensive Care Unit (NICU), epileptic EEG signals, as well as mental health issues in elderlies [231]. It was applied in many biomedical applications such as showing the time-frequency analysis of FP1 EEG channel of alcoholic and non- alcoholic subjects [230]. Others used in EEG-Based brain intention recognition studies [232,233] to decompose original Steady state visually evoked potential (SSVEPs) into several IMFs. The instantaneous frequency of the SSVEP-related IMFs were computed, then the frequency which had the maximum presence probability and closest to the stimulation frequency was identified as the target [232]. Thus, the HHT is more robust than the FFT, and other frequency calculation methods meaning its accuracy in recognition does not change dramatically with data length.

I propose the use of the Complete Ensemble Empirical Mode Decomposition with Adaptive Noise [216] method to solve the low time-resolution and estimation problems of sliding window dynamic connectivity calculations. At each stage of the decomposition process, a particular noise was added, and a unique residue was calculated for obtaining each mode. The resulting decomposed IMFs are complete, with a numerically negligible error. Also, the method provided a better spectral separation of the modes with a lesser number of sifting iterations, moreover, the computational cost was reduced. The steps for the proposed method calculation are as follows:

a) Using CEEMDAN, the signals are first decomposed in an adaptive way into so-called intrinsic mode functions (IMFs) that represent constituent signal components. Unlike other decomposition methods, EMD-based approaches do not use special baseline functions. IMFs are created adaptively from the signal itself during an iterative sifting process [234]. Empirical Mode Decomposition acts as a dyadic (octave) filter bank that naturally follows the characteristics of the brain frequency bands and results in IMFs that correspond to gamma, beta, alpha, theta and delta band signals as shown in Figure *7-6*.

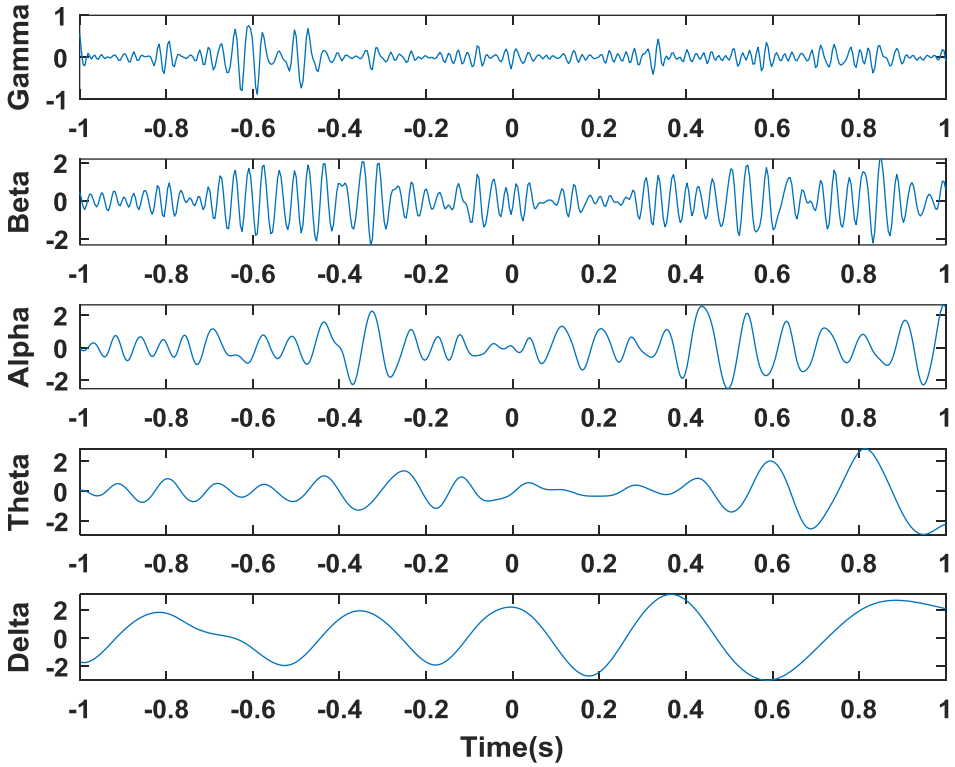

Figure 7-6: IMFs of the decomposed signal, 513-sample long of one trial, channel A1.

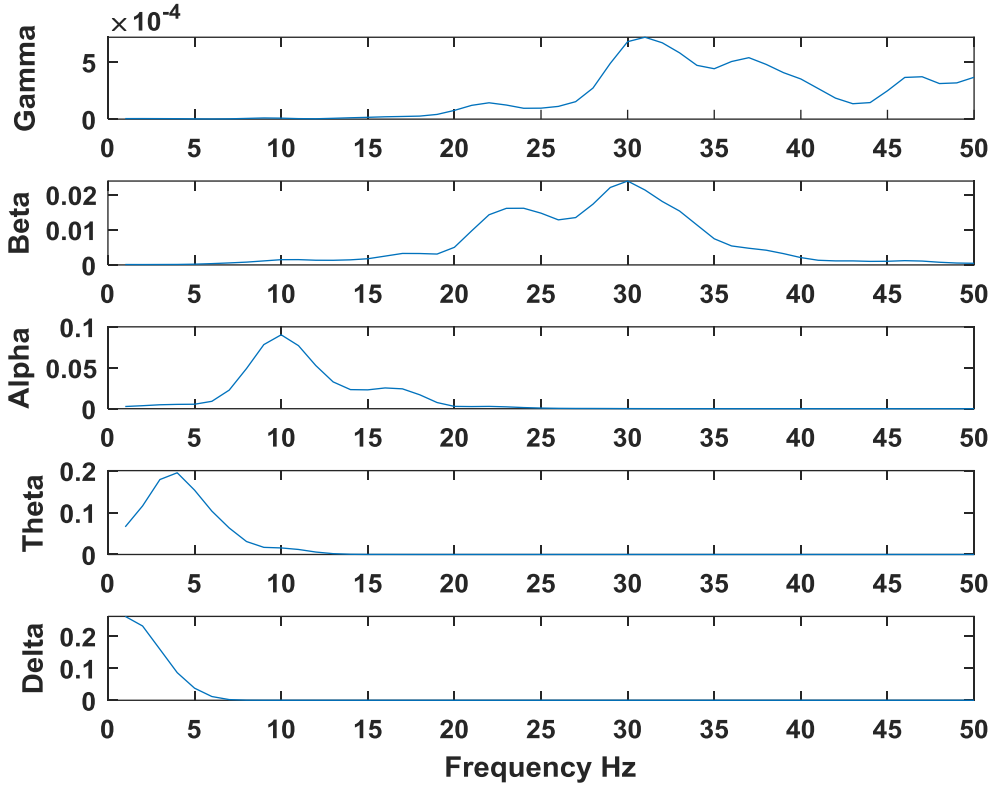

Figure 7-7: PSD of the calculated IMFs shown in Figure 7-6.

The CEEMDAN algorithm ensures that the decomposition process is robust in the presence of noise, separates IMFs correctly, minimizes error, and that the original signal can be reconstructed entirely from the modes.

The steps for CEEMDAN calculation are as follows:

1- Let E_k is the function which generates the k[th] mode/IMF from the EMD method as

$$E(s) = x - M(s) \quad (7.2)$$

where 's' is the input signal and M(.) refers to the function that outputs local mean of the input signal. The first mode/IMF $E_1$is defined by the following equation:

$$E_1(s) = x - M(s) \quad (7.3)$$

here 's' denotes the input signal $E_1(s)$ provides the first decomposition by EMD.

2- The set of ensembles denoted as $s^{(i)}$ is initially computed by the following equation

$$s^{(i)} = s + \beta_0 E_1(w^i) \quad (7.4)$$

where w^i is white noise of zero mean and unit variance while, $i \in (1,2,\dots I)$ is the ensemble number. Here β_0 represents a positive constant and in general ($\beta_{k-1} > 0$), and k indicates the mode number.

3- The local of mean for 'I' realization is computed by using the traditional EMD method i.e. $M(.)$ for the set of ensembles to get the first residue as shown in the equation below

$$r_1 = \langle M(s^{(i)}) \rangle \quad (7.5)$$

where $\langle . \rangle$ calculates the averaging operation over all the $i \in (1,2, \dots I)$.

4- The calculated residue r_1 is then subtracted from the signal 's' to derive the first mode C_1 which is given by this equation

$$C_1 = s - r_1 \quad (7.6)$$

5- Now the residue r_1 is considered as the base signal to compute the second residue as an average of the local means of $r_1 + \beta_1 E_2(w^i)$ same as the equation in step 1 and calculated residue defines the second mode C_2 as:

$$C_2 = r_1 - \langle \mathrm{M}(r_1 + \beta_1 E_2(w^i)) \rangle \quad (7.7)$$

6- From the above steps, the generalised kth residue can be given by

$$r_k = \langle \mathrm{M}(r_{k-1} + \beta_{k-1} E_k(w^i)) \rangle \quad (7.8)$$

7- Then the kth mode is given by

$$C_k = r_{k-1} - r_k \quad (7.9)$$

Step 6 and 7 are repeated for the next mode until the residue r_k cannot be further decomposed by EMD.

b) The IMFs are then processed using the Hilbert transform $h(t)$ to extract the instantaneous phase information as,

$$h(t) = \frac{1}{\pi} P \int_{-\infty}^{-\infty} \frac{s(\tau)}{t - \tau} \, \mathrm{d}\tau \quad (7.10)$$

where $s(t)$ is the input signal and P is Cauchy principal value for singular integral.

c) The transformed signal is then used in the calculation of the instantaneous PLV connectivity measure. Over all trials $n[1 \dots N]$, and for each channel pair at time t, PLV is calculated as:

$$PLV_t = \frac{1}{N} \left| \sum_{n=1}^{N} e^{j(\theta(t,n))} \right| \quad (7.11)$$

where $\theta(t,n)$ is the phase difference $\varphi_1(t,n) - \varphi_2(t,n)$.

7.3 Validation using Synthetic Signals

To test the temporal accuracy and resolution of the method, first artificial signals were examined. Four synthetic signals were created as mixtures of 10 and 40 Hz sine waves with fixed phased difference and added noise to test the temporal resolution of different functional connectivity methods. The signals in one trial were defined as:

$x_1(t) =$	$\sin(2\pi 10 * t) + \sin(2\pi 40 * t) + 0.15n_1(t)$	$t \in [0.2, 0.6],$
$x_2(t) =$	$\sin\left(2\pi 10t + \frac{\pi}{4}\right) + \sin\left(2\pi 40t + \frac{\pi}{4}\right) + 0.2n_2(t)$	$t \in [0.3, 1.6],$
$x_3(t) =$	$\sin\left(2\pi 10t + \frac{\pi}{3}\right) + \sin\left(2\pi 40t + \frac{\pi}{3}\right) + \sin\left(2\pi 10t + \frac{\pi}{3}\right) + \sin\left(2\pi 40t + \frac{\pi}{3}\right) + 0.25n_3(t)$	$t \in [0.8, 1.2]$ $t \in [1.7, 1.9],$
$x_4(t) =$	$\sin\left(2\pi 10t + \frac{\pi}{2}\right) + \sin\left(2\pi 40t + \frac{\pi}{2}\right) + 0.35n_4(t)$	$t \in [1.4, 1.8].$

When t is outside the specified intervals, each signal is random noise $n_i(t)$. I generated one hundred 2-second trials for the entire experiment; sampling frequency was f_s = 1000 Hz. The signal waveforms of a single trial with intervals of pairwise signal correlations are shown in Figure *7-8*.

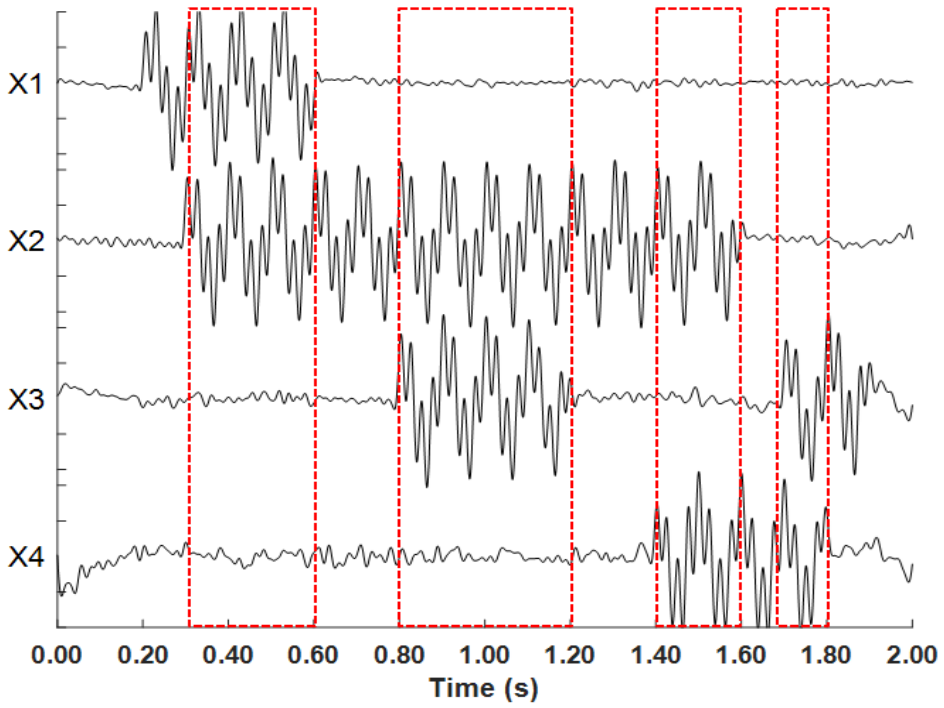

Figure 7-8: The synthetic signals used in the connectivity test. Rectangles mark time intervals in which connectivity is present between the pairs of signals.

7.3.1.1 Functional Connectivity Computation

Given two input signals $x_1(t)$ and $x_2(t)$, the cross-spectrum of the signals is defined as $X \equiv Z_1 Z_2^*$, where Z_1, and Z_2 are the Fourier spectra of the two input signals, and Z_2^* is the complex conjugate. The cross-spectrum can be also expressed in exponential form, $X = Re^{i\theta}$, where R is the magnitude and θ is the relative phase. Coherence [128] is the frequency domain equivalent of the correlation and is defined as the magnitude $|C|$ of the complex-valued coherency $C \equiv$

$E\{X\}/\sqrt{E\{M_1^2\}E\{M_2^2\}}$ where $E\{.\}$ is the expected value operator, $M_1 = |Z_1|$, and $M_2 = |Z_2|$. For uncorrelated sources I get $C = 0$, while positive values indicate correlation.

Since coherence is partly based on the magnitude of the signals that may cause spurious connections due to volume conduction, it has been suggested to use only the phase information in connectivity calculations [155]. The phase-locking value (PLV) [163] defined as $P \equiv \left|E\left\{e^{i\theta}\right\}\right|$ is a commonly used connectivity measure that uses only the relative phase information. Several improved metrics, less sensitive to relative phase values of 0 or π that are assumed to appear due to volume conduction, have been proposed in the literature, such as the imaginary component of coherence ImC $= |\Im\{X\}|$ [155], phase lag index PLI $= |E\{sgn(\Im\{X\})\}|$ [167], weighted phase lag index WPLI $= \left|E\left\{\Im\{X\}\right\}\right|/E\{|\Im\{X\}|\}$ and the debiased WPLI [54]. I refer the readers to the references for further details. For reasons of simplicity, only the PLV metric is used in this work but my method equally allows the use of any other phase-based metric.

Dynamic connectivity was first calculated using the sliding window technique. Window sizes of 0.25, 0.5 and 1 seconds were used to calculate PLV. Within a signal window, stationarity was assumed. After the Short-Time Fourier Transform was calculated, the PLV value was computed from the cross-spectrum. The window was moved by 50 ms steps over the entire trial to generate a time series of connectivity values. Figure *7-9* shows the connectivity between signals x_1 and x_2 for the three different window sizes. While the method detects changes in connectivity, when compared to the real correlation pattern, the error (approximately half of the window size at both sides) in estimation is evident. This makes this method unsuitable for tracking connectivity changes for tasks completing within few hundred milliseconds.

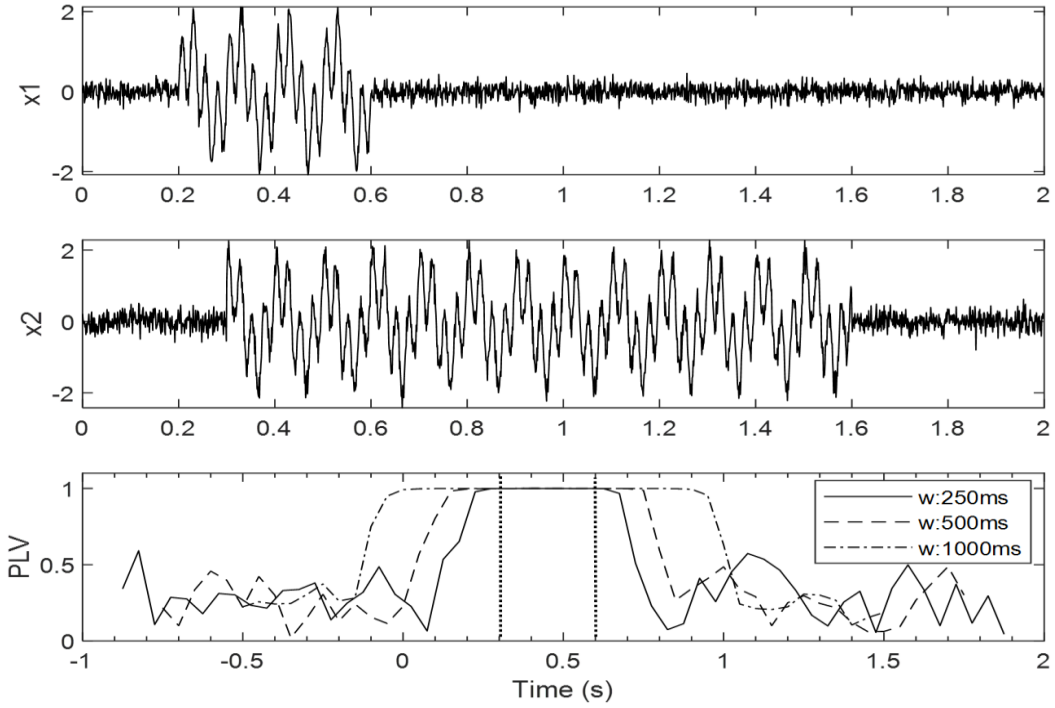

Figure 7-9: PLV connectivity values (bottom) calculated from signals x1 (top) and x2 (middle) using sliding window dynamic connectivity calculation. Window sizes used are 0.25, 0.5 and 1 seconds. Real connectivity appears between 0.3 and 0.6 seconds (dotted vertical lines.

The dynamic connectivity results given by the sliding window method, shown in Figure *7-9*, demonstrated that the sliding window techniques is inadequate for studying fast-changing brain

activities. The low temporal resolution is the result of the smearing effect of the large windows. Note that in order to study delta-band activity, 2-3 second windows would be required. Figure *7-10* illustrates the results given by my proposed dynamic instantaneous connectivity method. The top plot shows the phase locking values computed from the IMFs representing the 40 Hz, while the bottom representing the 10 Hz signal components, respectively

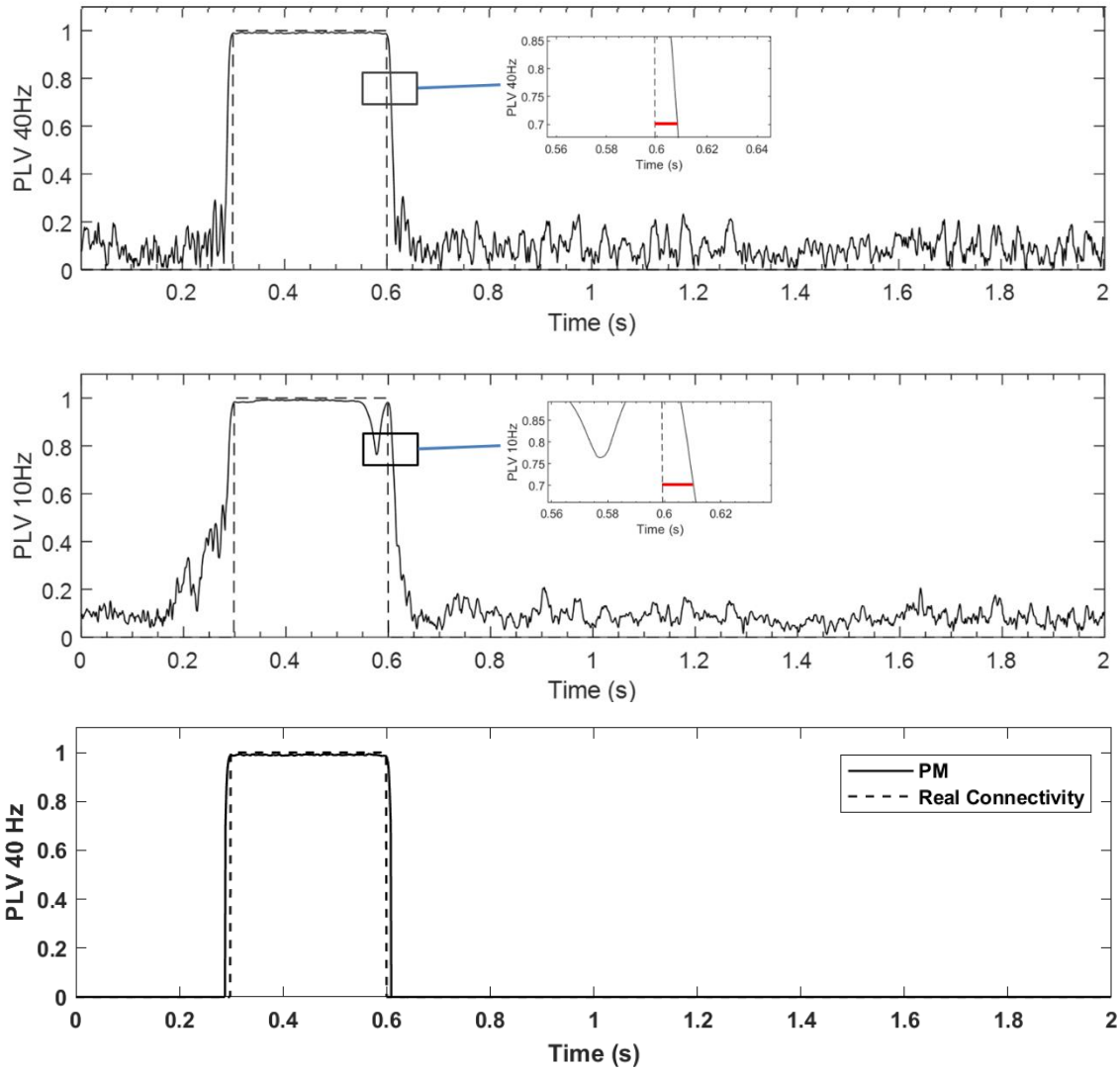

Figure 7-10: Instantaneous dynamic connectivity estimation of signals x1 and x2 from the 40 Hz (top) and 10 Hz (middle) IMFs with respect to the real connectivity (dashed line). Instantaneous dynamic connectivity estimation of signals x1 and x2 from the 40 Hz (bottom) after setting a threshold (th = 0.7).

The proposed method gives a more accurate estimate of the real connectivity between the signals, and the temporal resolution remains nearly constant over all frequencies. Using a PLV threshold of 0.7 to distinguish genuine connectivity from noise, resulted in a resolution of approximately 10 ms (see red lines insets in Figure *7-10*). By repeating the calculations for the IMFs of each pair of electrode signals, the complete connectivity association matrix can be created for each time step. From these matrices, a brain connectivity graph/network can be built then analysed using appropriate network metrics.

7.4 Validation using a Finger-tapping Experiment

This section describes the use of the new proposed method for investigating the dynamic functional connectivity of the brain during a task-related finger tapping experiment. The finger tapping experiment is an EEG experiment for testing the function and activity of the sensorimotor brain areas [235]. The experiment was performed by five volunteer subjects. Each subject had to press a button with the right index finger on a visual cue appearing approximately every five seconds. The cue is a small rectangle at the centre of the computer screen continuously changing its intensity level between black and mid-grey in front of a mid-grey background. The subject had to press the button when the small rectangle disappeared in the background.

Over 100 presses were recorded for each subject and the button press event was used to lock the trials during event-related trial averaging. The dataset was recorded by using Biosemi ActiveTwo EEG device with 128 channels using a radial ABC layout electrode cap and 2048 Hz sampling frequency. Time windows of two seconds long were selected (trials), one second before and on second after the button press. The key point of the finger tapping experiment is that the activity of the brain on the motor and sensory motor areas can be assessed with high time resolution. The dataset was cleaned from artefacts, then the proposed method of high time resolution functional connectivity was applied to the dataset. Several connectivity metrics were calculated and results were presented as a sequence of topographical maps.

Connectivity graphs were created for a selected time instance, before and within and after the finger press as shown in Figure 7-11. The sensory motor area connects to the motor area on the left side of the brain with clear patterns are shown at time 100 ms after the finger tap for theta band. Also, the visual cortex is activated and has links to the frontal area in the same time for alpha band. Strong connections are located in left motor cortex, beta band at the time of the finger press and nodes of this area indicate the importance of the node's connection by referring to the node size.

Many metrics can be explored to show the network connectivity changes, and node degree was selected as an indicator of varying connectivity. The graph connectivity metrics were calculated corresponding for different time instances with different frequency bands as shown in Figure 7-12. The theta band topoplot at time 100 ms shows high node degree values in the left sensory and motor areas that agree with the connectivity graphs in Figure 7-11.

Figure 7-12 shows seven sub figures on vertical view (for each frequency band) for temporal changes around time zero (time of the tap press) with step of 30 ms starting at -100 ms before the finger tapping and end at 100 ms from the press tap. The topoplot activity of the node degrees started on the left motor area at 30 ms/Theta after the press tapping and increased with widespread towards the left occipital area at time 70 ms to be greatly more concentrated on the left motor area at 100 ms. Similar activity was noticed for Delta band at -30 ms on the left motor area before the tapping and gradually increased till 70 ms, and then the activity reduced at 100 ms. Figure 7-13 shows the degree of nodes topoplot of sliding time window (400 ms width with 100 ms overlapping) for bands (Delta: D, Theta: T, Alpha: A) at t= -100 ms step 30 ms to 100 ms after the press tap. The topoplot activity extended over the entire time period from -100 to 100 ms for all bands, which makes the real activity hidden behind the averaged sliding window and hard to be tracked on time. Similar results for the local efficiency calculation were shown (Figure 7-14 and Figure 7-15) with the same time period to prove that the sliding window distorted the activity metrics and spread the activity of interest over the entire time window, making the tracking of brain activity changes during task execution in doubt.

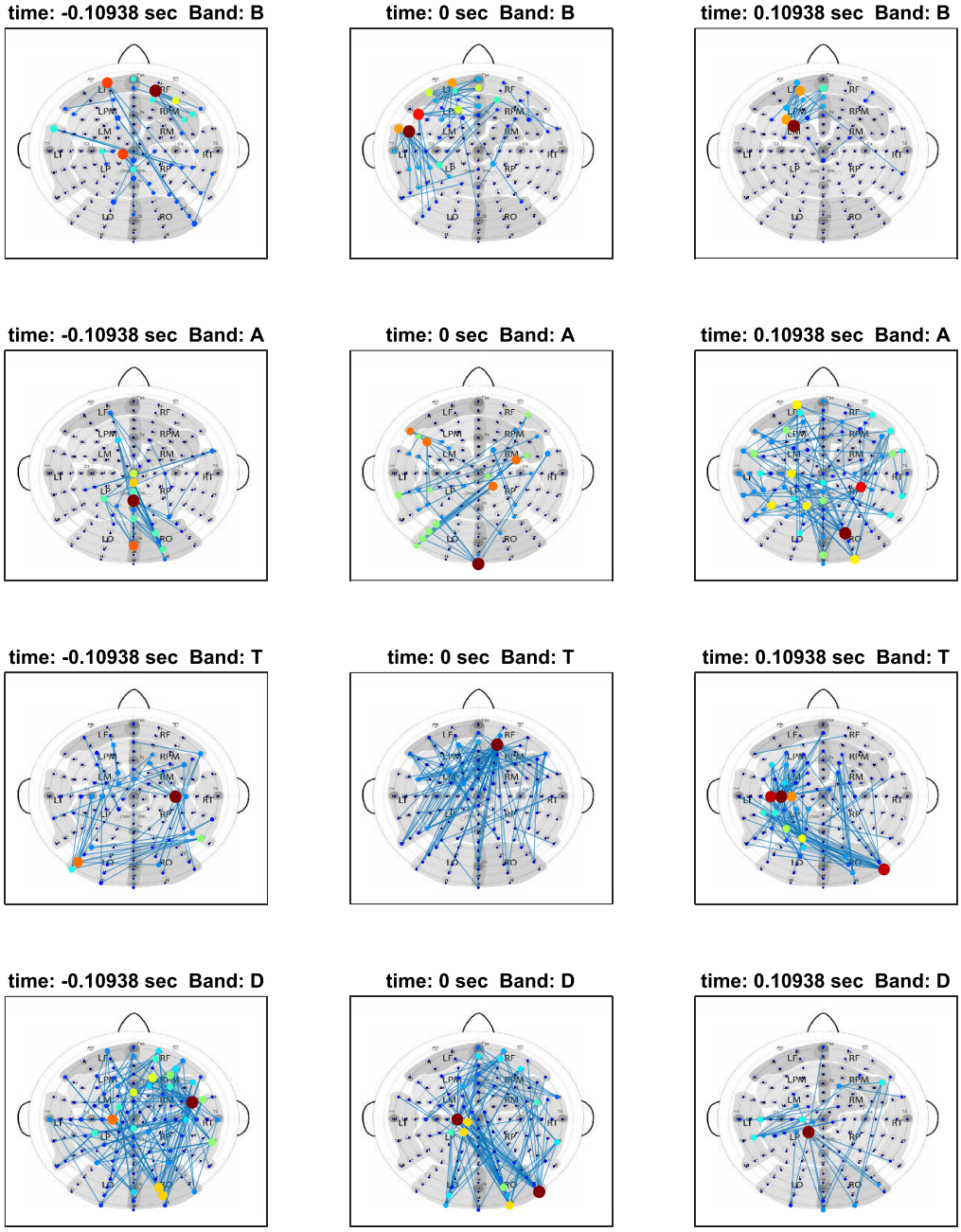

Figure 7-11: Connectivity graph of healthy subject finger tapping experiment for, Delta, Theta, Alpha and Beta bands. The graphs were calculated for three-time latencies -100 ms and 0 and 100 ms from the finger press.

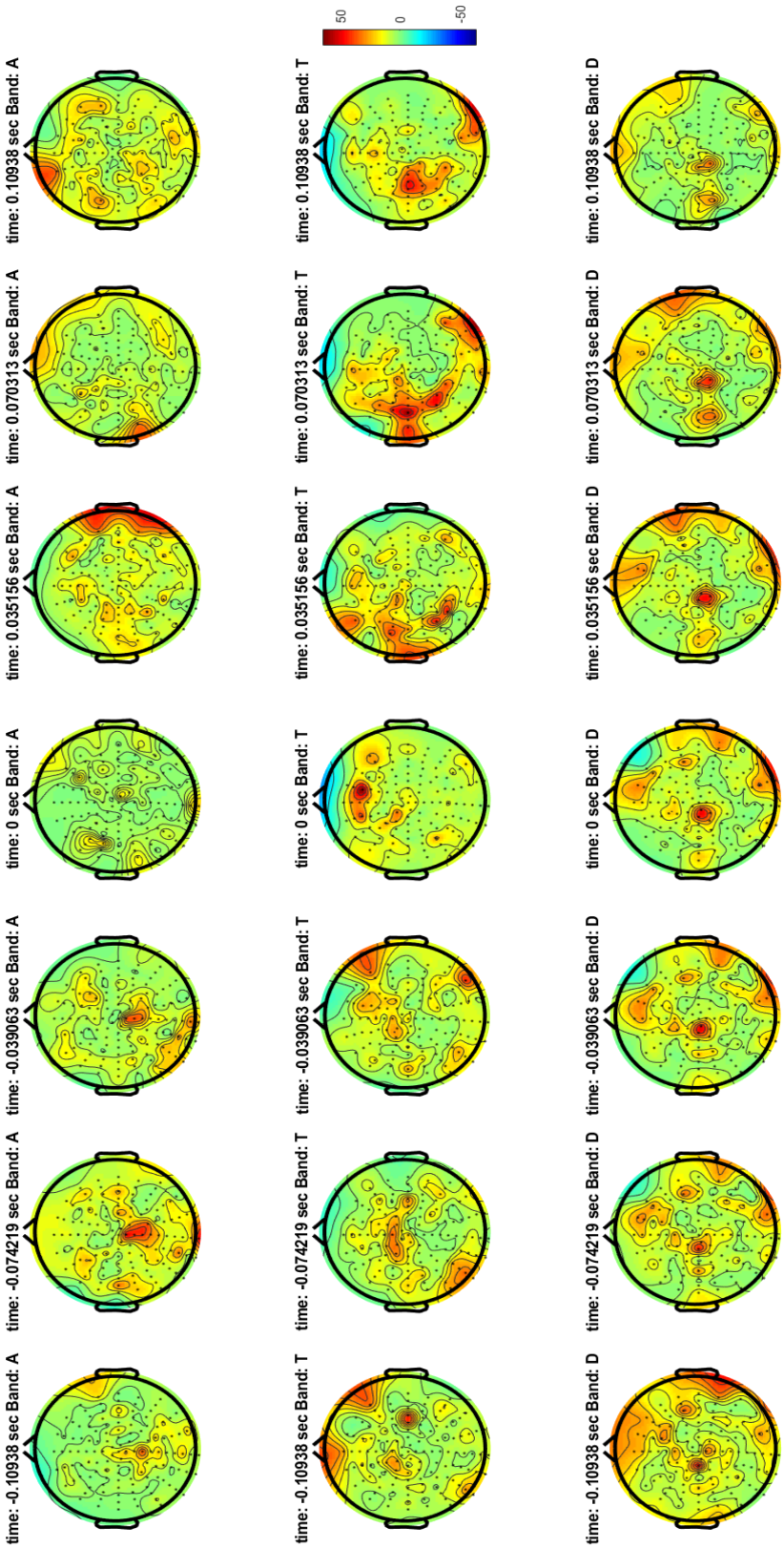

Figure 7-12: Changes in node degree in different frequency bands using the proposed method (columns left to right, Alpha: A, Theta: T, Delta: D) shown as topoplots from t= -100 ms to 100 ms relative to button press with approximately 30 ms time steps.

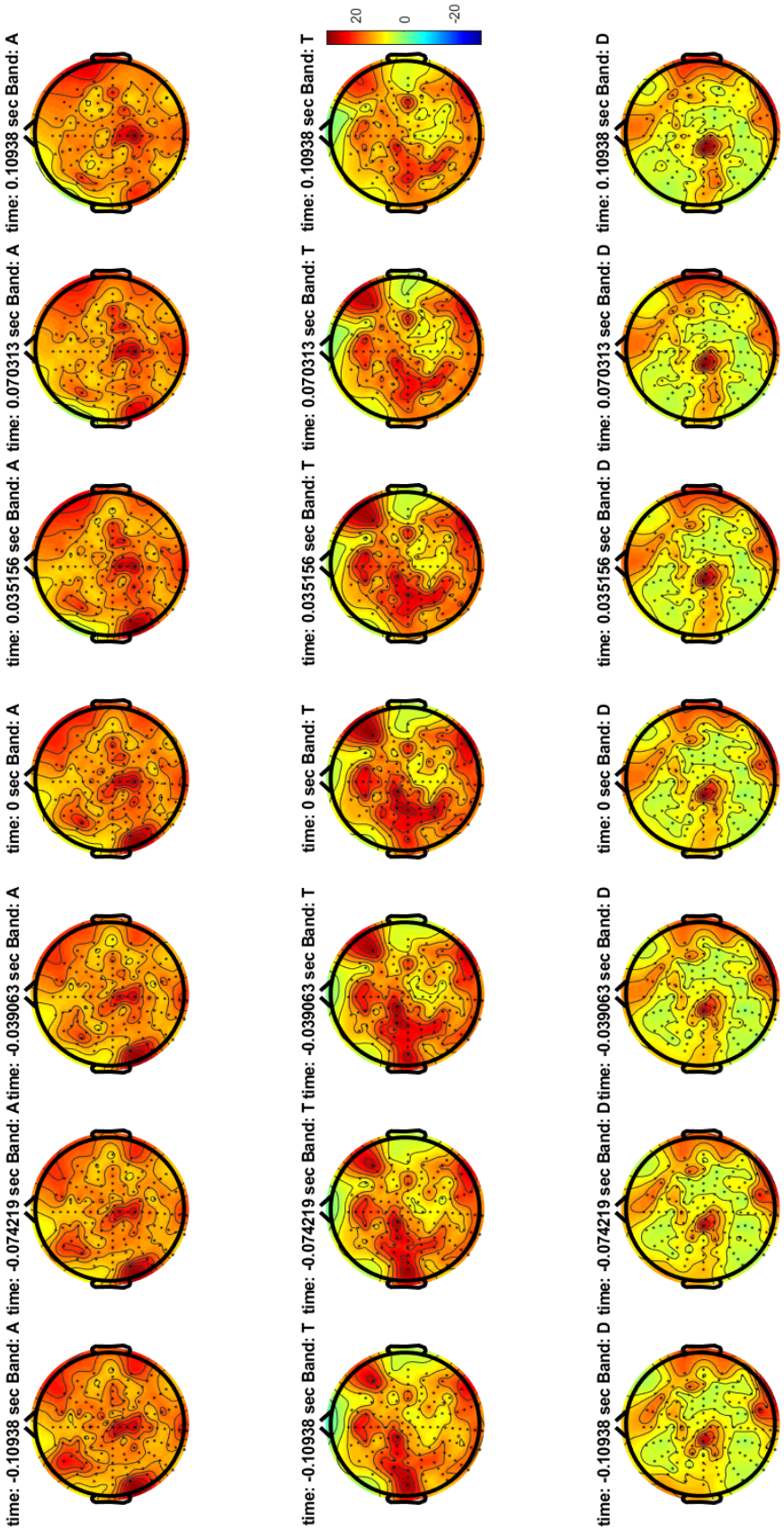

Figure 7-13: Node degree changes using sliding time window (400 ms width with 100 ms overlapping) for bands (Delta: D, Theta: T, Alpha: A) from time t= -100 ms to 100 ms relative to button press, with time step of 30 ms.

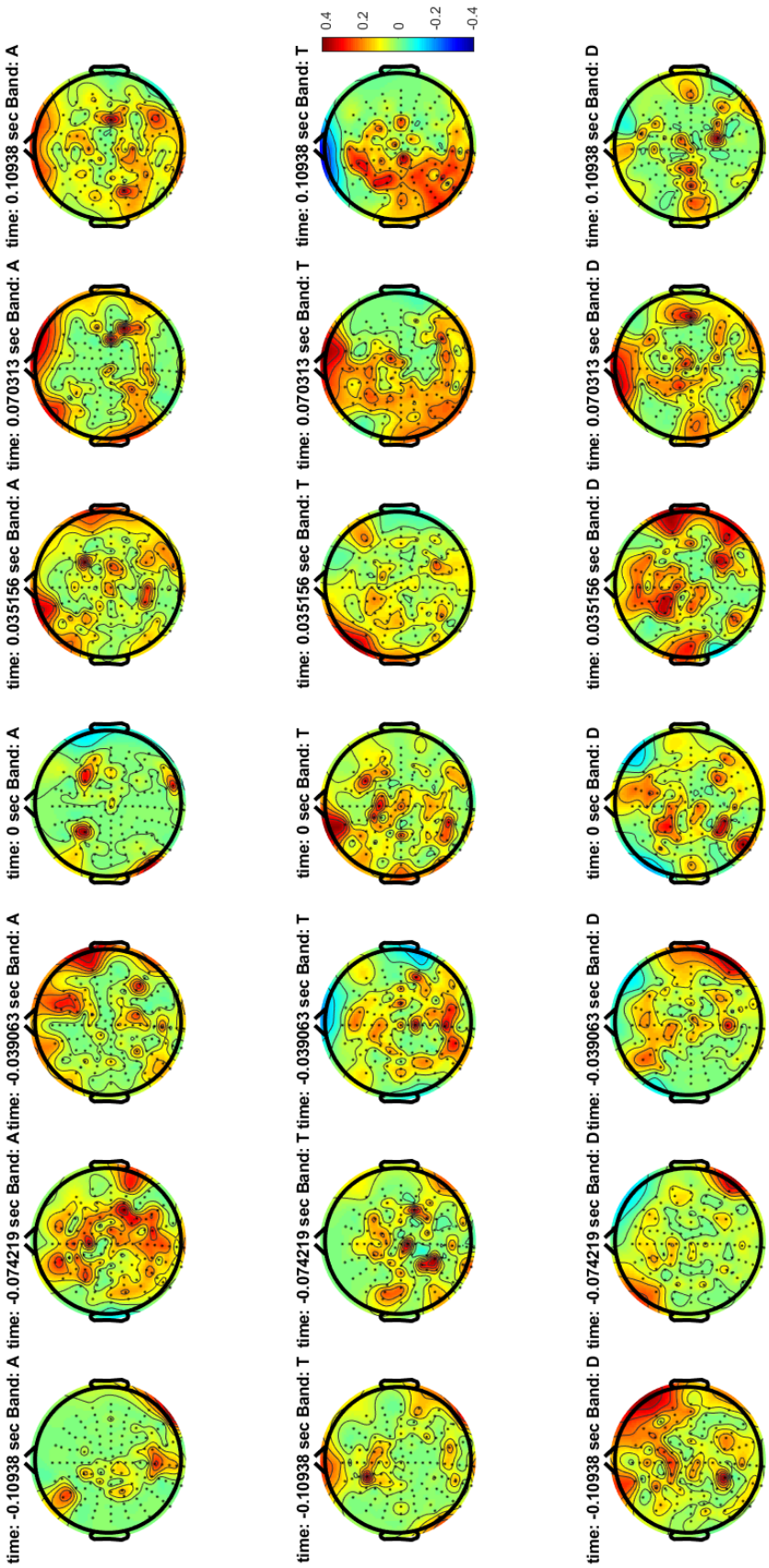

Figure 7-14: Topoplot of temporal changes in local efficiency using the proposed method for bands (Delta: D, Theta: T, Alpha: A) from time t= -100 ms to 100 ms relative to button press, with time step of 30 ms.

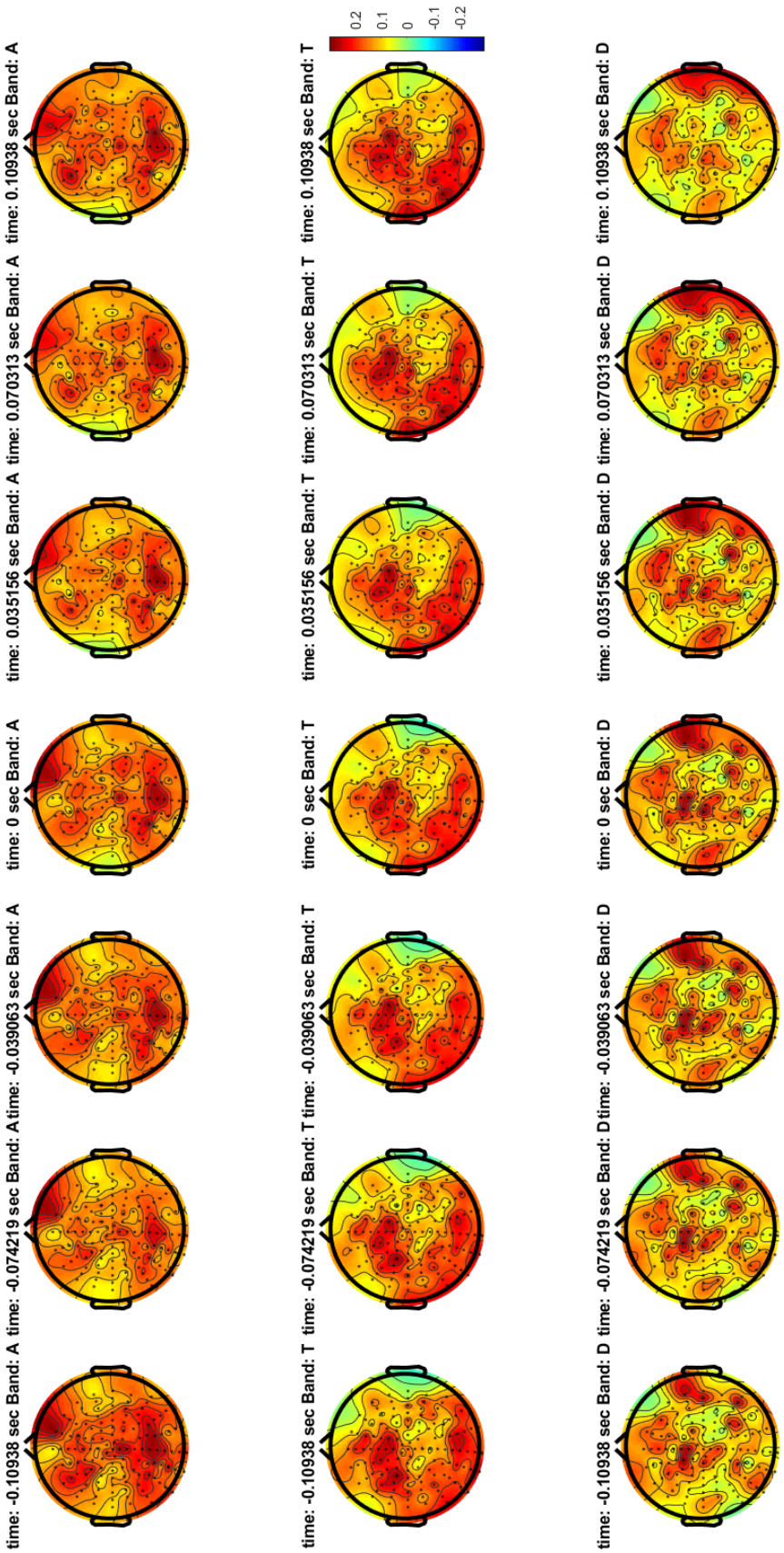

Figure 7-15: Local efficiency changes using sliding time window (400 ms width with 100 ms overlapping) for bands (Delta: D, Theta: T, Alpha: A) from time t= -100 ms to 100 ms relative to button press, with time step of 30 ms.

Two channels were selected from the sensory (D19) and motor (D13) areas to show how these two areas are connected during the finger tapping task. Several electrodes measure both areas, we selected the electrodes that had a peak in degree at and after the moment of press. The 100 ms delay between the motor and sensory electrodes confirm physiological behaviour, moreover, to prove the causality effect between these two sensors (one sensor causes the other one), Figure 7-16. Figure 7-17 shows how the node degree changes over time for the two selected channels, D13 and D19. A connection between the two electrodes D13 and D19 is located at 100 ms after the finger press with a delay refers to the way that the two sensors are effectively connected.

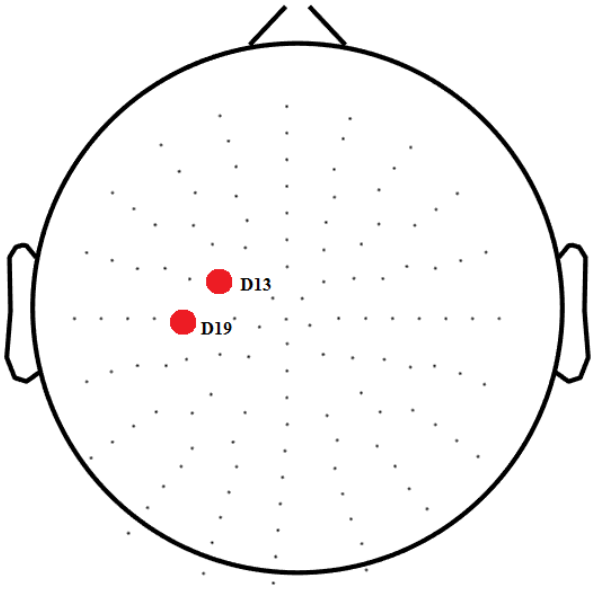

Figure 7-16: Position of channels D13 (left motor area) and D19 (left sensory area) in the 128-channel Biosemi cap layout.

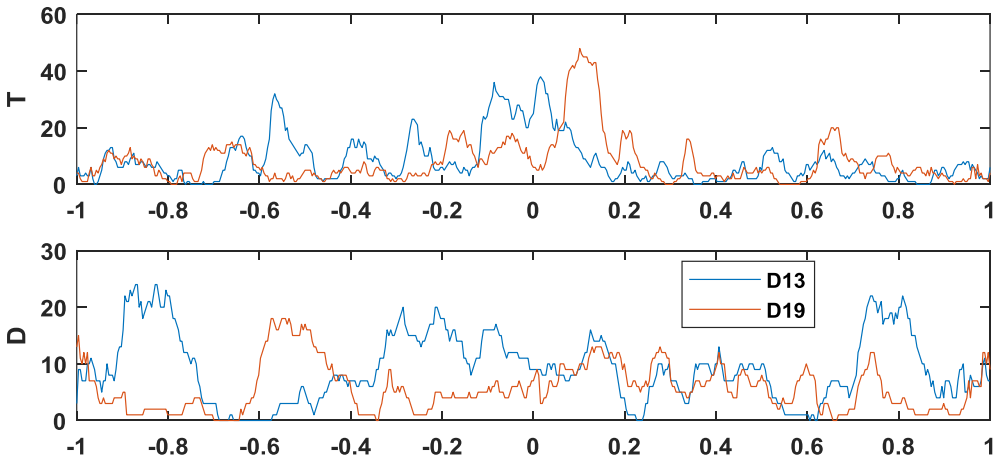

Figure 7-17: Node degree change over time in Theta and Delta band from 1 second before the finger press to 1 second after the press. Time t=0 refers to the button press event.

7.5 Summary

Functional connectivity provides insights into the collaboration of brain regions during resting state or task execution. Based on connectivity metrics, brain networks can be assembled, characterized and compared, opening up new possibilities for understanding and characterizing

healthy and diseased brain operation. The dynamism of these processes and the changes in network structure are expected to provide important information, yet, functional connectivity is still frequently computed on the assumption of stationarity. This work showed that fast-changing connectivity patterns cannot be tracked accurately by sliding-window dynamic connectivity methods. I proposed the use of the Ensemble Empirical Mode Decomposition and the Hilbert transform to extract the instantaneous phase information from the EEG data, and from this create millisecond-resolution dynamic connectivity information. Synthetic signals were used to demonstrate the correctness and temporal resolution of the proposed method. I used the phase locking value (PLV) for the connectivity calculation but the method works equally well with alternative connectivity measures. The proposed method was applied to task-related finger tapping experiment to track the changes that happen in the motor area and the synchronization in activities that happen in the other brain regions before, at and after the finger tap. The method showed the brain connectivity graphs and related connectivity metrics with different frequency bands in very high temporal resolution unlike the sliding time window approach that due to averaging over a larger temporal interval could not track brain activity with similar temporal accuracy. The proposed method enables the construction and analysis of high temporal resolution connectivity matrix time series, which may provide the basis for future research on the dynamic properties of brain networks.

8 Conclusions

In this chapter I summarise the results I got during the research work and state my main contributions. The measured EEG signals are regularly contaminated by ocular EOG, and cardiac artifacts (ECG) that are especially problematic due to their high amplitude and non-periodic (ocular, muscle) or quasi-periodic (cardiac) nature. They can easily turn valuable EEG measurements unusable. Since Visual inspection is slow, tiring and requires an expert assistant, several authors proposed methods for semi or fully automatic component detection and gave rise to new challenges including automating the analysis pipeline. The automation approach saves time, allows scalable analysis and reduces the barriers to reanalysis of data, thus facilitating reproducibility. In this sense, I proposed a novel method to clean the EEG from the EOG artifacts without losing EEG information. The developed automated artifact removal method combines the advantages of ICA-based artifact separation and wavelet decomposition. The new contribution for removing the EOG artifacts, is that the identified EOG component is cleaned only at the contaminated EOG peaks, while the rest of the component is left, retaining a higher portion of neural information that is present in the cleaned component. It reduces distortions that rejection ICA methods introduce in the time and frequency domain. Using simulated data and real measurements, my method outperforms state-of-the-art removal methods ICA-rej, and (wICA) both the time and frequency domain (significantly better 19.1%, $p = 0.00236$ than the wICA and 32.6% better $p = 1.43\times10\text{-}5$ than the reject ICA methods

The measured EEG signals are regularly contaminated by parodic ECG (cardiac) artifacts. Early ECG removal attempts included subtraction and ensemble average subtraction (EAS) methods. Current mainstream methods are based on adaptive filtering and reference ECG channel used to remove the ECG artifacts. The reported method used to remove the ECG artifacts by:

- *Manual rejection of artifact contaminated data epochs.*
- *Using ECG reference channel.*
- *visual inspection of ICA_ECG related components.*

The reported methods are laborious, require trained person, can largely reduce the number of usable epochs, and prevents the automatic and high-speed analysis of large-scale EEG.

I proposed a fully automatic method for removing ECG artefacts from EEG signals. The proposed method does not require a reference ECG channel. It can detect and remove ECG artefacts generated by pathological cardiac activities which can make the method more robust when analysing EEGs of elderly patients. It achieved sensitivity above 99.3% on the PhysioNet datasets (specificity > 99%), higher than all known automatic methods reported in literature [Dora and Jiang]. The significance of the method is that due to its excellent sensitivity and specificity, it can be used reliably for automatic, unsupervised artefact removal, where similar reported methods might incorrectly remove non-artefacts or leave contaminating components in the dataset. Cleaning artifact was very crucial, to move forward step towards the EEG connectivity calculation (graphs and metrics), since it would not be possible to get a true and undoubted metrics if the data set has artifacts.

The human brain comprises more than one hundred billion neurons, each establishing several thousand synaptic connection matrices which can be mathematically modelled for neuroimaging detecting diseases. Ischemic stroke is considered one of the major causes of death or causing a permanent disability. Prompt and effective treatment can speed up recovery and improve rehabilitation outcome. Brain connectivity metrics were introduced for selecting the proper treatment path and be used as predictors for the level of recovery at the end of the rehabilitation period. I introduced brain connectivity metrics with a high-density imaging method for

monitoring and quantifying stroke patient recovery progress. EEG measurements were recorded from healthy volunteers and stroke patients during the resting state function connectivity was calculated using debiased Weighted Phase Lag Index method (WPLI), and the graph approach was introduced to visualize the connectivity patterns of the networks at different frequency bands (Delta, Theta, Alpha, Beta). A comparison was performed between the patients and control group as well as between start and end of the stroke rehabilitation interval based on the results of the connectivity metrics as degree of nodes, local and global efficiency etc. Differences were found in the graph degree, clustering coefficient, global and local efficiency, which correlate with brain plasticity changes during stroke recovery and used as biomarkers to quantify stroke severity and outcome of recovery.

Over the past 30 years Fourier and Wavelet research to EEG signals increasingly has been the only approach representing "time-frequency" (TF) of EEG signals. These techniques, show resolution limitations (localization) due to the trade-off between time and frequency localizations and smearing due to the finite size of their template's time series, so this is the motivation point to compute instantaneous frequency based-method to generate a high temporal and spectral resolution at the same time and tracks the fast-dynamic brain connectivity changes. A novel method based on the use of the Ensemble Empirical Mode Decomposition was proposed to extract the instantaneous phase information from the EEG data. The method showed a millisecond-resolution dynamic connectivity information. Synthetic signals were used to demonstrate the correctness and temporal resolution of the proposed method. The proposed method enables the construction and analysis of high temporal resolution connectivity matrix time series, which may provide the basis for future research on the dynamic properties of brain networks. A comparison was conducted to validate the efficiency of the method and was compared to the static-sliding time window. The results showed that the proposed method able to track the fast-dynamic brain connectivity changes in time and frequency resolution at rate of sampling frequency better than using the traditional reported method as STFT.

9 Summary of the main contributions

9.1 Thesis I: Novel method for removing EOG artifacts

I developed a novel automated artifact removal method (Chapter 4.2) that combines the advantages of ICA-based artifact separation and wavelet decomposition. The novel contribution of the method is that eye artifact ICA components are not rejected entirely. Instead, artifactual components are cleaned only at contaminated sections, retaining a higher portion of neural information that is present in the artifact component. Using simulated data and real measurements I showed that my method outperforms state-of-the-art removal methods ICA-rej [111] and (wICA) [70] both in the time and frequency domain (significantly better 19.1%, $p = 0.00236$ than the wICA and 32.6% better $p = 1.43 \times 10^{-5}$ than the ICA-rej methods).

9.2 Thesis II: Novel method for removing ECG artifacts

I developed a fully automatic method for removing ECG artefacts (Chapter 5.1) using Independent Component Analysis (ICA). A sophisticated classification method is used to identify true ECG artifact components. My method does not require the use of a reference ECG channel, and can detect and remove ECG artefacts generated by pathological cardiac activities. The resulting sensitivity is above 99.3% on the PhysioNet datasets (specificity > 99%), higher than the best known automatic methods [9,10].

9.3 Thesis III: Functional connectivity biomarkers for stroke monitoring

I identified a set of functional connectivity graph metrics that can be used as biomarkers in identifying progress of recovery in ischemic stroke patients and predicting rehabilitation outcome (Chapter 6.3). Functional connectivity graphs were constructed from resting-state EEG measurements using the debiased weighted Phase Lag Index as association measure. The graphs were calculated for four different frequency bands (delta, theta, alpha and beta) with different thresholds. Connectivity measures were compared between patient and control groups at the beginning and end of the stroke rehabilitation period. The connectivity graph metrics showed differences in clustering coefficient, the graph degree, global and local efficiency, and correlated with brain plasticity changes during stroke recovery.

9.4 Thesis IV: New method to increase the temporal resolution of dynamic functional connectivity

I proposed a new method to create dynamic functional connectivity graphs with high temporal resolution that is considered the basis for future research on the dynamic properties of brain networks (Chapter 7.2). I proposed the use of the Ensemble Empirical Mode Decomposition and the Hilbert Transform to extract the instantaneous phase information from the EEG data, from which to create millisecond-resolution dynamic connectivity information using the Phase Locking Value (PLV). The proposed method provides a greater insight about the dynamism of the brain activity, where it can track the fast-dynamic brain connectivity changes in time and frequency resolution at rate of sampling frequency

List of Publications

1. **Issa, M.F**.; Juhasz, Z. Improved EOG Artifact Removal Using Wavelet Enhanced Independent Component Analysis. Brain Sci. 2019, 9, 355, **IF: 3.386, (Thesis I)**
2. **Mohamed F. Issa**, Gergely Tuboly, György Kozmann, Zoltan Juhasz, Automatic ECG artifact removal from EEG, Measurement Science Review, 19, (2019), No. 3, 101-108, **IF: 1.4, (Thesis II)**
3. **Mohamed F. Issa**, Gyorgy Kozmann, Zoltan Nagy, Zoltan Juhasz, Functional Connectivity Biomarkers based on Resting-state EEG for Stroke Recovery, Measurement 2019, 12th International Conference on Measurement, May 27-29, Smolenice, Slovakia, **(Thesis III).**
4. M.F. Issa, Z. Juhasz, Gy. Kozmann, Automatic Removal of EOG artefacts from EEG based on Independent Component Analysis, Pannonian Conference on Advances in Information Technology (PCIT 2019), 31 May – 1 June, Veszprem, Hungary (**(Thesis I).**
5. Z. Juhasz and **M.F. Issa**, EEG based imaging of stroke location, extent and progress of recovery using a GPU architecture, MIPRO 2019, 42th International Convention on Information and Communication Technology, Electronics and Microelectronics (MIPRO), Opatija, Croatia, May 20-24, 2019, **(Thesis III).**
6. **Mohamed F. Issa**, György Kozmann, and Zoltan Juhasz, Increasing the Temporal Resolution of Dynamic Functional Connectivity with Ensemble Empirical Mode Decomposition, submitted to EMBEC 2020, 8th European Medical and Biological Engineering Conference, Slovenia, 29 Nov-Dec 2020, *under review* **(Thesis IV).**
7. Juhász Z., **Issa, M**. Kozmann Gy, Nagy Z., Stroke betegek EEG alapú nyugalmi funkcionális konnektivitásának vizsgálata, IME - XIV. IME Képalkotó Diagnosztikai Továbbképzés és Konferencia, 2019. március 21., Budapest.
8. Zoltán Juhász, **Mohammed F. Issa**, János Körmendi, Ádám Gyulai, Zoltán Nagy, Quantitative EEG in stroke rehabilitation, 6th Neuroimaging Workshop, 19-20 Oct 2018, Pecs, Hungary. (abstract only)
9. Judit Navracsics, Gyula Sáry, Zoltán Juhász and **Mohamed F. Issa**, EEG correlates of L1 and L2 recognition, 20th Summer School of Psycholinguistics, June 10 – 14, 2018, Balatonalmadi, Hungary. (abstract only)
10. **Mohamed F. Issa**, Juhász Zoltán, Kozmann György, Agyi konnektivitási módszerek alkalmazása motoros és kognitív feladatok vizsgálatában, IME XIII. Képalkotó Diagnosztikai Továbbképzés és Konferencia, Budapest, 2018. március 22. (abstract only)
11. **Mohamed F. Issa**, Zoltan Juhasz and Gyorgy Kozmann, EEG analysis methods in neurolinguistics: a short review, IME: Interdiszciplináris Magyar Egészségügy/ Informatika és Menedzsment az Egészségügyben XVII : 2 pp. 48-54, (2018), **(Thesis III).**
12. Navracsics Judit, Juhász Zoltán, **Issa F. Mohamed**, Sáry Gyula, Kétnyelvűek vizuális szófelismerésének EEG korrelátumai, Tudomány Napja nemzetközi konferencia, Magyar és Alkalmazott Nyelvtudományi Intézet, 2017. november 3-4. (abstract only)
13. **M.F. Issa**, F. Csizmadia, Z. Juhasz, Gy. Kozmann, "EEG-Assisted Reaction Time Measurement Method for Bilingual Lexical Access Study Experiments", Proc. Measurement 2017, 11th International Conference on Measurement, Smolenice, Slovakia, May 29 - 31, 2017.

14. Judit Navracsics, Gyula Sáry, Zoltán Juhász, **Mohamed F. Issa**, EEG correlates of a bilingual language decision test, 19th Summer School of Psycholinguistics, May 21 – 25, 2017, Balatonalmadi, Hungary (abstract only)
15. Navracsics Judit, Juhász Zoltán, **Mohamed F. Issa** és Sáry Gyula, Kétnyelvűek vizuális szófelismerése és annak EEG korrelátumai, IME XV. Jubileumi Országos Infokommunikációs Konferencia, 2017. május 18., Budapest.

References

1. Nunez, P.L.; Srinivasan, R. *Electric fields of the brain : the neurophysics of EEG*; Oxford University Press, 2006; ISBN 019505038X.

2. Jurcak, V.; Tsuzuki, D.; Dan, I. 10/20, 10/10, and 10/5 systems revisited: Their validity as relative head-surface-based positioning systems. *Neuroimage* **2007**, *34*, 1600–1611.

3. Widmann, A.; Schröger, E.; methods, B.M.-J. of neuroscience; 2015, undefined Digital filter design for electrophysiological data–a practical approach. *Elsevier*.

4. Park, H.J.; Jeong, D.U.; Park, K.S. Automated detection and elimination of periodic ECG artifacts in EEG using the energy interval histogram method. *IEEE Trans. Biomed. Eng.* **2002**, *49*, 1526–1533.

5. Weidong Zhou; Gotman, J. Removal OF EMG and ECG artifacts from EEG based on real time recurrent learning algorithm. In Proceedings of the academicjournals.org; 2008; pp. 392–395.

6. Correa, A.G.; Laciar, E.; Patiño, H.D.; Valentinuzzi, M.E. Artifact removal from EEG signals using adaptive filters in cascade. *J. Phys. Conf. Ser.* **2007**, *90*, 012081.

7. Burel, G. Blind separation of sources: A nonlinear neural algorithm. *Neural Networks* **1992**, *5*, 937–947.

8. Vigário, R.; Särelä, J.; Jousmäki, V.; Hämäläinen, M.; Oja, E. *Independent Component Approach to the Analysis of EEG and MEG Recordings*; 2000; Vol. 47;.

9. Dora, C.; Biswal, P.K. Robust ECG artifact removal from EEG using continuous wavelet transformation and linear regression. In Proceedings of the 2016 International Conference on Signal Processing and Communications, SPCOM 2016; IEEE, 2016; pp. 1–5.

10. Jiang, J.A.; Chao, C.F.; Chiu, M.J.; Lee, R.G.; Tseng, C.L.; Lin, R. An automatic analysis method for detecting and eliminating ECG artifacts in EEG. *Comput. Biol. Med.* **2007**, *37*, 1660–1671.

11. Hamaneh, M.B.; Chitravas, N.; Kaiboriboon, K.; Lhatoo, S.D.; Loparo, K.A. Automated removal of EKG artifact from EEG data using independent component analysis and continuous wavelet transformation. *IEEE Trans. Biomed. Eng.* **2014**, *61*, 1634–1641.

12. Mak, J.N.F.; Hu, Y.; Luk, K.D.K. An automated ECG-artifact removal method for trunk muscle surface EMG recordings. *Med. Eng. Phys.* **2010**, *32*, 840–848.

13. Jas, M.; Engemann, D.A.; Bekhti, Y.; Raimondo, F.; Gramfort, A. Autoreject: Automated artifact rejection for MEG and EEG data. *Neuroimage* **2017**, *159*, 417–429.

14. Delorme, A.; Makeig, S.; Sejnowski, T. *AUTOMATIC ARTIFACT REJECTION FOR EEG DATA USING HIGH-ORDER STATISTICS AND INDEPENDENT COMPONENT ANALYSIS*; 2001;

15. Nolan, H.; Whelan, R.; Reilly, R.B. FASTER: Fully Automated Statistical Thresholding for EEG artifact Rejection. *J. Neurosci. Methods* **2010**, *192*, 152–162.

16. Mognon, A.; Jovicich, J.; Bruzzone, L.; Buiatti, M. ADJUST: An automatic EEG artifact detector based on the joint use of spatial and temporal features. *Psychophysiology* **2011**, *48*, 229–240.

17. Tadel, F.; Baillet, S.; Mosher, J. Brainstorm: a user-friendly application for MEG/EEG analysis. *dl.acm.org* **2011**, 1–13.

18. Delorme, A.; Makeig, S. EEGLAB: an open source toolbox for analysis of single-trial EEG dynamics

including independent component analysis. *J. Neurosci. Methods* **2004**, *134*, 9–21.

19. Oostenveld, R.; Fries, P.; Maris, E.; Schoffelen, J.M. FieldTrip: Open source software for advanced analysis of MEG, EEG, and invasive electrophysiological data. *Comput. Intell. Neurosci.* **2011**, *2011*, 156869.

20. Gramfort, A.; Luessi, M.; Larson, E.; Engemann, D.A.; Strohmeier, D.; Brodbeck, C.; Goj, R.; Jas, M.; Brooks, T.; Parkkonen, L.; et al. MEG and EEG data analysis with MNE-Python. *Front. Neurosci.* **2013**, *7*, 267.

21. Delorme, A.; Jung, T.-P.; Sejnowski, T.; Makeig, S. Enhanced detection of artifacts in EEG data using higher-order statistics and independent component analysis. *Neuroimage* **2007**, *34*, 1443–1449.

22. Hinkle, J.L. Reliability and Validity of the National Institutes of Health Stroke Scale for Neuroscience Nurses. *Stroke* **2014**, *45*.

23. Theofanidis, D.; Fitsioris, X.; Iakovos, T. Stroke Scales and Trajectory of Recovery: A Major Concern for Patients and Nurses Alike. *Heal. Sci. J. 9*.

24. Geraghty, J.R.; Testai, F.D. Delayed Cerebral Ischemia after Subarachnoid Hemorrhage: Beyond Vasospasm and Towards a Multifactorial Pathophysiology. *Curr. Atheroscler. Rep.* **2017**, *19*, 50.

25. Nuwer, M.R. Quantitative EEG: I. Techniques and problems of frequency analysis and topographic mapping. *J. Clin. Neurophysiol.* **1988**, *5*, 1–43.

26. Murri, L.; Gori, S.; Massetani, R.; Bonanni, E.; Marcella, F.; Milani, S. Evaluation of acute ischemic stroke using quantitative EEG: A comparison with conventional EEG and CT scan. *Neurophysiol. Clin. Neurophysiol.* **1998**, *28*, 249–257.

27. Wu, J.; Srinivasan, R.; Burke Quinlan, E.; Solodkin, A.; Small, S.L.; Cramer, S.C. Utility of EEG measures of brain function in patients with acute stroke. *J. Neurophysiol.* **2016**, *115*, 2399–2405.

28. Finnigan, S.; van Putten, M.J.A.M. EEG in ischaemic stroke: Quantitative EEG can uniquely inform (sub-)acute prognoses and clinical management. *Clin. Neurophysiol.* **2013**, *124*, 10–19.

29. Kanna, S.; Heng, J. Quantitative EEG parameters for monitoring and biofeedback during rehabilitation after stroke. In Proceedings of the 2009 IEEE/ASME International Conference on Advanced Intelligent Mechatronics; IEEE, 2009; pp. 1689–1694.

30. van Putten, M.J.A.M.; Tavy, D.L.J. Continuous Quantitative EEG Monitoring in Hemispheric Stroke Patients Using the Brain Symmetry Index. *Stroke* **2004**, *35*, 2489–2492.

31. Cavallini, A.; Micieli, G.; Marcheselli, S.; Quaglini, S. Role of Monitoring in Management of Acute Ischemic Stroke Patients. *Stroke* **2003**, *34*, 2599–2603.

32. Hall, M. Resolution and uncertainty in spectral decomposition. *First Break* **2006**, *24*, 43–47.

33. Kumar, P.; Foufoula-Georgiou, E. Wavelet analysis for geophysical applications. *Rev. Geophys.* **1997**, *35*, 385–412.

34. Tary, J.B.; Herrera, R.H.; Han, J.; Baan, M. Van Der Reviews of Geophysics Spectral estimation — What is new? What is next? *Rev. Geophys.* **2014**, *52*, 723–749.

35. Britton JW, Frey LC, Hopp JLet al., St. Louis EK, F.L. Electroencephalography (EEG): An Introductory Text and Atlas of Normal and Abnormal Findings in Adults, Children, and Infants Available online: https://www.ncbi.nlm.nih.gov/books/NBK390348/ (accessed on Nov 14, 2019).

36. Haas, L.F. Hans Berger (1873-1941), Richard Caton (1842-1926), and electroencephalography. *J. Neurol. Neurosurg. Psychiatry* **2003**, *74*, 9.

37. Vannemreddy, P.; Stone, J.L.; Slavin, K. V Frederic Gibbs and his contributions to epilepsy surgery and electroencephalography. *Neurosurgery* **2012**, *70*, 774–82.

38. Noachtar, S.; Rémi, J. The role of EEG in epilepsy: A critical review. *Epilepsy Behav.* 2009, *15*, 22–33.

39. Kim, H.T.; Kim, B.Y.; Park, E.H.; Kim, J.W.; Hwang, E.W.; Han, S.K.; Cho, S. Computerized recognition of Alzheimer disease-EEG using genetic algorithms and neural network. In Proceedings of the Future Generation Computer Systems; Elsevier B.V., 2005; Vol. 21, pp. 1124–1130.

40. Polikar, R.; Greer, M.H.; Udpa, L.; Keinert, F. Multiresolution wavelet analysis of ERPs for the detection of Alzheimer's disease. *Annu. Int. Conf. IEEE Eng. Med. Biol. - Proc.* **1997**, *3*, 1301–1304.

41. Papadourakis, G.; Vourkas, M.; Micheloyannis, S.; Jervis, B. Use of artificial neural networks for clinical diagnosis. *Math. Comput. Simul.* **1996**, *40*, 623–635.

42. Cash, S.S.; Halgren, E.; Dehghani, N.; Rossetti, A.O.; Thesen, T.; Wang, C.M.; Devinsky, O.; Kuzniecky, R.; Doyle, W.; Madsen, J.R.; et al. The human K-complex represents an isolated cortical down-state. *Science (80-.).* **2009**, *324*, 1084–1087.

43. Farwell, L.A.; Donchin, E. Talking off the top of your head: toward a mental prosthesis utilizing event-related brain potentials. *Electroencephalogr. Clin. Neurophysiol.* **1988**, *70*, 510–523.

44. Koles, Z.J. Trends in EEG source localization. *Electroencephalogr. Clin. Neurophysiol.* **1998**, *106*, 127–137.

45. Gao, J.; Sultan, H.; Hu, J.; Tung, W.W. Denoising nonlinear time series by adaptive filtering and wavelet shrinkage: A comparison. *IEEE Signal Process. Lett.* **2010**, *17*, 237–240.

46. Kanoga, S.; Mitsukura, Y. Review of Artifact Rejection Methods for Electroencephalographic Systems. In *Electroencephalography*; InTech, 2017.

47. Somers, B.; Francart, T.; Bertrand, A. A generic EEG artifact removal algorithm based on the multi-channel Wiener filter. *J. Neural Eng.* **2018**, *15*.

48. Izzetoglu, M.; Devaraj, A.; Bunce, S.; Onaral, B. Motion artifact cancellation in NIR spectroscopy using Wiener filtering. *IEEE Trans. Biomed. Eng.* **2005**, *52*, 934–938.

49. Feis, R.A.; Smith, S.M.; Filippini, N.; Douaud, G.; Dopper, E.G.P.; Heise, V.; Trachtenberg, A.J.; van Swieten, J.C.; van Buchem, M.A.; Rombouts, S.A.R.B.; et al. ICA-based artifact removal diminishes scan site differences in multi-center resting-state fMRI. *Front. Neurosci.* **2015**, *9*.

50. Lawhern, V.; Hairston, W.D.; Robbins, K. DETECT: A MATLAB Toolbox for Event Detection and Identification in Time Series, with Applications to Artifact Detection in EEG Signals. *PLoS One* **2013**, *8*, e62944.

51. Rahman, F.A.; Othman, M.F.; Shaharuddin, N.A. Analysis methods of EEG signals: A review in EEG application for brain disorder. *J. Teknol.* **2015**, *72*, 67–72.

52. Mouraux, A.; Iannetti, G.D. Across-trial averaging of event-related EEG responses and beyond. **2008**.

53. Jatoi, M.A.; Kamel, N.; Malik, A.S.; Faye, I.; Begum, T. A survey of methods used for source localization using EEG signals. *Biomed. Signal Process. Control* 2014, *11*, 42–52.

54. Vinck, M.; Oostenveld, R.; Van Wingerden, M.; Battaglia, F.; Pennartz, C.M.A. An improved index of phase-synchronization for electrophysiological data in the presence of volume-conduction, noise and sample-size bias. *Neuroimage* **2011**, *55*, 1548–1565.

55. Singer, W. Neuronal synchrony: A versatile code for the definition of relations? *Neuron* 1999, *24*, 49–65.

56. Xu, M.; Wang, T.; Chen, S.; Fox, P.T.; Tan, L.H. Effective connectivity of brain regions related to visual word recognition: An fMRI study of Chinese reading. *Hum. Brain Mapp.* **2015**, *36*, 2580–2591.

57. Guàrdia-Olmos, J.; Peró-Cebollero, M.; Zarabozo-Hurtado, D.; González-Garrido, A.A.; Gudayol-Ferré, E. Effective connectivity of visual word recognition and homophone orthographic errors. *Front. Psychol.* **2015**, *6*, 640.

58. Sporns, O. Brain connectivity. *Scholarpedia* **2007**, *2*, 4695.

59. Alexander, A.L.; Lee, J.E.; Lazar, M.; Field, A.S. Diffusion tensor imaging of the brain. *Neurotherapeutics* **2007**, *4*, 316–329.

60. Friston, K.J. Functional and Effective Connectivity: A Review. *Brain Connect.* **2011**, *1*, 13–36.

61. Rubinov, M.; Sporns, O. Complex network measures of brain connectivity: Uses and interpretations. *Neuroimage* **2010**, *52*, 1059–1069.

62. Citi, L.; Poli, R.; Cinel, C. Documenting, modelling and exploiting P300 amplitude changes due to variable target delays in Donchin's speller. *J. Neural Eng.* **2010**, *7*, 056006.

63. Goldberger, A.L.; Amaral, L.A.N.; Glass, L.; Hausdorff, J.M.; Ivanov, P.C.; Mark, R.G.; Mietus, J.E.; Moody, G.B.; Peng, C.-K.; Stanley, H.E. PhysioBank, PhysioToolkit, and PhysioNet : Components of a New Research Resource for Complex Physiologic Signals. *Circulation* **2000**, *101*, e215–e220.

64. Wnek, G.E.. & B.G.L. *Encyclopedia of Biomedical Engineering*; 2008;

65. Devuyst, S.; Dutoit, T.; Stenuit, P.; Kerkhofs, M.; Stanus, E. Removal of ECG artifacts from EEG using a modified independent component analysis approach. In Proceedings of the 2008 30th Annual International Conference of the IEEE Engineering in Medicine and Biology Society; IEEE, 2008; pp. 5204–5207.

66. Chen, X.; Liu, A.; Chiang, J.; Wang, Z.J.; McKeown, M.J.; Ward, R.K. Removing Muscle Artifacts From EEG Data: Multichannel or Single-Channel Techniques? *IEEE Sens. J.* **2016**, *16*, 1986–1997.

67. Maddirala, A.K.; Shaik, R.A. Motion artifact removal from single channel electroencephalogram signals using singular spectrum analysis. *Biomed. Signal Process. Control* **2016**, *30*, 79–85.

68. Sweeney, K.T.; Ward, T.E.; McLoone, S.F. Artifact removal in physiological signals-practices and possibilities. *IEEE Trans. Inf. Technol. Biomed.* **2012**, *16*, 488–500.

69. Mammone, N.; La Foresta, F.; Morabito, F.C. Automatic artifact rejection from multichannel scalp EEG by wavelet ICA. *IEEE Sens. J.* **2012**, *12*, 533–542.

70. Castellanos, N.P.; Makarov, V.A. Recovering EEG brain signals: Artifact suppression with wavelet enhanced independent component analysis. *J. Neurosci. Methods* **2006**, *158*, 300–312.

71. Jiang, X.; Bian, G.-B.; Tian, Z.; Jiang, X.; Bian, G.-B.; Tian, Z. Removal of Artifacts from EEG Signals: A Review. *Sensors* **2019**, *19*, 987.

72. Hyvärinen, A.; Oja, E. Independent component analysis: algorithms and applications. *Neural Networks* **2000**, *13*, 411–430.

73. Bigdely-Shamlo, N.; Mullen, T.; Kothe, C.; Su, K.-M.; Robbins, K.A. The PREP pipeline: standardized preprocessing for large-scale EEG analysis. *Front. Neuroinform.* **2015**, *9*, 16.

74. Tuyisenge, V.; Trebaul, L.; Bhattacharjee, M.; Chanteloup-Forêt, B.; Saubat-Guigui, C.; Mîndruţă, I.; Rheims, S.; Maillard, L.; Kahane, P.; Taussig, D.; et al. Automatic bad channel detection in intracranial electroencephalographic recordings using ensemble machine learning. *Clin. Neurophysiol.* **2018**, *129*, 548–554.

75. Lopez-Calderon, J.; Luck, S.J. ERPLAB: an open-source toolbox for the analysis of event-related potentials. *Front. Hum. Neurosci.* **2014**, *8*, 1–14.

76. Langlois, D.; Chartier, S.; Gosselin, D. *An Introduction to Independent Component Analysis: InfoMax and FastICA algorithms*; 2010; Vol. 6;.

77. Sahonero-Alvarez, G.; Calderón, H. A comparison of SOBI, FastICA, JADE and Infomax algorithms.

Proc. 8th Int. Multi-Conference Complexity, Informatics Cybern. **2017**, 17–22.

78. Burger, C.; Jacobus Van Den Heever, D. Removal of EOG artefacts by combining wavelet neural network and independent component analysis. *Biomed. Signal Process. Control* **2015**, *15*, 67–79.

79. Jung, T.P.; Makeig, S.; Westerfield, M.; Townsend, J.; Courchesne, E.; Sejnowski, T.J. Removal of eye activity artifacts from visual event-related potentials in normal and clinical subjects. *Clin. Neurophysiol.* **2000**, *111*, 1745–1758.

80. Romero, S.; Mananas, M.A.; Romero1', S.; Mailanas', M.A.; Clos2, S.; Gimenez2, S.; Barbanoj2, M.J. Reduction of EEG artifacts by ICA in different sleep stages Modelling of intoxication with organophosphorus compounds View project Human Action Monitoring View project Reduction of EEG Artifacts by ICA in Different Sleep Stages.

81. Urigüen, J.A.; Garcia-Zapirain, B. EEG artifact removal—state-of-the-art and guidelines. *J. Neural Eng.* **2015**, *12*, 031001.

82. Friston, K.J. Modes or models: A critique on independent component analysis for fMRI. *Trends Cogn. Sci.* **1998**, *2*, 373–375.

83. Mahajan, R.; Morshed, B.I. Unsupervised Eye Blink Artifact Denoising of EEG Data with Modified Multiscale Sample Entropy, Kurtosis, and Wavelet-ICA. *IEEE J. Biomed. Heal. Informatics* **2015**, *19*, 158–165.

84. Bian, N.Y.; Wang, B.; Cao, Y.; Zhang, L. Automatic removal of artifacts from EEG data using ICA and exponential analysis. In Proceedings of the Lecture Notes in Computer Science (including subseries Lecture Notes in Artificial Intelligence and Lecture Notes in Bioinformatics); Springer Verlag, 2006; Vol. 3972 LNCS, pp. 719–726.

85. Li, Y.; Ma, Z.; Lu, W.; Li, Y. Automatic removal of the eye blink artifact from EEG using an ICA-based template matching approach. *Physiol. Meas.* **2006**, *27*, 425–436.

86. Zhou, W.; Gotman, J. Automatic removal of eye movement artifacts from the EEG using ICA and the dipole model. *Prog. Nat. Sci.* **2009**, *19*, 1165–1170.

87. Engemann, D.A.; Gramfort, A. Automated model selection in covariance estimation and spatial whitening of MEG and EEG signals. *Neuroimage* **2015**, *108*, 328–342.

88. Joyce, C.A.; Gorodnitsky, I.F.; Kutas, M. Automatic removal of eye movement and blink artifacts from EEG data using blind component separation. *Psychophysiology* **2004**, *41*, 313–325.

89. Sweeney, K.T.; Ayaz, H.; Ward, T.E.; Izzetoglu, M.; McLoone, S.F.; Onaral, B. A methodology for validating artifact removal techniques for physiological signals. *IEEE Trans. Inf. Technol. Biomed.* **2012**, *16*, 918–926.

90. Greco, A.; Mammone, N.; Morabito, F.C.; Versaci, M. Kurtosis, Renyi's Entropy and Independent Component Scalp Maps for the Automatic Artifact Rejection from EEG data. *Int. J. Signal Process.* **2006**, *2*, 240–244.

91. Kelly, J.W.; Siewiorek, D.P.; Smailagic, A.; Collinger, J.L.; Weber, D.J.; Wang, W.; Kelly, J.W.; Siewiorek, D.P.; Smailagic, A.; Weber,) D J; et al. Fully Automated Reduction of Ocular Artifacts in High-Dimensional Neural Data. *IEEE Trans. Biomed. Eng.* **2011**, *58*.

92. Shoker, L.; Sanei, S.; Member, S.; Chambers, J. Artifact Removal From Electroencephalograms Using a Hybrid BSS-SVM Algorithm. *IEEE Signal Process. Lett.* **2005**, *12*, 721.

93. Halder, S.; Bensch, M.; Mellinger, J.; Bogdan, M.; Kübler, A.; Birbaumer, N.; Rosenstiel, W. Online artifact removal for brain-computer interfaces using support vector machines and blind source separation. *Comput. Intell. Neurosci.* **2007**, *2007*.

94. Woestenburg, J.C.; Verbaten, M.N.; Slangen, J.L. The removal of the eye-movement artifact from the EEG by regression analysis in the frequency domain. *Biol. Psychol.* **1983**, *16*, 127–147.

95. Hillyard, S.A.; Galambos, R. Eye movement artifact in the CNV. *Electroencephalogr. Clin. Neurophysiol.* **1970**, *28*, 173–182.

96. Wallstrom, G.L.; Kass, R.E.; Miller, A.; Cohn, J.F.; Fox, N.A. Automatic correction of ocular artifacts in the EEG: A comparison of regression-based and component-based methods. *Int. J. Psychophysiol.* **2004**, *53*, 105–119.

97. Gatsonis, C.; Hodges, J.; Kass, R.; Singpurwalla, N. *Case studies in bayesian statistics*; 2012;

98. Klados, M.A.; Papadelis, C.; Braun, C. REG-ICA: A hybrid methodology combining Blind Source Separation and regression techniques for the rejection of ocular artifacts. *Biomed. Signal Process. Control* **2011**, *6*, 291–300.

99. Mannan, M.M.N.; Jeong, M.Y.; Kamran, M.A. Hybrid ICA—Regression: Automatic Identification and Removal of Ocular Artifacts from Electroencephalographic Signals. *Front. Hum. Neurosci.* **2016**, *10*, 193.

100. Wang, Z.; Xu, P.; Liu, T.; Tian, Y.; Lei, X.; Yao, D. Robust removal of ocular artifacts by combining Independent Component Analysis and system identification. *Biomed. Signal Process. Control* **2014**, *10*, 250–259.

101. Time Frequency and Wavelets in Biomedical Signal Processing - IEEE Journals & Magazine Available online: https://ieeexplore.ieee.org/document/731313 (accessed on Nov 21, 2019).

102. Senthil Kumar, P.; Arumuganathan, R.; Sivakumar, K.; Vimal, C. *Removal of Ocular Artifacts in the EEG through Wavelet Transform without using an EOG Reference Channel*; 2008; Vol. 1;.

103. Amorim, P.; Moraes, T.; Fazanaro, D.; Silva, J.; Pedrini, H. Electroencephalogram signal classification based on shearlet and contourlet transforms. *Expert Syst. Appl.* **2017**, *67*, 140–147.

104. Sanjeeva Reddy, M.; Narasimha, B.; Suresh, E.; Subba Rao, K. Analysis of EOG signals using wavelet transform for detecting eye blinks. *2010 Int. Conf. Wirel. Commun. Signal Process. WCSP 2010* **2010**, 0–3.

105. Yasoda, K. Certain Analysis on EEG for the Detection of EOG Artifact Using Symlet Wavelet. *J. Theor. Appl. Inf. Technol.* **2014**, *10*.

106. Krishnaveni, V.; Jayaraman, S.; Aravind, S.; Hariharasudhan, V.; Ramadoss, K. *Automatic Identification and Removal of Ocular Artifacts from EEG using Wavelet Transform*; 2006; Vol. 6;.

107. Nguyen, H.-A.T.; Musson, J.; Li, F.; Wang, W.; Zhang, G.; Xu, R.; Richey, C.; Schnell, T.; McKenzie, F.D.; Li, J. EOG artifact removal using a wavelet neural network. *Neurocomputing* **2012**, *97*, 374–389.

108. Croft, R.J.; Barry, R.J. Removal of ocular artifact from the EEG: a review. *Neurophysiol. Clin. Neurophysiol.* **2000**, *30*, 5–19.

109. Shoker, L.; Sanei, S.; Wang, W.; Chambers, J.A. *Removal of eye blinking artifact from the electro-encephalogram, incorporating a new constrained blind source separation algorithm*;

110. Verleger, R. The instruction to refrain from blinking affects auditory P3 and N1 amplitudes. *Electroencephalogr. Clin. Neurophysiol.* **1991**, *78*, 240–51.

111. Joyce, C. A., Gorodnitsky, I. F., & Kutas, M. Joyce, C. A., Gorodnitsky, I. F., & Kutas, M. (2004). Automatic removal of eye movement and blink artifacts from EEG data using blind component separation. *Psychophysiology* **2004**, *41*, 313–325.

112. Zeng, H.; Song, A. Removal of EOG artifacts from EEG recordings using stationary subspace analysis. *ScientificWorldJournal.* **2014**, *2014*, 259121.

113. Wang, G.; Teng, C.; Li, K.; Zhang, Z.; Yan, X. The Removal of EOG Artifacts from EEG Signals Using Independent Component Analysis and Multivariate Empirical Mode Decomposition. *IEEE J. Biomed. Heal. Informatics* **2016**, *20*, 1301–1308.

114. Islam, M.K.; Rastegarnia, A.; Yang, Z. Methods for artifact detection and removal from scalp EEG: A review. *Neurophysiol. Clin.* 2016, *46*, 287–305.

115. Makeig, S.; Jung, T.-P.; Bell, A.J.; Sejnowski, T.J. Independent Component Analysis of Electroencephalographic Data. *Adv. neural Inf. Process. Syst.* **1996**, 145–151.

116. Read, G.L.; Innis, I.J. Electroencephalography (Eeg). In *The International Encyclopedia of Communication Research Methods*; Wiley, 2017; pp. 1–18.

117. Klados, M.A.; Bamidis, P.D. A semi-simulated EEG/EOG dataset for the comparison of EOG artifact rejection techniques. *Data Br.* **2016**, *8*, 1004–1006.

118. Langford, E. Quartiles in Elementary Statistics. *J. Stat. Educ.* **2006**, *14*.

119. Thomas, George B.; Weir, Maurice D.; Hass, J. *Thomas' calculus early transcendentals.*; 12th ed.; Addison-Wesley, 2010;

120. Fang, F.; Shinozaki, T. Electrooculography-based continuous eye-writing recognition system for efficient assistive communication systems. *PLoS One* **2018**, *13*, e0192684.

121. Kim, Y.S.; Baek, H.J.; Kim, J.S.; Lee, H.B.; Choi, J.M.; Park, K.S. Helmet-based physiological signal monitoring system. *Eur. J. Appl. Physiol.* **2009**, *105*, 365–372.

122. Kevric, J.; Subasi, A. Comparison of signal decomposition methods in classification of EEG signals for motor-imagery BCI system. *Biomed. Signal Process. Control* **2017**, *31*, 398–406.

123. Khatwani, P.; Tiwari, A. Removal of Noise from EEG Signals Using Cascaded Filter - Wavelet Transforms Method. *Int. J. Adv. Res. Electr. Electron. Instrum. Energy* **2014**, *3*, 13713–13719.

124. Daubechies, I.; Society for Industrial and Applied Mathematics. *Ten lectures on wavelets*; Society for Industrial and Applied Mathematics (SIAM, 3600 Market Street, Floor 6, Philadelphia, PA 19104), 1992; ISBN 1611970105.

125. Qinglin Zhao; Bin Hu; Yujun Shi; Yang Li; Moore, P.; Minghou Sun; Hong Peng Automatic Identification and Removal of Ocular Artifacts in EEG—Improved Adaptive Predictor Filtering for Portable Applications. *IEEE Trans. Nanobioscience* **2014**, *13*, 109–117.

126. Islam, M.K.; Rastegarnia, A.; Nguyen, A.T.; Yang, Z. Artifact characterization and removal for in vivo neural recording. *J. Neurosci. Methods* **2014**, *226*, 110–123.

127. Sweeney, K.T.; McLoone, S.F.; Ward, T.E. The Use of Ensemble Empirical Mode Decomposition With Canonical Correlation Analysis as a Novel Artifact Removal Technique. *IEEE Trans. Biomed. Eng.* **2013**, *60*, 97–105.

128. Carter, Gary and Knapp, Charles and Nuttall, A. Estimation of the magnitude-squared coherence function via overlapped fast Fourier transform processing. *IEEE Trans. audio Electroacoust.* **1973**, *21*, 337–344.

129. Majmudar, C.A.; Mahajan, R.; Morshed, B.I. Real-time hybrid ocular artifact detection and removal for single channel EEG. *IEEE Int. Conf. Electro Inf. Technol.* **2015**, *2015-June*, 330–334.

130. Khatun, S.; Mahajan, R.; Morshed, B.I. Comparative Study of Wavelet-Based Unsupervised Ocular Artifact Removal Techniques for Single-Channel EEG Data. *IEEE J. Transl. Eng. Heal. Med.* **2016**, *4*, 1–8.

131. Gudmundsson, S.; Runarsson, T.P.; Sigurdsson, S.; Eiriksdottir, G.; Johnsen, K. Reliability of quantitative EEG features. *Clin. Neurophysiol.* **2007**, *118*, 2162–2171.

132. Malekpour, S.; Gubner, J.A.; Sethares, W.A. Measures of generalized magnitude-squared coherence: Differences and similarities. *J. Franklin Inst.* **2018**, *355*, 2932–2950.

133. Jung, T.P.; Makeig, S.; Humphries, C.; Lee, T.W.; McKeown, M.J.; Iragui, V.; Sejnowski, T.J. Removing electroencephalographic artifacts by blind source separation. *Psychophysiology* **2000**,

37, 163–78.

134. Goldberger, A.L.; Amaral, L.A.; Glass, L.; Hausdorff, J.M.; Ivanov, P.C.; Mark, R.G.; Mietus, J.E.; Moody, G.B.; Peng, C.K.; Stanley, H.E. “PhysioBank, PhysioToolkit, PhysioNet: Com- ponents of a new research resource for complex physiologic signals,” Available online: http://www.ncbi.nlm.nih.gov/pubmed/10851218 (accessed on Oct 15, 2018).

135. Kel’manov, A.; Khamidullin, S.; Mikhailova, L.; Ruzankin, P. Polynomial-Time Solvability of One Optimization Problem Induced by Processing and Analyzing Quasiperiodic ECG and PPG Signals. In Proceedings of the Communications in Computer and Information Science; Springer, 2020; Vol. 1145 CCIS, pp. 88–101.

136. Christov, I.I. Real time electrocardiogram QRS detection using combined adaptive threshold. *Biomed. Eng. Online* **2004**, *3*, 28.

137. Elgendi, M.; Eskofier, B.; Dokos, S.; Abbott, D. Revisiting QRS detection methodologies for portable, wearable, battery-operated, and wireless ECG systems. *PLoS One* **2014**, *9*.

138. Automatic detection of A phases of the Cyclic Alternating Pattern during sleep. *ieeexplore.ieee.org*.

139. Friston, K.J. Modalities, Modes, and Models in Functional Neuroimaging. *Science (80-.).* **2009**, *326*, 399–403.

140. Fornito, A. An Introduction to Brain Networks. *Fundam. Brain Netw. Anal.* **2016**, 1–35.

141. Beckmann, C.F.; Deluca, M.; Devlin, J.T.; Smith, S.M.; Hospital, J.R.; Ox, O. Investigations into resting-state connectivity using independent component analysis. **2005**, 1001–1013.

142. Smith, S.M.; Fox, P.T.; Miller, K.L.; Glahn, D.C.; Fox, P.M.; Mackay, C.E.; Filippini, N.; Watkins, K.E.; Toro, R.; Laird, A.R.; et al. Correspondence of the brain’s functional architecture during activation and rest. *Proc. Natl. Acad. Sci. U. S. A.* **2009**, *106*, 13040–5.

143. Glasser, M.F.; Smith, S.M.; Robinson, E.C.; Uğurbil, K.; Vidaurre, D.; Woolrich, M.W.; Van Essen, D.C.; Barch, D.M.; Miller, K.L.; Nichols, T.E.; et al. Functional connectomics from resting-state fMRI. *Trends Cogn. Sci.* **2013**, *17*, 666–682.

144. Hutchison, R.M.; Womelsdorf, T.; Allen, E.A.; Bandettini, P.A.; Calhoun, V.D.; Corbetta, M.; Della Penna, S.; Duyn, J.H.; Glover, G.H.; Gonzalez-Castillo, J.; et al. Dynamic functional connectivity: promise, issues, and interpretations. *Neuroimage* **2013**, *80*, 360–78.

145. Bullmore, E.; Sporns, O. Complex brain networks: Graph theoretical analysis of structural and functional systems. *Nat. Rev. Neurosci.* **2009**, *10*, 186–198.

146. Li, J.G.; Chiu, J.; Praticò, D. Full recovery of the Alzheimer’s disease phenotype by gain of function of vacuolar protein sorting 35. *Mol. Psychiatry* **2019**, 1–11.

147. Friston, K.J. Functional and effective connectivity in neuroimaging: A synthesis. *Hum. Brain Mapp.* **1994**, *2*, 56–78.

148. Lang, E.W.; Tomé, A.M.; Keck, I.R.; Górriz-Sáez, J.M.; Puntonet, C.G. Brain Connectivity Analysis: A Short Survey. *Comput. Intell. Neurosci.* **2012**, *2012*, 1–21.

149. Orfanidis, S.J. Optimum signal processing: an introduction 2nd Ed 1988, 42–45.

150. Nunez, P.L.; Srinivasan, R.; Westdorp, A.F.; Wijesinghe, R.S.; Tucker, D.M.; Silberstein, R.B.; Cadusch, P.J. EEG coherency: I: statistics, reference electrode, volume conduction, Laplacians, cortical imaging, and interpretation at multiple scales. *Electroencephalogr. Clin. Neurophysiol.* **1997**, *103*, 499–515.

151. Lachaux, J.-P.; Lutz, A.; Rudrauf, D.; Cosmelli, D.; Le Van Quyen, M.; Martinerie, J.; Varela, F. Estimating the time-course of coherence between single-trial brain signals: an introduction to wavelet coherence. *Neurophysiol. Clin. Neurophysiol.* **2002**, *32*, 157–174.

152. Sakkalis, V. Review of advanced techniques for the estimation of brain connectivity measured with EEG/MEG. *Comput. Biol. Med.* **2011**, *41*, 1110–1117.

153. Kamiński, M.; Blinowska, K.; neurophysiology, W.S. clinical; 1997, undefined Topographic analysis of coherence and propagation of EEG activity during sleep and wakefulness. *Elsevier*.

154. Blinowska, K.J.; Kaminski, M.; Brzezicka, A.; Kaminski, J. Application of directed transfer function and network formalism for the assessment of functional connectivity in working memory task. *Philos. Trans. R. Soc. A Math. Phys. Eng. Sci.* **2013**, *371*, 20110614–20110614.

155. Nolte, G.; Bai, O.; Wheaton, L.; Mari, Z.; Vorbach, S.; Hallett, M. Identifying true brain interaction from EEG data using the imaginary part of coherency. *Clin. Neurophysiol.* **2004**, *115*, 2292–2307.

156. García Domínguez, L.; Stieben, J.; Pérez Velázquez, J.L.; Shanker, S. The Imaginary Part of Coherency in Autism: Differences in Cortical Functional Connectivity in Preschool Children. *PLoS One* **2013**, *8*, e75941.

157. Hohlefeld, F.U.; Huchzermeyer, C.; Huebl, J.; Schneider, G.-H.; Nolte, G.; Brücke, C.; Schönecker, T.; Kühn, A.A.; Curio, G.; Nikulin, V.V. Functional and effective connectivity in subthalamic local field potential recordings of patients with Parkinson's disease. *Neuroscience* **2013**, *250*, 320–332.

158. Mormann, F.; Lehnertz, K.; David, P.; E. Elger, C. Mean phase coherence as a measure for phase synchronization and its application to the EEG of epilepsy patients. *Phys. D Nonlinear Phenom.* **2000**, *144*, 358–369.

159. Stam, C.J.; de Haan, W.; Daffertshofer, A.; Jones, B.F.; Manshanden, I.; van Cappellen van Walsum, A.M.; Montez, T.; Verbunt, J.P.A.; de Munck, J.C.; van Dijk, B.W.; et al. Graph theoretical analysis of magnetoencephalographic functional connectivity in Alzheimer's disease. *Brain* **2009**, *132*, 213–224.

160. Kaminski, M.; Blinowska, K.J. Directed Transfer Function is not influenced by volume conduction-inexpedient pre-processing should be avoided. *Front. Comput. Neurosci.* **2014**, *8*, 61.

161. Bastos, A.M.; Schoffelen, J.-M. A Tutorial Review of Functional Connectivity Analysis Methods and Their Interpretational Pitfalls. *Front. Syst. Neurosci.* **2016**, *9*, 175.

162. Sakkalis, V.; Giurcaneanu, C.D.; Xanthopoulos, P.; Zervakis, M.E.; Tsiaras, V.; Yang, Y.; Karakonstantaki, E.; Micheloyannis, S. Assessment of Linear and Nonlinear Synchronization Measures for Analyzing EEG in a Mild Epileptic Paradigm. *IEEE Trans. Inf. Technol. Biomed.* **2009**, *13*, 433–441.

163. Lachaux, J.-P.; Rodriguez, E.; Martinerie, J.; Varela, F.J. Measuring phase synchrony in brain signals. *Hum. Brain Mapp.* **1999**, *8*, 194–208.

164. Fries, P. Rhythms for Cognition: Communication through Coherence. *Neuron* 2015, *88*, 220–235.

165. Garcés, P.; Martín-Buro, M.C.; Maestú, F. Quantifying the Test-Retest Reliability of Magnetoencephalography Resting-State Functional Connectivity. *Brain Connect.* **2016**, *6*, 448–460.

166. López, M.E.; Bruña, R.; Aurtenetxe, S.; Pineda-Pardo, J.Á.; Marcos, A.; Arrazola, J.; Reinoso, A.I.; Montejo, P.; Bajo, R.; Maestú, F. Alpha-band hypersynchronization in progressive mild cognitive impairment: A magnetoencephalography study. *J. Neurosci.* **2014**, *34*, 14551–14559.

167. Stam, C.J.; Nolte, G.; Daffertshofer, A. Phase lag index: Assessment of functional connectivity from multi channel EEG and MEG with diminished bias from common sources. *Hum. Brain Mapp.* **2007**, *28*, 1178–1193.

168. Lau, T.M.; Gwin, J.T.; McDowell, K.G.; Ferris, D.P. Weighted phase lag index stability as an artifact resistant measure to detect cognitive EEG activity during locomotion. *J. Neuroeng. Rehabil.* **2012**, *9*, 1–9.

169. Goebel, R.; Roebroeck, A.; Kim, D.S.; Formisano, E. Investigating directed cortical interactions in

time-resolved fMRI data using vector autoregressive modeling and Granger causality mapping. *Magn. Reson. Imaging* **2003**, *21*, 1251–1261.

170. Zhou, Z.; Ding, M.; Chen, Y.; Wright, P.; Lu, Z.; Liu, Y. Detecting directional influence in fMRI connectivity analysis using PCA based Granger causality. *Brain Res.* **2009**, *1289*, 22–29.

171. Rajapakse, J.C.; Wang, Y.; Zheng, X.; Zhou, J. Probabilistic framework for brain connectivity from functional MR images. *IEEE Trans. Med. Imaging* **2008**, *27*, 825–833.

172. Kaminski, M.J.; Blinowska, K.J. A new method of the description of the information flow in the brain structures. *Biol. Cybern.* **1991**, *65*, 203–210.

173. Brunner, C.; Billinger, M.; Seeber, M.; Mullen, T.R.; Makeig, S. Volume Conduction Influences Scalp-Based Connectivity Estimates. *Front. Comput. Neurosci.* **2016**, *10*, 121.

174. Baccalá, L.A.; Sameshima, K. Partial directed coherence: a new concept in neural structure determination. *Biol. Cybern.* **2001**, *84*, 463–474.

175. Blinowska, K.J. Review of the methods of determination of directed connectivity from multichannel data. *Med. Biol. Eng. Comput.* **2011**, *49*, 521–529.

176. Babiloni, F.; Cincotti, F.; Babiloni, C.; Carducci, F.; Mattia, D.; Astolfi, L.; Basilisco, A.; Rossini, P.M.; Ding, L.; Ni, Y.; et al. Estimation of the cortical functional connectivity with the multimodal integration of high-resolution EEG and fMRI data by directed transfer function. *Neuroimage* **2005**, *24*, 118–131.

177. De Pasquale, F.; Della Penna, S.; Sporns, O.; Romani, G.L.; Corbetta, M. A Dynamic Core Network and Global Efficiency in the Resting Human Brain. *Cereb. Cortex* **2016**, *26*, 4015–4033.

178. Freeman, L.C. A Set of Measures of Centrality Based on Betweenness. *Sociometry* **1977**, *40*, 35.

179. Newman, M.E.J. Modularity and community structure in networks. *Proc. Natl. Acad. Sci. U. S. A.* **2006**, *103*, 8577–8582.

180. Feigin, V.L.; Roth, G.A.; Naghavi, M.; Parmar, P.; Krishnamurthi, R.; Chugh, S.; Mensah, G.A.; Norrving, B.; Shiue, I.; Ng, M.; et al. Global burden of stroke and risk factors in 188 countries, during 1990–2013: a systematic analysis for the Global Burden of Disease Study 2013. *Lancet Neurol.* **2016**, *15*, 913–924.

181. Dromerick, A.W.; Reding, M.J. Functional Outcome for Patients With Hemiparesis, Hemihypesthesia, and Hemianopsia. *Stroke* **1995**, *26*, 2023–2026.

182. James, G.A.; Lu, Z.L.; VanMeter, J.W.; Sathian; Hu, X.P.; Butler, A.J. Changes in resting state effective connectivity in the motor network following rehabilitation of upper extremity poststroke paresis. *Top. Stroke Rehabil.* **2009**, *16*, 270–281.

183. Granziera, C.; Daducci, A.; Meskaldji, D.E.; Roche, A.; Maeder, P.; Michel, P.; Hadjikhani, N.; Sorensen, A.G.; Frackowiak, R.S.; Thiran, J.P.; et al. A new early and automated MRI-based predictor of motor improvement after stroke. *Neurology* **2012**, *79*, 39–46.

184. Burke, E.; Cramer, S.C. Biomarkers and predictors of restorative therapy effects after stroke topical collection on stroke. *Curr. Neurol. Neurosci. Rep.* **2013**, *13*.

185. Zhu, L.L.; Lindenberg, R.; Alexander, M.P.; Schlaug, G. Lesion load of the corticospinal tract predicts motor impairment in chronic stroke. *Stroke* **2010**, *41*, 910–915.

186. Lindenberg, R.; Renga, V.; Zhu, L.L.; Betzler, F.; Alsop, D.; Schlaug, G. Structural integrity of corticospinal motor fibers predicts motor impairment in chronic stroke. *Neurology* **2010**, *74*, 280–287.

187. Johansen-Berg, H.; Dawes, H.; Guy, C.; Smith, S.M.; Wade, D.T.; Matthews, P.M. Correlation between motor improvements and altered fMRI activity after rehabilitative therapy. *Brain* **2002**, *125*, 2731–2742.

188. Pearce, J.M.S. Broca's Aphasiacs. *Eur. Neurol.* **2009**, *61*, 183–189.

189. Gläscher, J.; Tranel, D.; Paul, L.K.; Rudrauf, D.; Rorden, C.; Hornaday, A.; Grabowski, T.; Damasio, H.; Adolphs, R. Lesion Mapping of Cognitive Abilities Linked to Intelligence. *Neuron* **2009**, *61*, 681–691.

190. Rao, S.M.; Binder, J.R.; Bandettini, P.A.; Hammeke, T.A.; Yetkin, F.Z.; Jesmanowicz, A.; Lisk, L.M.; Morris, G.L.; Mueller, W.M.; Estkowski, L.D.; et al. Functional magnetic resonance imaging of complex human movements. *Neurology* **1993**, *43*, 2311–2318.

191. Goodin, P.; Lamp, G.; Vidyasagar, R.; McArdle, D.; Seitz, R.J.; Carey, L.M. Altered functional connectivity differs in stroke survivors with impaired touch sensation following left and right hemisphere lesions. *NeuroImage Clin.* **2018**, *18*, 342–355.

192. Puig, J.; Blasco, G.; Alberich-Bayarri, A.; Schlaug, G.; Deco, G.; Biarnes, C.; Navas-Martí, M.; Rivero, M.; Gich, J.; Figueras, J.; et al. Resting-state functional connectivity magnetic resonance imaging and outcome after acute stroke. *Stroke* **2018**, *49*, 2353–2360.

193. Tuladhar, A.M.; Snaphaan, L.; Shumskaya, E.; Rijpkema, M.; Fernandez, G.; Norris, D.G.; de Leeuw, F.-E. Default Mode Network Connectivity in Stroke Patients. *PLoS One* **2013**, *8*, e66556.

194. Saur, D.; Lange, R.; Baumgaertner, A.; Schraknepper, V.; Willmes, K.; Rijntjes, M.; Weiller, C. Dynamics of language reorganization after stroke. *Brain* **2006**, *129*, 1371–1384.

195. Nudo, R.J.; Wise, B.M.; SiFuentes, F.; Milliken, G.W. Neural substrates for the effects of rehabilitative training on motor recovery after ischemic infarct. *Science (80-.).* **1996**, *272*, 1791–1794.

196. Vinck, M.; Oostenveld, R.; van Wingerden, M.; Battaglia, F.; Pennartz, C.M.A. An improved index of phase-synchronization for electrophysiological data in the presence of volume-conduction, noise and sample-size bias. *Neuroimage* **2011**, *55*, 1548–1565.

197. Chennu, S.; Finoia, P.; Kamau, E.; Allanson, J.; Williams, G.B.; Monti, M.M.; Noreika, V.; Arnatkeviciute, A.; Canales-Johnson, A.; Olivares, F.; et al. Spectral Signatures of Reorganised Brain Networks in Disorders of Consciousness. *PLoS Comput. Biol.* **2014**.

198. Edmunds1, K.; , H Petersen2, 3, M.H.; Yassine4, S.; Olivieri5, A.; , F Barollo1, 6, R.F.; Edmunds1, PGÍslason1, M.; Fratini6, A.; , and P Gargiulo1, 7 Cortical recruitment and functional dynamics in postural control adaptation and habituation during vibratory proprioceptive stimulation. *J. Neural Eng.* **2019**.

199. Sporns, O.; Zwi, J.D. The small world of the cerebral cortex. *Neuroinformatics* 2004, *2*, 145–162.

200. Measuring electrophysiological connectivity by power envelope correlation: a technical review on MEG methods. - PubMed - NCBI Available online: https://www.ncbi.nlm.nih.gov/pubmed/26447925 (accessed on Apr 26, 2020).

201. Hampson, M.; Driesen, N.R.; Skudlarski, P.; Gore, J.C.; Constable, R.T. Brain connectivity related to working memory performance. *J. Neurosci.* **2006**, *26*, 13338–13343.

202. Liddle, E.B.; Price, D.; Palaniyappan, L.; Brookes, M.J.; Robson, S.E.; Hall, E.L.; Morris, P.G.; Liddle, P.F. Abnormal salience signaling in schizophrenia: The role of integrative beta oscillations. *Hum. Brain Mapp.* **2016**, *37*, 1361–1374.

203. Pfurtscheller, G.; Lopes Da Silva, F.H. Event-related EEG/MEG synchronization and desynchronization: Basic principles. *Clin. Neurophysiol.* 1999, *110*, 1842–1857.

204. Allen, E.A.; Damaraju, E.; Eichele, T.; Wu, L.; Calhoun, V.D. EEG Signatures of Dynamic Functional Network Connectivity States. *Brain Topogr.* **2018**, *31*, 101–116.

205. O'Neill, G.C.; Tewarie, P.K.; Colclough, G.L.; Gascoyne, L.E.; Hunt, B.A.E.; Morris, P.G.; Woolrich, M.W.; Brookes, M.J. Measurement of dynamic task related functional networks using MEG. *Neuroimage* **2017**, *146*, 667–678.

206. Preti, M.G.; Bolton, T.A.; Van De Ville, D. The dynamic functional connectome: State-of-the-art and perspectives. *Neuroimage* **2017**, *160*, 41–54.

207. Tracking whole-brain connectivity dynamics in the resting state. - PubMed - NCBI Available online: https://www.ncbi.nlm.nih.gov/pubmed/23146964 (accessed on Apr 26, 2020).

208. O'Neill, G.C.; Tewarie, P.; Vidaurre, D.; Liuzzi, L.; Woolrich, M.W.; Brookes, M.J. Dynamics of large-scale electrophysiological networks: A technical review. *Neuroimage* 2018, *180*, 559–576.

209. Preti, M.G.; Bolton, T.A.; Van De Ville, D. The dynamic functional connectome: State-of-the-art and perspectives. *Neuroimage* **2017**, *160*, 41–54.

210. Huang, N.E.; Shen, Z.; Long, S.R.; Wu, M.C.; Shih, H.H.; Zheng, Q.; Yen, N.-C.; Tung, C.C.; Liu, H.H. The Empirical Mode Decomposition and the Hilbert Spectrum for Nonlinear and Non-Stationary Time Series Analysis. *Proc. Math. Phys. Eng. Sci. 454*, 903–995.

211. Huang, N.E. Complementary Ensemble Empirical Mode Decomposition: A Novel Noise Enhanced Data Analysis Method. **2010**, *2*, 135–156.

212. Hassan, A.R.; Hassan Bhuiyan, M.I. Automatic sleep scoring using statistical features in the EMD domain and ensemble methods. *Biocybern. Biomed. Eng.* **2016**, *36*, 248–255.

213. Williams, N.J.; Nasuto, S.J.; Saddy, J.D. Method for exploratory cluster analysis and visualisation of single-trial ERP ensembles. *J. Neurosci. Methods* **2015**, *250*, 22–33.

214. Wu, Z.; Huang, N.E. Ensemble empirical mode decomposition: A noise-assisted data analysis method. *Adv. Adapt. Data Anal.* **2009**, *1*, 1–41.

215. Torres, M.E.; Colominas, M.A.; Schlotthauer, G.; Flandrin, P. A complete ensemble empirical mode decomposition with adaptive noise. In Proceedings of the ICASSP, IEEE International Conference on Acoustics, Speech and Signal Processing - Proceedings; 2011; pp. 4144–4147.

216. Colominas, M.A.; Schlotthauer, G.; Torres, M.E. Improved complete ensemble EMD: A suitable tool for biomedical signal processing. *Biomed. Signal Process. Control* **2014**, *14*, 19–29.

217. Doron, K.W.; Bassett, D.S.; Gazzaniga, M.S. Dynamic network structure of interhemispheric coordination. *Proc. Natl. Acad. Sci. U. S. A.* **2012**, *109*, 18661–18668.

218. Leonardi, N.; Van De Ville, D. On spurious and real fluctuations of dynamic functional connectivity during rest. *Neuroimage* 2015, *104*, 430–436.

219. Zalesky, A.; Breakspear, M. Towards a statistical test for functional connectivity dynamics. *Neuroimage* 2015, *114*, 466–470.

220. Thakur, G.; Wu, H.T. Synchrosqueezing-based recovery of instantaneous frequency from nonuniform samples. *SIAM J. Math. Anal.* **2011**, *43*, 2078–2095.

221. Yule, G.U. On a Method of Investigating Periodicities in Disturbed Series, with Special Reference to Wolfer's Sunspot Numbers. *Philos. Trans. R. Soc. London. Ser. A, Contain. Pap. a Math. or Phys. Character 226*, 267–298.

222. Burg, J.P. The relationship between maximum entropy spectra and maximum likelihood spectra. *Geophysics* **1972**, *37*, 375–376.

223. Kay, S.M.; Marple, S.L. Spectrum Analysis—A Modern Perspective. *Proc. IEEE* **1981**, *69*, 1380–1419.

224. Schlotthauer, G.; Torres, M.E.; Rufiner, H.L. A new algorithm for instantaneous F 0 speech extraction based on ensemble empirical mode decomposition. In Proceedings of the European Signal Processing Conference; 2009; pp. 2347–2351.

225. Yeh, J.R.; Shieh, J.S.; Huang, N.E. Complementary ensemble empirical mode decomposition: A novel noise enhanced data analysis method. *Adv. Adapt. Data Anal.* **2010**, *2*, 135–156.

226. Navarro, X.; Porée, F.; Carrault, G. ECG removal in preterm EEG combining empirical mode decomposition and adaptive filtering. In Proceedings of the ICASSP, IEEE International Conference on Acoustics, Speech and Signal Processing - Proceedings; 2012; pp. 661–664.

227. Han, J.; van der Baan, M. Empirical mode decomposition for seismic time-frequency analysis. *Geophysics* **2013**, *78*.

228. Nalband, S.; Valliappan, C.A.; Prince, A.A.; Agrawal, A. Time-frequency based feature extraction for the analysis of vibroarthographic signals. *Comput. Electr. Eng.* **2018**, *69*, 720–731.

229. Muñoz-Gutiérrez, P.A.; Giraldo, E.; Bueno-López, M.; Molinas, M. Localization of active brain sources from EEG signals using empirical mode decomposition: a comparative study. *Front. Integr. Neurosci.* **2018**, *12*.

230. Lin, C.-F.; Zhu, J.-D. Hilbert–Huang transformation-based time-frequency analysis methods in biomedical signal applications. *Proc. Inst. Mech. Eng. Part H J. Eng. Med.* **2012**, *226*, 208–216.

231. Boashash, B.; Stevenson, N.J.; Rankine, L.J.; Stevenson, N.J.; Azemi, G.; Sejdić, E.; Aviyente, S.; Akan, A.; Mert, A.; Dong, S.; et al. Time-frequency methodologies in neurosciences. In *Time-Frequency Signal Analysis and Processing: A Comprehensive Reference*; Elsevier Inc., 2016; pp. 915–966 ISBN 9780123984999.

232. Wu, C.H.; Chang, H.C.; Lee, P.L.; Li, K.S.; Sie, J.J.; Sun, C.W.; Yang, C.Y.; Li, P.H.; Deng, H.T.; Shyu, K.K. Frequency recognition in an SSVEP-based brain computer interface using empirical mode decomposition and refined generalized zero-crossing. *J. Neurosci. Methods* **2011**, *196*, 170–181.

233. Wu, C.-H.; Chang, H.-C.; Lee, P.-L. Instantaneous Gaze-Target Detection by Empirical Mode Decomposition: Application to Brain Computer Interface. In; Springer, Berlin, Heidelberg, 2009; pp. 215–218.

234. Huang, N.E.; Shen, Z.; Long, S.R.; Wu, M.C.; Snin, H.H.; Zheng, Q.; Yen, N.C.; Tung, C.C.; Liu, H.H. The empirical mode decomposition and the Hilbert spectrum for nonlinear and non-stationary time series analysis. *Proc. R. Soc. A Math. Phys. Eng. Sci.* **1998**, *454*, 903–995.

235. Barut, Ç.; Kiziltan, E.; Gelir, E.; Köktürk, F. Advanced analysis of finger-tapping performance: A preliminary study. *Balkan Med. J.* **2013**, *30*, 167–171.